INVERSION OF REFLECTION SEISMOGRAMS

by

SHLOMO LEVY

M.Sc. The University Of British Columbia

B.Sc. University of California at Los Angeles

A THESIS SUBMITTED IN PARTIAL FULFILMENT OF

THE REQUIREMENT FOR THE DEGREE OF

DOCTOR OF PHILOSOPHY

in

THE FACULTY OF GRADUATE STUDIES

Department of Geophysics And Astronomy

We accept this thesis as conforming to the required standard

THE UNIVERSITY OF BRITISH COLUMBIA

MAY 1985

In presenting this thesis in partial fulfilment of the requirements for an advanced degree at the University of British Columbia, I agree that the Library shall make it freely available for reference and study. I further agree that permission for extensive copying of this thesis for scholarly purposes may be granted by the head of my department or by his or her representatives. It is understood that copying or publication of this thesis for financial gain shall not be allowed without my written permission.

Department of GEOPHYSICS AND ASTRONOMY

The University of British Columbia
1956 Main Mall
Vancouver, Canada
V6T 1Y3

Date 1/10/85

Abstract

A method for the estimation of impedance or pseudo-velocity sections from the information contained in CMP stacked sections, the corresponding stacking velocities and sonic and density logs (when available) is presented. The method relies on a linear programming approach for the reconstruction of full-band reflectivities, and utilizes linearized relations between the multiple free reflectivity functions and average or point-wise impedance or velocity values. The reconstruction procedure requires the solution of an underdetermined set of equations and hence a minimum structure condition is imposed on the desired solution. This condition guaranties the uniqueness of the obtained solution in the sense that it is the solution that features the least amount of impedance variations as a function of travel-time (or depth). Since the presented inversion yields minimum structure solutions, it is argued that features which appear on the obtained result are strictly demanded by the data and are not artifacts of the inversion scheme.

A number of physical assumptions are required by the presented inversion. These are summarized below in point form:

(1) The earth reflectivity function is non-white and can be reasonably represented by a sparse spike train.

(2) The observed CMP stacked section is a reasonable representation of the multiple-free normal-ray section with reasonably correct relative amplitude relations.

(3) The residual wavelet on the stacked section is to a good approximation a zero-phase wavelet with a relatively flat spectrum.

(4) The estimated stacking velocities can be inverted to yield an acceptable representation of the averages of the true earth velocity model.

Since in a realistic environment some of the above assumptions may be violated, all the corresponding relations in the presented inversion scheme include appropriate uncertainty terms. That is, all the information components considered in the inversion are satisfied only to within some prespecified error bounds.

A number of possibilities for speeding up the inversion scheme are described. It is shown that utilizing the expected trace-to-trace coherency of seismic reflection data yields considerable reduction in computational efforts.

Finally, a number of steps required for a successful completion of the inversion are described. In particular, the problems of preinversion data scaling and the correction of the residual wavelet's phase are discussed in some detail.

TABLE OF CONTENTS

Abstract .....(ii)

List of Tables .....(x)

List of Figures .....(xi)

Acknowledgments .....(xvi)

Chapter I: Introduction 1

1.1 Stage I: Early Developments 2

1.2 Stage II: External Constraints in the Reconstruction of Full-Band Reflectivities 4

1.3 Stage III: Practical Implementation of the Inversion . 6

Chapter II: Reconstruction of a Sparse Spike Train From a Portion of its Spectrum and Application to High Resolution Deconvolution 8

2.1 Introduction 8

2.2 Reconstruction of a Sparse Spike Train from a Portion of its Spectrum 10

2.3 Examples with Noise-Free Data 13
2.3.1 Example 1 13
2.3.2 Example 2 14
2.4 Selection of Data in the Frequency Domain in the Presence of Noise 16
2.4.1 Empirical Cutoff 19
2.4.2 Statistical Cutoff 19
2.5 Formulation of the Inverse Problem in the Presence of Noise 22
2.5.1 Inequality Constraints 22
2.5.2 Equality Constraints 24
2.6 Examples with Noisy Data 26
2.6.1 Example 3 27
2.6.2 Example 4 29
2.7 Practical Recommendations 31
2.8 Comparison with Least-Squares Techniques 34
2.8.1 Example 5 35
2.8.2 Example 6 36
2.9 Conclusions 39

Chapter III: Acoustic Impedance Inversion and Well-Log Constraints 41
3.1 Introduction 41
3.2 External Constraints in Impedance Inversion 43
3.3 Point Velocity Constraints - Well Log Information 44
3.4 Discussion 46

Chapter IV: RMS Velocities and Recovery of the Acoustic Impedance 48

4.1 Introduction 48

4.2 Inversion of RMS Velocities: Model Construction 54

4.3 Linear Appraisal 67

4.4 Derivation of the Impedance Constraints 73

4.5 Summary 88

Chapter V: Multi-Trace Simplex Algorithm in Seismic Data Analysis 92

5.1 Introduction 92

5.2 Simplex Algorithm (background) 93

5.3 Basic Formulation of the Algorithm 98

5.4 Solving Multiple Related Problems 101

5.5 Application to Seismic Data 103

5.6 Example 105

5.7 Summary 115

Chapter VI: Pre-Inversion Scaling of Reflection Seismograms 116

6.1 Introduction 116

6.2 Method 118

6.2.1 General 118

6.2.2 The Construction of Spiky Reflectivity Function - Relative Information 119

6.2.3 Well-Logs or Stacking Velocities - Absolute Information 120
6.2.4 Comparison of the Absolute and the Relative Information 121
6.2.5 Considerations Pertaining to the Use of Stacking Velocities for Scaling 123
6.2.6 Considerations Pertaining to Localized Spiking Deconvolution Failures 124
6.3 Synthetic Examples 125
6.3.1 Layered Earth Model with Well Defined Layer Boundaries 125
6.3.2 Layered Earth Model with Slowly Varying Impedance Zones 131
6.4 Real Data Examples 135
6.4.1 Scaling Data Using Well-Log Information 135
6.4.2 Scaling Data Using Stacking Velocity Information 143
6.5 Conclusion 147

Chapter VII: Pre-Inversion Correction of Wavelet Residual Phase 150
7.1 Introduction 150
7.2 Method and Explanatory Examples 155
7.3 Real Data Examples 172
7.4 Concluding Comments 179

Chapter VIII: Summary 182

References 201

Appendix 2-A: Mean Noise Power and the Variance of a Random Noise Process 206

Appendix 2-B: The Choice of Statistical Cutoff in LP Deconvolution 209

Appendix 2-C: Noise Consideration in the Equality Constraints Formulation of LP Deconvolution 211

Appendix 6-A: AR Spiking Deconvolution of Band-Limited Data .213

Appendix 7-A: The Deconvolution of Phase-Shifted Wavelets ...217

7-A.1 Introduction 217

7-A.2 Theory 220

7-A.3 Conclusions 246

Appendix 7-B: Applications of Analytic Common Signal Analysis in Exploration Geophysics 248

7-B.1 Introduction 248

7-B.2 Mathematical Background 249

7-B.3 Modelling Dispersion by a Constant Phase-Shift 255

7-B.4 Density and Velocity Estimation from Super-Critical Reflections 260

7-B.5 Conclusions 265

LIST OF TABLES

4.1 Seventeen accurate and inaccurate RMS velocities 62

5.1 CPU run times for the modified Simplex algorithm. 114

6.1 Scale factor evaluation for a simple model 127

6.2 Scale factor evaluation for impedance model with ramp-like components 134

7.1 The varimax standout for a bandlimited sinc function 160

7.2 Summary of the application of the automatic phase correction algorithm to well-log synthetic reflectivities 165

7.3 Summary of the application of the automatic phase correction algorithm to well-log synthetic reflectivities after AR spectral extension 169

7-A.1 Phase and amplitude estimates as a function of reflectors time separation 239

7-B.1 Offset, angle of incidence and phase angle for reflections associated with a first-order multiple ...264

7-B.2 Density and sound speed ratios obtained via the inversion of phase shift information. 266

LIST OF FIGURES

2-1 Recovery of a sparse spike series - simple wavelet . 15

2-2 Recovery of a sparse spike series - complex wavelet 17

2-3 Recovery of a sparse spike series from noisy data - simple wavelet 30

2-4 Recovery of a sparse spike series from noisy data - complex wavelet 32

2-5 Recovery of a reflectivity series using frequency and time domain least squares deconvolution techniques - simple wavelet 37

2-6 Recovery of a reflectivity series using frequency and time domain least squares deconvolution techniques - complex wavelet 38

4-1 Velocity profile and the corresponding RMS velocity and reflectivity functions 58

4-2 Constructed interval velocity models - accurate data 61

4-3 Constructed interval velocity models - inaccurate data 65

4-4 Constructed interval velocity models, data include both RMS and point velocities 68

4-5 Trade-off diagram for RMS velocity inversion 71

4-6 Sample trade-off curves for t_0=0.55 seconds and t_0=1.25 seconds 72

4-7 Impedance inversion with RMS velocity constraints - accurate data 80

4-8 Impedance inversion with RMS velocity constraints - inaccurate data 84

4-9 Impedance inversion with RMS and point velocity constraints - inaccurate data 87

5-1 Geometrical interpretation of a linear programming problem 94

5-2 Geometrical and algorithmic closeness in the context of linear programming 97

5-3 Stacked section featuring a reasonable trace to trace correlation 106

5-4 The data of Figure 5-3 after spectral whitening, phase correction and three-trace princpal component SNR enhacement 107

5-5 The data of Figure 5-4 after linear programming deconvolution with the multitrace Simplex mode 109

5-6 The data of Figure 5-4 after linear programming deconvolution with objective function weights and polarity constraints 110

5-7 The pseudo-impedance section obtained via the integration of the data in Figure 5-5 112

5-8 Pseudo-impedance section overlaid on the full band LP reflectivity 113

6-1 Data for a simple scaling example 128

6-2 True pseudo-impedance function and the corresponding pseudo-impedances calculated from the LP solution and inverted interval velocities 129

6-3 The reconstructed acoustic impedance function obtained via constrained inversion of scaled data 130

6-4 Input data with a ramp-like component. Second synthetic example for scaling 132

6-5 True pseudo-impedance function and the corresponding pseudo-impedances calculated from the LP solution and inverted interval velocities (second example) 136

6-6 The velocity function obtained from the constrained inversion of the second set of synthetic data 137

6-7 Input seismograms after post stack spectral whitening and phase correction 138

6-8 Sonic log from a well site at the vicinity of trace 70 139

6-9 The data of Figure 6-7 after application of linear programming deconvolution 141

6-10 The pseudo-impedance section obtained via the integration of the data in Figure 6-9 142

6-11 The result of a constrained inversion 144

6-12 Input stacked section 145

6-13 Interval velocity section obtained by the inversion of a set of stacking velocity profiles 146

6-14 The result of a constrained inversion (with stacking velocities) 148

7-1 Phase rotations of a Klauder wavelet 157

7-2 Phase correction of mixed delay wavelets 162

7-3 Phase correction and dipole reflectivity 164

7-4 Eight velocity logs and the corresponding reflectivity functions 166

7-5 Example of an alternative deconvolution approach 173

7-6a CMP seismograms representing the output of a standard processing sequence 176

7-6b The data of Fig. 7-6a after zero-phase deconvolution .177

7-6c Phase corrected data 178

7-7 Comparison of unconstrained impedance inversion before and after the application of phase correction 180

7-8 The result of unconstrained inversion applied to phase corrected data 181

7-A.1 The basic quantities involved in the deconvolution of phase shifted wavelets 229

7-A.2 Simple example of the deconvolution of phase shifted data 241

7-A.3 Conventional deconvolution of the data shown in Figure 7-A.2 244

7-A.4 Wavelet shifted by varying amounts of phase-shift angles 245

7-B.1 Dispersed Ricker wavelets and the corresponding principal components 257

7-B.2 Dispersed and attenuated Ricker wavelets and the corresponding principal components 259

7-B.3a Reduced time plot of the data for phase inversion example 262

7-B.3b,c Phase estimation with the K-L transform 263

ACKNOWLEDGEMENTS

I am proud to belong to the group which at a relatively low cost developed a working solution to an important industrial problem. Since there weren't many road signs on the route that we have chosen, the majority of the components presented here are original and have not been previously treated in the published literature. My deepest thanks are given to those researchers (Dr. D.W. Oldenburg, Dr. P.K. Fullagar, K. Stinson, T. Scheuer, Dr. T.J. Ulrych, C. Walker, B.T. Prager and I.F. Jones) who took the whole or selected portions of this research road and contributed greatly to the solution of the problem presented in this work.

I am also grateful to my friends J.J. Cabrera and S. Clegg for their help in the preparation of this thesis.

CHAPTER I: INTRODUCTION

The following work is dedicated to the problem of seismogram inversion (that is, the construction of impedance or velocity sections from the information contained in reflection seismograms). The results of this inversion should enhance the interpretability of the data and supply additional information which may be subsequently used for the inference of petrophysical parameters. The problem, which is complex and exhibits a high degree of non-uniqueness, has been tackled in three stages each of which reflects the level of naivety prevailing at the corresponding time of development. After a long period of struggle a complete set of algorithms which presents a working solution to the impedance inversion problem has been developed. An outline of the solution presented in this work is given below.

1.1 STAGE I: EARLY DEVELOPMENTS

At the early stages of this work, the problem of the acoustic impedance inversion of reflection seismograms was not treated directly. Rather, I have concentrated my efforts on the construction of full-band reflectivity functions from the available band-limited information. I started by assuming a model in which the reflection seismograms consist of the convolution of a band-limited zero-phase (flat-spectrum) wavelet with a sparse spike earth response function. To the product of this convolution we have allowed the addition of a certain level of random noise. Then the problem under consideration was the recoverability of the full-band reflectivity series from the available band-limited signal. Chapter II shows that via the use of the Linear Programming (LP) scheme, and the minimization of the L_1 norm of the desired reflectivity model, a good representation of a sparse spike series can be recovered from a relatively small portion of its spectrum.

A latter work by Scheuer (1981) and Oldenburg et al. (1983) has pointed out that for data in which the multiples were removed from the measured seismograms prior to LP reconstruction of the full-band reflectivity function, direct integration of the recovered reflectivity will yield a reasonable

representation of the true earth relative impedance function.

Although stacked sections (the input to the following inversion scheme) do not generally represent the ideal primary-only section required here, processing chains which contain operations like stack with primary stacking velocities, gap-deconvolution and frequency-wave number filters will largely suppress multiple effects. Energy contained in the remaining multiples can then be treated as noise and be further suppressed by the internal mechanism of the algorithm as was described in Oldenburg et al. 1983. The reader who is still skeptical as to the applicability of the primaries-only model to real seismic data is reminded that the generation of a stacked section in which primary events and all their corresponding multiples are present is equally as hard as the generation of a multiple-free section. Consequently, the starting point of the inversion procedure to be described in this work is no worse than that underlying wave-equation approaches to the impedance inversion problem.

Scheuer (1981), and Oldenburg et al. (1983) have also presented a different approach to the reconstruction of the full-band reflectivity function. This approach uses the Auto-Regressive model and extrapolates the available frequency information toward the missing low and high frequencies by means of a prediction operator. Most importantly, they have incorporated velocity constraints into the deconvolution problem

and thereby created the basis of what will be later referred to as geological deconvolution. In Chapter III I describe the essentials of this later addition. I should add that my contribution to this portion of the work was rather minor.

1.2 STAGE II: EXTERNAL CONSTRAINTS IN THE RECONSTRUCTION OF FULL-BAND REFLECTIVITIES

At the early stages of this work, it was believed that given the ideal data, an inversion procedure involving the integration and exponentiation of the full-band reflectivity function reconstructed from the information contained in the seismogram alone should yield a reasonable estimate of the corresponding impedance function. Although this operation seemed to be successful in a fairly large number of cases (particularly on short time windows featuring a relatively small number of sharp impedance contrasts), there are a considerable number of geological-physical models in which satisfactory impedance reconstuction requires additional information. For example, the incorporation of information contained in the velocity and density logs acquired at a well site in the vicinity of the line of interest is likely to yield a significant reduction in the allowed solution space. Hence, the solution obtained from the combined information set is considerably more reliable.

Since well-logs are not always available and since it is not always possible to establish a clear tie between the well-log information and the observed stacked section, we had to look for additional information sources which will routinely be at our disposal. The most natural source of information concerning gross velocity structure is stored in the set of velocities used in the stacking process. In Chapter IV we present a scheme through which a linearized relation between the stacking velocities and the constructed full-band reflectivities is established. Using this relation, the deconvolution/impedance inversion process is better constrained; that is, we have further limited the solution space and thereby decreased the non-uniqueness associated with the problem.

It is important to note that using the stacking velocities and the CMP stacked seismograms simultaneously, the inversion scheme proposed here is utilizing both the dynamic and the kinematic properties of the recorded data. The additional information supplied from the well-logs is used to further decrease the allowed solution space and thereby increase the solution's reliability.

1.3 STAGE III: PRACTICAL IMPLEMENTATION OF THE INVERSION

Academically speaking the combined approach presented in Chapters II, III and IV, constitutes a reasonable solution to the problem we set forth to solve. However, a number of practical considerations had to be addressed in order to transform this work into an economically viable and geophysically reliable production algorithm. The efforts in this stage are directed toward the following aspects:

A. Speeding up the linear-programming algorithm.

B. Scaling the observed stacked section so that the incorporation of the three information sets into the inversion will yield physically meaningful results, and

C. Correcting the phase of the residual (interpreter's) wavelet so that the input seismograms will constitute a reasonable approximation to the earth reflectivity function convolved with a zero-phase wavelet.

Chapter V describes procedures for improving the computational efficiency of the linear programming algorithm, Chapter VI discusses the pre-inversion scaling of stacked sections and Chapter VII describes a partial solution to the problem of phase correction. In the appendices of Chapter VII,

we take the reader through the concept of the constant phase shift model and present a number of methods for the estimation of the desired phase shift angle. However, the essential contribution of Chapter VII is the automatic phase correction in which we use a simple scheme to effect the desired correction.

An interesting secondary outcome of the phase correction study is presented in Appendix VII-B. There, we describe the inversion of phase shifts associated with post-critical reflections to obtain both velocity and density information. This method was tried for the determination of the density and velocity of the uppermost layer of sediments in a deep water environment and was found to yield reasonable results.

Finally the conclusion of this work contains a description of the steps required for the completion of acoustic impedance inversion, together with some recommendations which may ease some of the initial pains that will afflict the reader who is interested in trying his hand in the subject.

CHAPTER 2: RECONSTRUCTION OF A SPARSE SPIKE TRAIN FROM A PORTION OF ITS SPECTRUM AND APPLICATION TO HIGH RESOLUTION DECONVOLUTION

2.1 INTRODUCTION

In seismology and other branches of applied science, it is often necessary to estimate a function from a portion of its Fourier transform, either because its complete transform cannot be measured or because sections of the transform are unreliable. Fourier transformation of an incomplete spectrum is an underdetermined linear inverse problem. Therefore it admits an infinite number of solutions (Backus and Gilbert, 1967, p. 251). If, however, the form of the unknown function can be restricted on physical grounds, it may be possible to determine the most physically acceptable solution by minimizing an appropriate norm. If a solution consisting of isolated spikes is required, minimization of the L_1-norm is most appropriate. Accordingly, a linear programming method has been developed to reconstruct a "sparse spike train" from a portion of its spectrum by minimizing the L_1-norm.

With the assumption that the earth response is a set of delta-functions of unknown amplitude and delay, one immediate field of application of the method is high-resolution seismic deconvolution. It is commonly observed that the signal-to-noise (S/N) ratio is very poor in certain portions of a seismic spectrum, and inclusion of these highly contaminated spectral

data in the calculation of the response function can produce gross errors. If the unreliable data are rejected, the inverse Fourier transformation is underdetermined and therefore has no unique solution. Indeed, if the reliable (albeit noisy) spectral data constitute the totality of the available information, a highly resolved estimate of the response function is necessarily associated with large uncertainties (Oldenburg, 1976, 1981). However, by enforcing the physical requirement that the earth response should consist of isolated spikes, i.e., by introducing additional information, the linear programming method described here is able to construct a response function estimate which is both acceptably accurate and well resolved. The efficacy of the method is demonstrated in single-trace examples with 10 percent random noise, and the quality of our results surpasses that attainable using conventional least-squares techniques.

Linear programming has been applied previously to seismic deconvolution (Claerbout and Muir, 1973; Taylor et al. 1979), but its potential was not fully exploited in the time-domain formulation adopted. The most significant differences in the present approach relate to the treatment of errors. First, by formulating the problem in the frequency domain, it is possible to identify (and then to discard) the spectral data which are most seriously contaminated; no such "winnowing" of data is possible in the time domain. Second, there is no attempt to minimize the misfit errors; the response function with minimum L_1-norm is always sought in our formulation because minimization of this norm favors solutions with as few nonzero values as

possible, i.e., with isolated spikes. The data are satisfied to an accuracy compatible with the perceived noise level. What degree of accuracy is "compatible" is governed by the propagation of random noise: this is considered in some detail in appendices 2-A, 2-B and 2-C.

2.2 RECONSTRUCTION OF A SPARSE SPIKE TRAIN FROM A PORTION OF ITS SPECTRUM

The unknown time series a(t) may be visualized as a generalized Dirac comb, i.e.,

$$a(t) = \sum_{n=0}^{N-1} a_n \delta(t - t_n), \qquad (2.1)$$

where $t_n = n\Delta t$, for some time increment Δt. The coefficients $\{a_n : n = 0, N - 1\}$ are the spike amplitudes; thus $a_n = 0$ when there is no spike at time t_n.

Denoting the Fourier transform of the time series a(t) by A(w), it follows from equation (2.1) that

$$A(w) = 1/N \sum_{n=0}^{N-1} a_n \exp(-i\omega t_n).$$

Hence,

$$\mathrm{Re}\{Aj\} = 1/N \sum_{n=0}^{N-1} a_n \cos(\omega j t_n), \tag{2.2}$$

$$\mathrm{Im}\{Aj\} = -\ 1/N \sum_{n=0}^{N-1} a \sin(\omega j t_n),$$

where $\omega j = 2j\pi/(N\Delta t)$ with $j = 0, 1, 2, \ldots, N/2$.

The defining relations (2.2) for the spectrum of a(t) constitute a set of linear constraints on the unknowns $\{a_n : n = 0, N - 1\}$. If the spectrum were known exactly for all $(N/2 + 1)$ distinct frequencies, the time series could be recovered perfectly by straightforward inverse Fourier transformation. When there are gaps in the spectrum, however, the inverse problem is underdetermined and admits an infinite number of solutions, corresponding to time series of greatly different appearance. If the time series is assumed to be a sparse spike train, by no means are all of these possible mathematical solutions physically acceptable, and it is desirable to introduce a criterion which discriminates against those solutions of inappropriate form. The criterion most suitable in this connection is the minimization of the L_1-norm $||a||_1$ of the time series a(t) where

$$||a||_1 = \sum_{n=0}^{N-1} |a_n|. \tag{2.3}$$

Linear programming may now be invoked to find the

coefficients {a} which satisfy the reliable spectral data and for which $||a||_1$ is minimum. The minimization of $||a||_1$ will favor solutions which are zero except at a small number of isolated times, and it will therefore tend to produce sparse spike trains, as desired. Furthermore, the number of nonzero values in the linear programming output never exceeds the number of constraints; in other words, the number of constraints is an upper limit on the number of spikes in the solution.

The Simplex algorithm is written for nonnegative unknowns only, whereas both positive and negative spikes are usually equally acceptable physically. This difficulty is overcome by expressing each spike amplitude as the difference between two positive quantities, i.e.,

$$a_n = b_n - c_n, \quad n = 0, N - 2. \tag{2.4}$$

where $b > 0$ and $c > 0$ for all $n = 0, N - 1$. The quantity actually minimized is the sum

$$s = \sum_{n=0}^{N-1} [b + c].$$

The minimum is attained when at least one of b and c is zero at each value of n; hence

$$|a_n| = |b_n - c_n| = |b_n + c_n|, \quad n = 0, N - 1.$$

2.3 EXAMPLES WITH NOISE-FREE DATA

The recovery of spikes from an incomplete spectrum may be visualized as deconvolution of a noise-free seismogram when the wavelet is known. Without loss of generality, therefore, the efficacy of the technique for (specialized) inverse Fourier transformation will be established by means of seismic examples.

The assumption that a seismogram $x^o(t)$ is a convolution of a source wavelet $w(t)$ with an earth response function $a(t)$ is widely used in applied seismology. In the frequency domain, this convolution may be expressed as a product, whence

$$A(\omega) = X^o(\omega)/W(\omega), \qquad (2.5)$$

where upper case symbols denote Fourier-transformed quantities.

2.3.1 EXAMPLE 1

The input time series in Figure 2-1c represents the convolution of the Ricker wavelet in Figure 2-1a with the spike train in Figure 2-1b. Our aim here is to show that the spike series can be reconstructed from a small portion of its spectrum

without significant loss of resolution. In implementing the technique described in Section 2.2, only those deconvolved spectral data $A(\omega)$ corresponding to frequencies between the arrows in Figure 2-1d were included in the computations which produced the times series shown in Figure 2-1e. Thus 20 percent of the spectrum sufficed for a perfect reconstruction of the generating spike sequence.

2.3.2 EXAMPLE 2

The seismogram in Figure 2-2c is the result of convolution of the wavelet in Figure 2-2a with the response function in Figure 2-2b. As in example 1, only the deconvolved data associated with frequencies between the arrows in Figure 2-2d entered into the calculations; both high and low frequencies have been discarded in this case. The output in Figure 2-2e exhibits a close resemblance to the original spike train in Figure 2-2b, although some of the spikes are split in two. This phenomenon is a manifestation of nonuniqueness arising from the neglect of some of the frequencies. The degree of splitting provides a qualitative indication of the resolving power of the method; a split spike indicates that resolution is plus or minus one time unit at best.

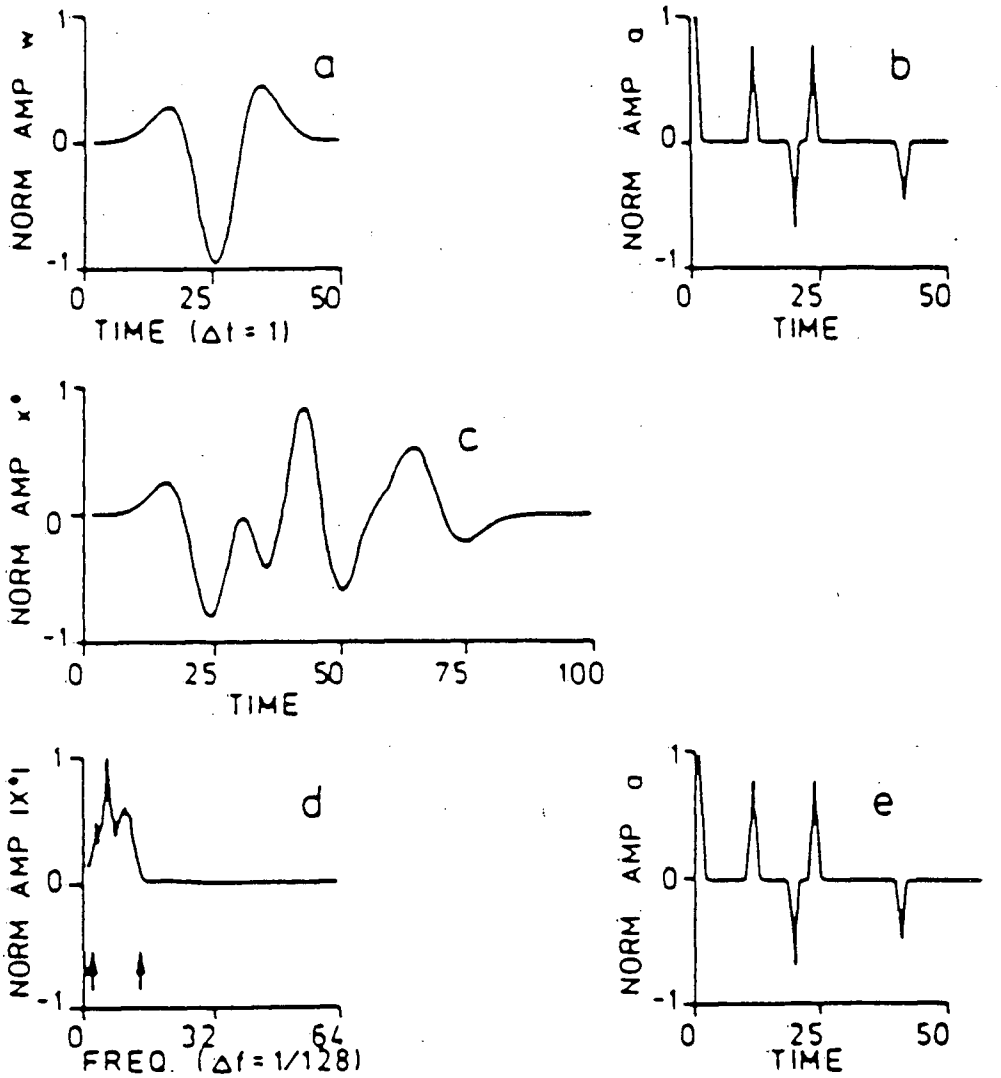

Figure 2-1

(a) A tapered Ricker wavelet. (b) Generating spike series. (c) Normalized input trace, obtained by convolving the wavelet in (a) with the series in (b). (d) Normalized amplitude spectrum of the seismogram in (c). (e) Normalized response function recovered using only the data corresponding to the frequencies between the arrows in (d).

2.4 SELECTION OF DATA IN THE FREQUENCY DOMAIN IN THE PRESENCE OF NOISE

Let $e(t)$ denote the noise in an observed seismogram $x(t)$, i.e.,

$$x(t) = x^0(t) + e(t),$$

where $x^0(t)$ represents the noise-free seismogram as before. If the wavelet is known, the noisy seismogram may be deconvolved in the frequency domain by dividing by the wavelet spectrum $W(\omega)$. The resulting estimate $A'(\omega)$ of the spectrum $A(\omega)$ is given by

$$A'(\omega) = X^0(\omega)/W(\omega) + E(\omega)/W(\omega), \tag{2.6}$$

where upper case letters denote Fourier transformed quantities as before. It may be observed that a conventional inverse Fourier transform of $A'(\omega)$ will not produce an acceptable estimate of $a(t)$ if at some frequencies $|E/W|$ is appreciable, in comparison with $|X^0/W|$.

To understand the influence of errors better, it is instructive to review the general characteristics of the component spectra which shape the spectrum of a seismogram. The amplitude spectrum of a typical wavelet falls off rapidly at

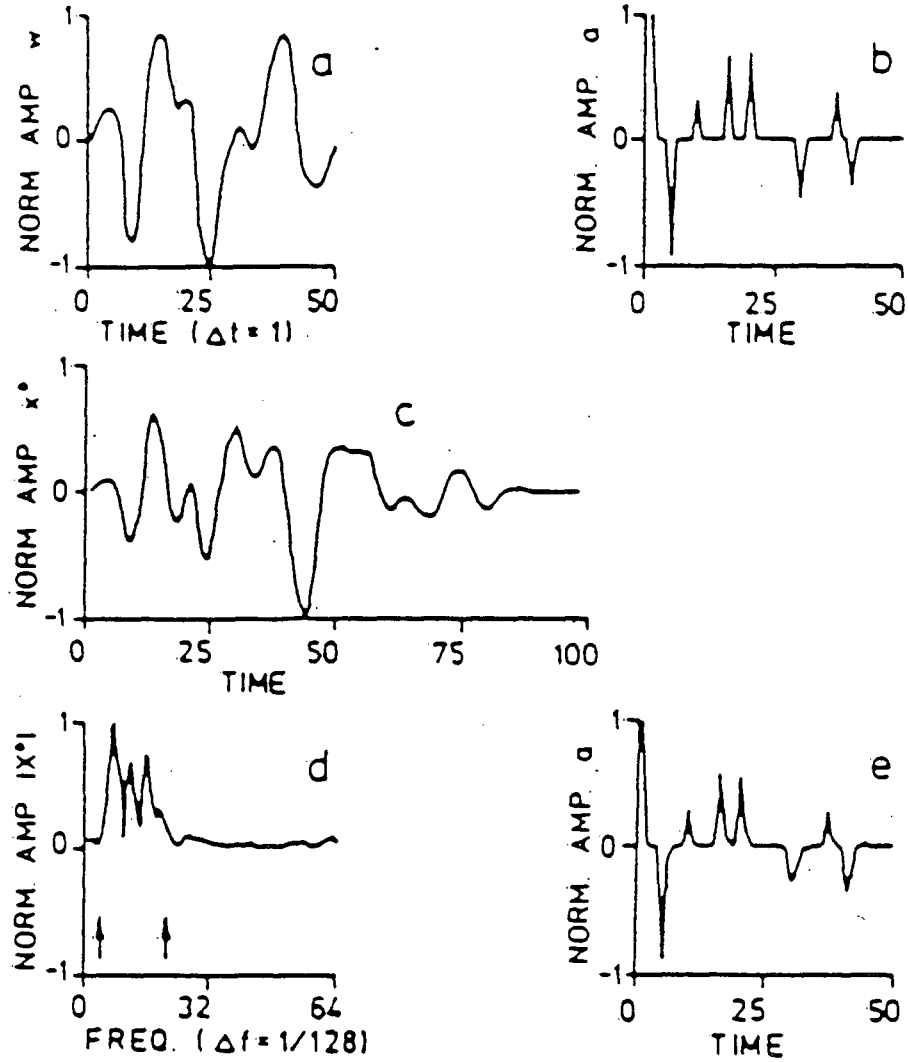

Figure 2-2

(a) A complex wavelet, devised by Wiggins (1978). (b) Normalized response function. (c) The normalized input trace, the result of convolving the wavelet in (a) with the spike train in (b). (d) Normalized amplitude spectrum of the seismogram in (c). (e) Reconstruction of the response function a(t) computed from spectral data associated with frequencies within the band delineated by the arrows in (d).

high frequency, whereas the spectrum of a spike series does not decay with frequency. The spectrum of a noise-free seismogram is the product of the wavelet and response spectra [per equation (2.5)] and it therefore decays with frequency like the wavelet spectrum. Consequently, if a seismogram is contaminated with pseudo-white noise, the S/N ratio is very poor at high frequencies because the noise power is almost independent of frequency. For the same reason, the reliable data are associated with frequencies at which the wavelet carries significant power.

If a(t) is estimated using only those deconvolved data corresponding to frequencies from a certain band, it will not be reconstructed perfectly unless some independent information is introduced. Some resolving power must be sacrificed if, for example, the unreliable data are replaced by zeros or if a penalty function is introduced to discriminate against the noisy data. What distinguishes our approach is that we make no a priori assumptions about the unreliable spectral data. Instead we use only the reliable data, in combination with the additional knowledge that the desired output consists of isolated spikes.

Whether or not the signal power at a certain frequency is significant must be assessed in relation to the noise power at that frequency. If the noise is pseudo-white, it is reasonable to introduce a cutoff and to regard a datum as "reliable" if it exceeds the cutoff, and "unreliable" otherwise. The choice of cutoff is governed by the perceived noise level; however, there

are no unequivocal quantitative rules, and two different procedures have been devised.

2.4.1 EMPIRICAL CUTOFF

An appropriate choice of cutoff can usually be made after inspection of the amplitude spectrum of the seismogram or on the basis of prior knowledge of the level of noise to be expected. It is convenient to express the cutoff K as a fraction of max $\{|X(\omega)|\}$; only the deconvolved data at those frequencies for which $|X(\omega)| > K$ figure in the subsequent computations.

2.4.2 STATISTICAL CUTOFF

It is possible to develop a cutoff criterion based on the statistical properties of random noise. Following Jenkins and Watts (1969, p. 231), it is assumed that the noise in the time domain is a realization of a random process characterized by the random variables $\{Z_n: n = 0, N - 1\}$, each having mean zero and variance σ^2. If it is possible to isolate a portion of the spectrum of the seismogram (e.g., the high-frequency section) which is due to noise alone, then (as shown in Appendix 2-A) the mean observed power at these frequencies constitutes an estimate

σ^2 of σ^2. Considered as a random variable, σ^2 is distributed as a chi-squared variable, so confidence limits can be assigned using, for example, Figure 2-3-10 of Jenkins and Watts (1969).

Although the noise power is estimated from the spectrum of the observed seismogram $X(\omega)$ in the manner just described, it is the deconvolved spectrum X/W or A' which is used in the selection of frequencies because the reliability of the real and imaginary parts of A', not X, governs the accuracy of the data equations (2.6). The real and imaginary parts of A' are scrutinized independently, since there is no guarantee that both are reliable at a particular frequency, i.e. $|\mathrm{Re}\{X/W\}|$ may be large when $|\mathrm{Im}\{X/W\}|$ is small, or vice versa. The same cutoff is applied to both real and imaginary parts, so it is without loss of generality that the real part is considered in the development below. From equation (2.6) it follows that

$$\mathrm{Re}^2\{A'\} = \mathrm{Re}^2\{X^0/W\} + 2\mathrm{Re}\{X^0/W\}\mathrm{Re}\{E/W\} + \mathrm{Re}^2\{E/W\}. \qquad (2.7)$$

understanding that this equation applies at all frequencies.

If Re{E/W} is visualized as the realization of a random variable, say Q, then $\epsilon[Q]$ is zero, and by equation (2-B-2),

$$\epsilon[Q]^2 = \sigma^2/(2|W|^2), \qquad (2.8)$$

where $\epsilon(x)$ is the expected value of x.

Combining equations (2.7) and (2.8),

$$\epsilon[Re^2\{A'\}] = Re^2\{X^0/W\} + \sigma^2/(2|W|^2).$$

Thus the relative magnitudes of $Re^2\{A'\}$ and $\epsilon[Q^2]$ provide a measure of the reliability of $Re\{A'\}$. Introducing the free parameter a, the cutoff Kj, at frequency ωj is defined by

$$Kj = 2a^2\epsilon[Q_j^2] = a^2\sigma^2/|Wj|^2 \qquad (2.9)$$

and the real part is considered reliable at that frequency provided $Re^2\{Aj\} > Kj$.

The choice of a is guided by the probability distribution of Q^2; specifically, from Appendix 2-B,

$$Pr\{Q^2>Kj\} = erfc(a). \qquad (2.10)$$

In view of the uncertainty in the estimate σ^2, Kj cannot be calculated precisely using equation (2.9). Consequently, the probability that pure noise will exceed the cutoff at a particular value of a can be determined only approximately from equation (2.10).

2.5 FORMULATION OF THE INVERSE PROBLEM IN THE PRESENCE OF NOISE

Although the disturbing influence of the noise will be greatly reduced by winnowing the most erroneous spectral data, as described above, the remaining (reliable) data are not noise-free. It is therefore inappropriate to solve the data equations exactly. Two ways to take the errors into account are discussed here, using inequality and equality constraints, respectively.

2.5.1 INEQUALITY CONSTRAINTS

In the inequality formulation, the linear programming algorithm is required to fit the noisy data only to within certain limits and, recalling equations (2.2) and (2.4), the constraints are written in the following form:

$$+\mathrm{Re}\{A'_j\} + \epsilon j > + \frac{1}{N}\sum_{m=0}^{N-1}(b_m - c_m)\cos(\omega j t_m),$$

$$+\mathrm{Im}\{A'_j\} + \epsilon j > + \frac{1}{N}\sum_{m=0}^{N-1}(b_m - c_m)\sin(\omega j t_m), \qquad (2.11)$$

where ϵj is the assigned uncertainty at frequency ωj. These uncertainties do not appear in the objective function; the L_1-norm of the response function alone is to be minimized.

If the uncertainties are increased, there is a greater likelihood that the true spectral value lies within the prescribed limits. The greater the freedom allowed, the greater the probability that the algorithm will find a feasible solution with fewer spikes (i.e.with smaller L_1-norm) than the true response function. This feature can be exploited to determine the most prominent spikes. An increase in the uncertainties also reduces the computational labor and hence, the cost. Conversely, the cost increases as the uncertainties are decreased, and there is a tendency for more and more spikes to appear. There is no fail-safe way to distinguish true spikes from spurious spikes, but physically untenable response functions can result when the uncertainties are too small. This will be discussed further later.

Just as there is more than one way to choose a cutoff, so too is there some flexibility in the choice of uncertainties; two possibilities are described below.

(1) Empirical uncertainties. - The uncertainty may be chosen to be some small fraction of the cutoff K (defined under "Empirical cutoff" in the previous section). The most straightforward approach is then to assign the same uncertainty to all the data.

(2) Statistical uncertainties. - The choice of uncertainties may be guided by consideration of the statistical character of the noise. Specifically, it is appropriate in view of equation (2.6) to define the uncertainties in terms of the standard deviation

of Q, where Q is a random variable representing either Re{E/W} or Im{E/W} as before. Using equation (2-B-2), the defining relation is

$$\epsilon j = \beta \sqrt{\mathrm{Var}[Qj]} = 0.7071\ \beta\sigma/|Wj|,$$

where β is a free parameter. Note that the uncertainties are frequency dependent in this instance. If the noise is normal or near-normal, the familiar Gaussian confidence limits serve to guide the choice of β.

2.5.2 EQUALITY CONSTRAINTS

In the process of solving for the response function with minimum L_1-norm, the linear programming algorithm also indirectly determines an estimate of the noise. In the inequality formulation this mathematical noise is bounded at each frequency, but its over-all statistical character is very weakly constrained. For example, there is no guarantee that the mean of the noise removed by the algorithm is acceptably close to its expected value of zero, nor that its power is compatible with the perceived noise power. In order to control the removal of the noise more closely, the error can be introduced explicitly into each equation as an additional unknown, say ηj. Recalling equations (2.6) and (2.2) the resulting equality constraints can be written in the form:

$$\mathrm{Re}\{A'_j\} = \mathrm{Re}\{\eta j/Wj\} + 1/N \sum_{n=0}^{N-1}(b_n - c_n)\cos(\omega j t_n),$$

and (2.12)

$$\mathrm{Im}\{A'_j\} = \mathrm{Im}\{\eta j/Wj\} - \sqrt{1/N} \sum_{n=0}^{N-1}(b_n - c_n)\sin(\omega j t_n).$$

In solving these equations, the algorithm is required to minimize the L_1-norm of the response function as before, and in so doing to determine that statistically consistent set $\{\eta j\}$ most favorable to the minimization. The most obvious statistical restriction on the noise is that it have mean zero. In addition, it is possible to devise a constraint on its L_1-norm. Specifically, the expected value of the quantity S is prescribed, with S defined by

$$S = (1/M) \sum_{m=1}^{M} (|\mu_m| + |\nu_m|), \qquad (2.13)$$

where $\mu = \mathrm{Re}\{Ej(m)\}$ and $\nu = \mathrm{Im}\{Ej(m)\}$, with j(m) the index of the mth acceptable frequency, there being M such frequencies in all. A formula for $\epsilon[S]$ is derived in Appendix 2-C:

$$\epsilon[S] = 2\sigma/\sqrt{\pi}.$$

Since S is an average of M quantities, its variance decreases as M increases, i.e., as the number of reliable data increases. Thus the lower the cutoff, the more likely is S to

assume its expected value. In this sense, the noise compensation using equality constraints improve as more and more data are included in the computations; this is in contrast to the inequality formulation where the noise compensation is unaffected by the number of acceptable data.

The use of equality constraints does introduce considerably more variables into the linear programming problem, an extra four at each acceptable frequency in fact. However, the number of constraints is reduced by a factor of approximately two with respect to the corresponding problem with inequalities, and in general the computer costs are little more than those incurred using inequalities.

2.6 EXAMPLES WITH NOISY DATA

The examples studied earlier will now be reworked in the presence of Gaussian random noise. Three variants of our linear programming approach are tested below. Two of the variants, denoted by Ie and Is, employ inequality constraints but differ in their choices of cutoff and uncertainties: Variant Ie adopts the empirical criteria and the empirical uncertainties, while variant Is makes use of the statistical criteria and uncertainties. The third variant, denoted Es, employs statistical cutoff and equality constraints.

Whereas both location and relative amplitude of the spikes are usually faithfully reproduced when the data are perfectly accurate, the presence of errors in the data often renders it impossible to discriminate between the effect of a single spike at time t_n with amplitude c, say, and two spikes at times t_n and t_{n+1} with amplitudes d and c - d, respectively. The trace obtained by convolving the wavelet with the double spike will differ from that obtained using the single spike by an amount which is everywhere negligible in comparison to the noise in the seismogram. As noted earlier with the noise-free data, the insufficiency of reliable data is also a contributing factor to this "splitting". If splitting is taken into account, the amplitude recovery is often better than it appears at first glance because the amplitude of a split spike should be regarded as the sum of the amplitudes of its components. At relatively high noise levels the entire amplitude of a spike may be assigned to an adjacent time, i.e., the spike in the output is shifted by one time interval with respect to the location of the corresponding spike in the true response function.

2.6.1 EXAMPLE 3

The time series in Figure 2-3a was obtained by the addition of 10 percent random noise to the synthetic seismogram in Figure 2-1c. As in the previous example, the similarity of the

amplitude spectra in Figures 2-3b and 2-1d testify to the reliability of the data in the frequency band of the wavelet.

Variant Ie (inequality constraints with empirical cutoff and uncertainties): Setting cutoff K to 0.2 $\{|X(\omega)|\}$ max and uncertainty ϵ to 0.015 $\{|X(\omega)|\}$ max, the spike train depicted in Figure 2-3c was returned. This solution exhibits a highly satisfactory degree of agreement with Figure 2-1b. The most significant effect of the errors has been to alter the separation of the third and fourth spikes.

Variant Is (inequality constraints with statistical cutoff and uncertainties): The spikes series depicted in Figure 2-3d was computed using the parameter values $\alpha = 3$ and $\beta = 3$. There is good correspondence with the generating spike series (Figure 2-1b), although a small spurious spike has appeared at time 7 and the spike at time 25 has been shifted by one time unit. Some of the spikes have been split, especially that at time 42.

Variant Es (equality constraints with statistical cutoff): The estimate of a(t) obtained using the equality constraint formulation with $\alpha = 0.2$ is shown in Figure 2-3e; there is very good agreement with Figure 2-1b. A small α [and hence, by equation (2.9), a low cutoff] was adopted in order to demonstrate the superior noise tolerance of this formulation; notwithstanding the considerably lower cutoff, the output in Figure 2-3e is free of spurious spikes, in contrast to Figure 2-

3d.

2.6.2 EXAMPLE 4

The complicated wavelet (Figure 2-2a) employed in this second example is that used previously by Wiggins (1978). The synthetic earth response in Figure 2-2b includes eight spikes in an interval of approximately four-fifths of the length of the wavelet; in the presence of noise, therefore, this example taxes the resolving power of any deconvolution method. The seismogram in Figure 2-4a was constructed by the addition of 10 percent random noise to the trace in Figure 2-2c. The similarity between the amplitude spectra of the noisy and noise-free seismograms at low frequencies (Figures 2-4b and 2-2d) justifies our reliance on the data at those frequencies. The dashed horizontal line in Figure 2-4b represents a possible cutoff level. Note that the reliable frequencies in this case do not lie in a single continuous band, but are derived from a number of narrow bands; this illustrates the fact that the distribution of reliable frequencies is unimportant.

Variant Ie: The response function obtained with $K = 0.2 \max \{|X(\omega)|\}$ and $\epsilon = 0.01 \max \{|X(\omega)|\}$ is shown in Figure 2-4c. Except for the small spike at time 10, all the spikes in Figure

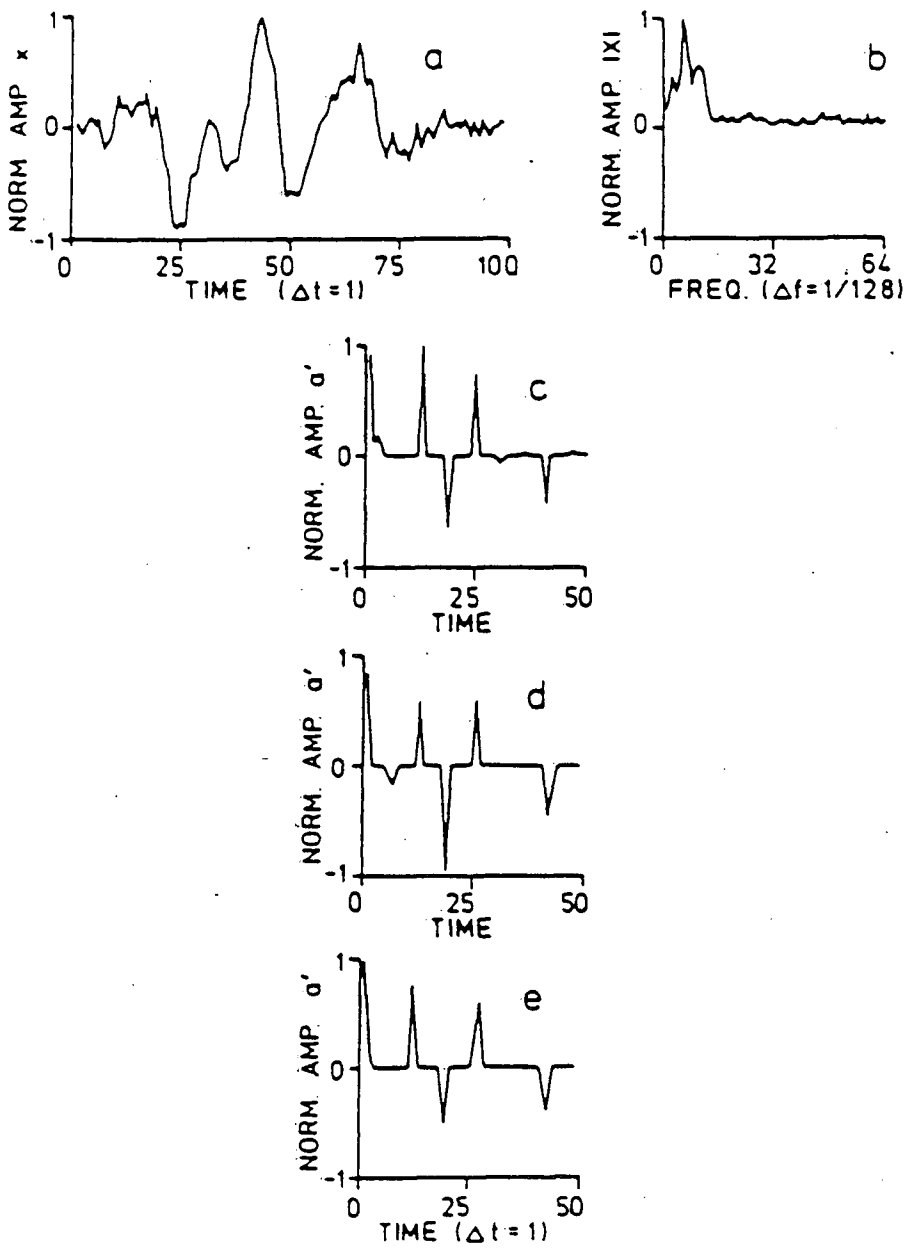

Figure 2-3

(a) Noisy input trace resulting from the addition of 10 percent random noise to the trace in Figure 2-1c. (b) Normalized amplitude spectrum of the trace shown in (a). At low frequencies this spectrum bears a strong resemblance to that for the noise-free seismogram (Figure 2-1d). (c) Normalized response function recovered from the reliable data using variant Ie. (d) Reconstructed response function obtained by application of variant Is with α = 3 and β = 3. (e) Normalized estimate of the response function determined with variant Es when α = 0.2.

2-2b have been located to within one time interval. There is some indication of the spike at time 10, but this is much smaller than the spurious spike at time 44. Since the fourth spike is split, its effective amplitude is in fact very similar to the amplitude of the third spike.

Variant Is: The spike series shown in Figure 2-4d was obtained with $\alpha = 2.5$ and $\beta = 1$. Six of the spikes in Figure 2-2b have been recovered faithfully. However, the spikes at 17 and 21 have been replaced by a single large spike spread over times 18 and 19, and a small spurious spike has been introduced at time 47.

Variant Es: When $\alpha = 0.2$, the equality constraint formulation returns the response function shown in Figure 2-4e. Six of the spikes in Figure 2-2b have been recovered, and no spurious spikes have been introduced. The net influence of the errors has been to mask the presence of two small spikes at times 10 and 40, as well as causing some splitting.

2.7 PRACTICAL RECOMMENDATIONS

When using the linear programming technique to deconvolve noisy seismograms, the following points deserve special consideration.

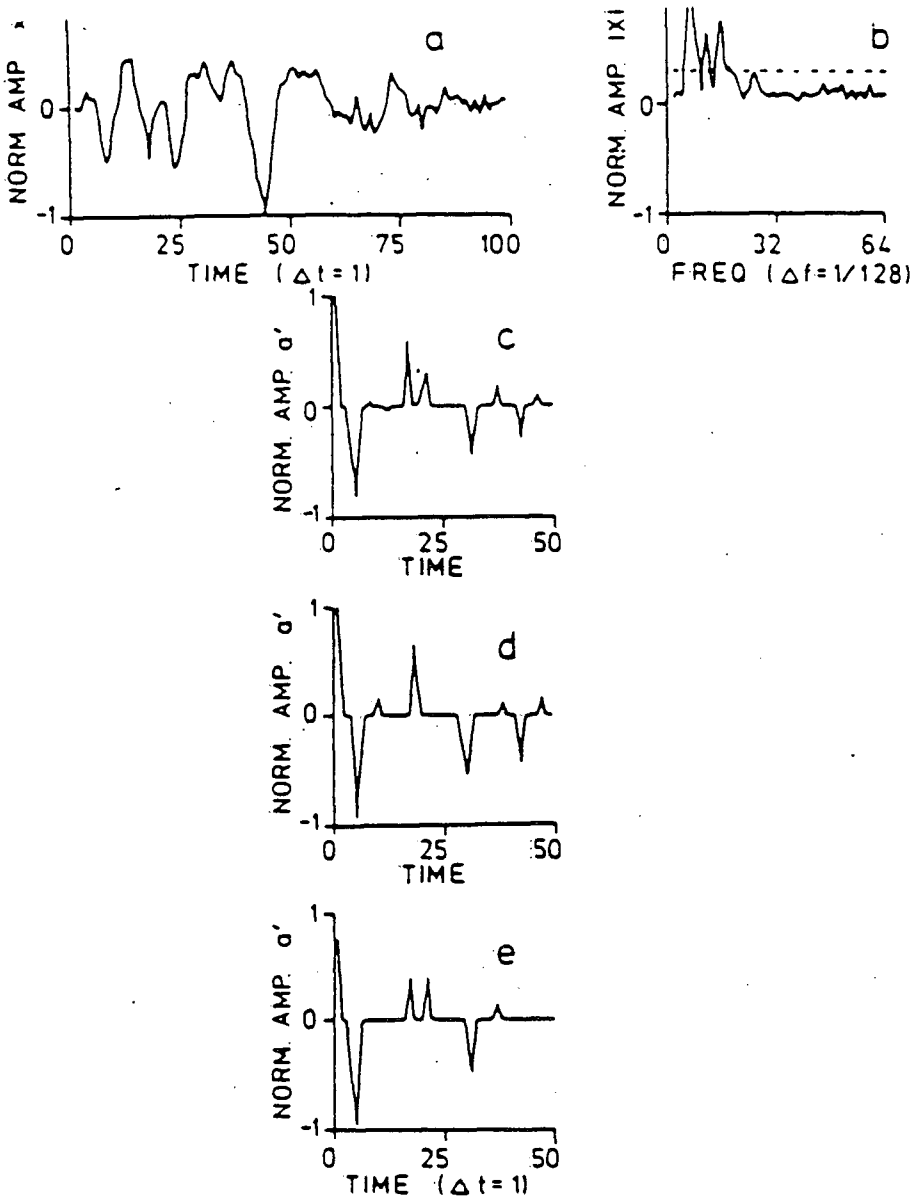

Figure 2-4

(a) Noisy input trace obtained by adding 10 percent random noise to the trace in Figure 2-2c. (b) Amplitude spectrum of the trace depicted in Figure 2-4a. The high-energy portions of this spectrum bear a close resemblance to the corresponding portions of the noise-free spectrum (Figure 2-2d). (c) Normalized reconstructed response function furnished by the empirical variant Ie. (d) Response function estimate computed using variant Is with α = 2.5 and β = 1. As for (c), there is good agreement with the generating spike series (Figure 2-2b). (e) Normalized response function recovered using the equality constraints variant Es, with α = 0.2.

(1) The computing costs increase if the algorithm is required to satisfy the data more precisely. The accuracy of solution is governed by the magnitude of the uncertainties when using inequalities, or by the prescribed noise level for equality constraints. If the accuracy demanded is inconsistent with the actual level of noise in the data, the Simplex algorithm will perform many iterations before it can locate the solution with minimum L_1-norm. If an unjustifably close fit is demanded, the solution obtained will be characterized by an unreasonably large number of spikes. At the other extreme, large uncertainties facilitate solution in a small number of iterations and at a correspondingly lower cost. However, only the most prominent spikes will be recovered, and their amplitudes may be underestimated.

In order to avoid needless computation, it is recommended that if possible a statement be introduced into the linear programming routine to terminate execution when the objective function exceeds a certain limit. If the maximum amplitude of the seismogram is normalized to unity, the upper limit on the L_1-norm should constitute a conservative estimate of the number of spikes expected.

(2) Identification of contaminated frequencies is a valuable aid in the determination of the spiky series, and it is recommended that a record of the background noise in the study

area be acquired. In conjunction with some knowledge of the frequency band of the wavelet, the spectrum of the noise indicates which frequencies should be omitted. Furthermore, a knowledge of the noise guides the choice of uncertainties to be assigned to the reliable spectral data.

2.8 COMPARISON WITH LEAST-SQUARES TECHNIQUES

In order to compare the linear programming method with conventional techniques, the examples have been repeated using (1) a least-squares frequency domain filter (Berkhout 1977) and (2) a least-squares time domain filter (Wood et. al., 1978).

In terms of the notation adopted here, the frequency domain filter $F(\omega)$ is defined by

$$F(\omega) = \frac{W^*(\omega)}{W(\omega)W^*(\omega) + c^2} \qquad (2.14)$$

where W^* denotes the complex conjugate of W. The "water-level" parameter c is adjusted according to the level of noise; c is zero for perfect data and is increased as the level of noise rises.

The time domain filter f(t) is defined by

$$f(t) = w(-t)*w^{-1}(t)*w^{-1}(-t), \tag{2.15}$$

where w^{-1} is the zero-delay Wiener inverse of w, and where the argument $-t$ is used to denote time reversal. Noise suppression is achieved in this case by the addition of a constant c' to the main diagonal of the autocorrelation matrix which features in the determination of w^{-1} (Berkhout, 1977). The higher the level of noise, the larger the value of c' adopted.

2.8.1 EXAMPLE 5

To provide a point of reference, the frequency domain filter was first applied to the noise-free trace in Figure 2-1c, using the wavelet in Figure 2-1a as before. The output (Figure 2-5a) is an exact replica of the generating spike sequence (Figure 2-1b, p-15), as expected. When the filter in equation (2.14) was applied to the noisy seismogram in Figure 2-3a, the response function shown in Figure 2-5b was obtained. In this case the most suitable value of c^2 was found to be 0.01 max $\{|W(\omega)|^2\}$, consistent with the known 10 percent noise level. The output in Figure 2-5c, on the other hand, resulted when the time domain filter was applied to the same example with $c' = 0.1R_0$, where R_0 denotes the zero lag autocorrelation. Substantial

delays have been caused by the successive convolutions performed during filter construction.

Comparing Figures 2-3c, 2-3d, and 2-3e with Figures 2-5b and 2-5c, it is clear that the linear programming method provides a much more highly resolved output than the conventional least-squares techniques.

2.8.2 EXAMPLE 6

As for the previous example, the frequency domain filter for the wavelet in Figure 2-2a was first applied to the exact seismogram in Figure 2-2c, and the original spike series (Figure 2-2b) was reproduced perfectly (Figure 2-6a). Subsequently, the same filter was applied to the noisy seismogram in Figure 2-4a; the most appropriate value of c^2 was found to be 0.02 max $\{|W(\omega)|^2\}$, and the resulting output is presented in Figure 2-6b. When the time domain filter was applied to the noisy trace with $c' = 0.05R_0$, the response function in Figure 2-6c resulted.

Comparison of Figures 2-4c, 2-4d, and 2-4e with Figures 2-6b and 2-6c reveals that the linear programming output is much more highly resolved than the corresponding output obtained using the conventional filters [equations (2.14) and (2.15)].

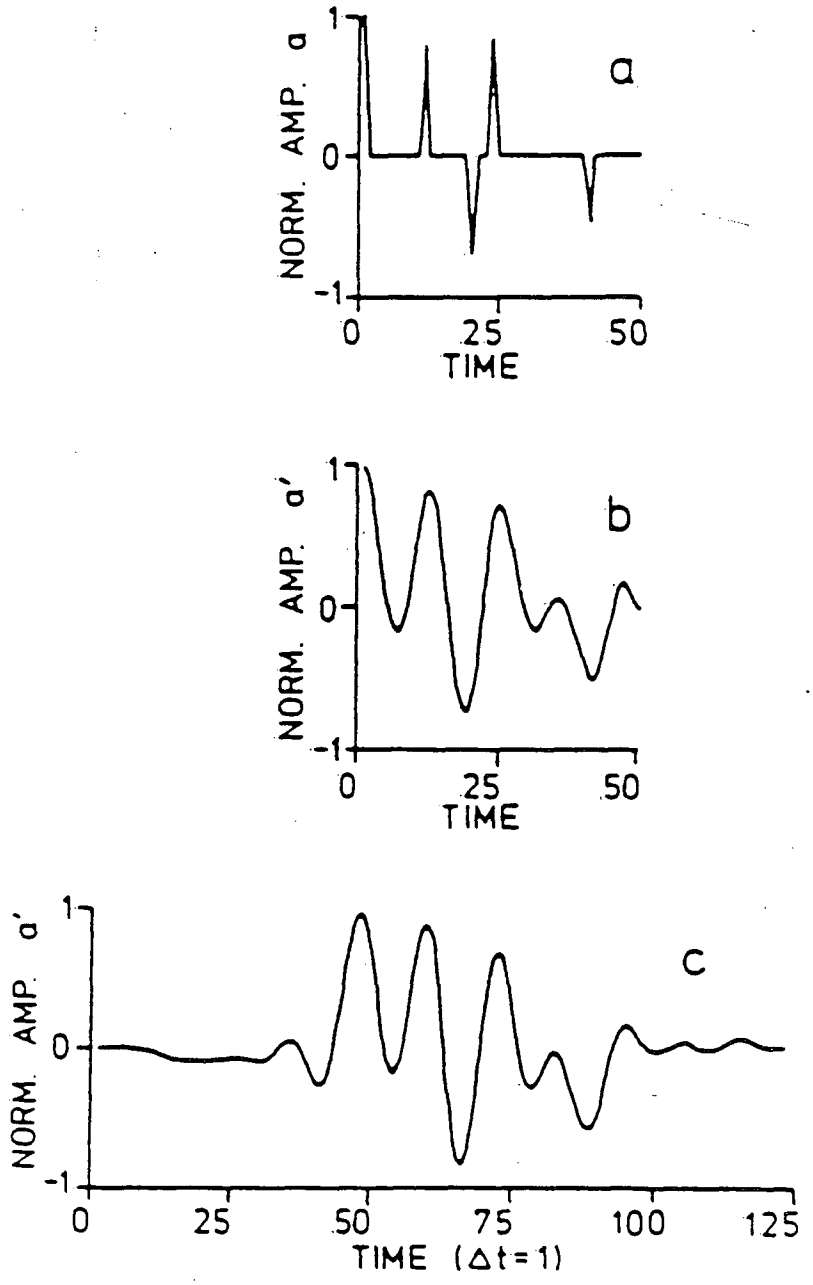

Figure 2-5

(a) Normalized reconstructed response function obtained by applying the frequency domain filter (2.14) to the noise-free seismogram in Figure 2-1c. (b) Normalized response function recovered from the noisy seismogram in Figure 2-3a using the frequency domain filter with $c^2 = 0.01 \max\{|W|^2\}$. (c) Reconstruction of response function resulting from application of the time domain filter (2.15) to the trace in Figure 2-3a, with $c' = 0.1R_0$.

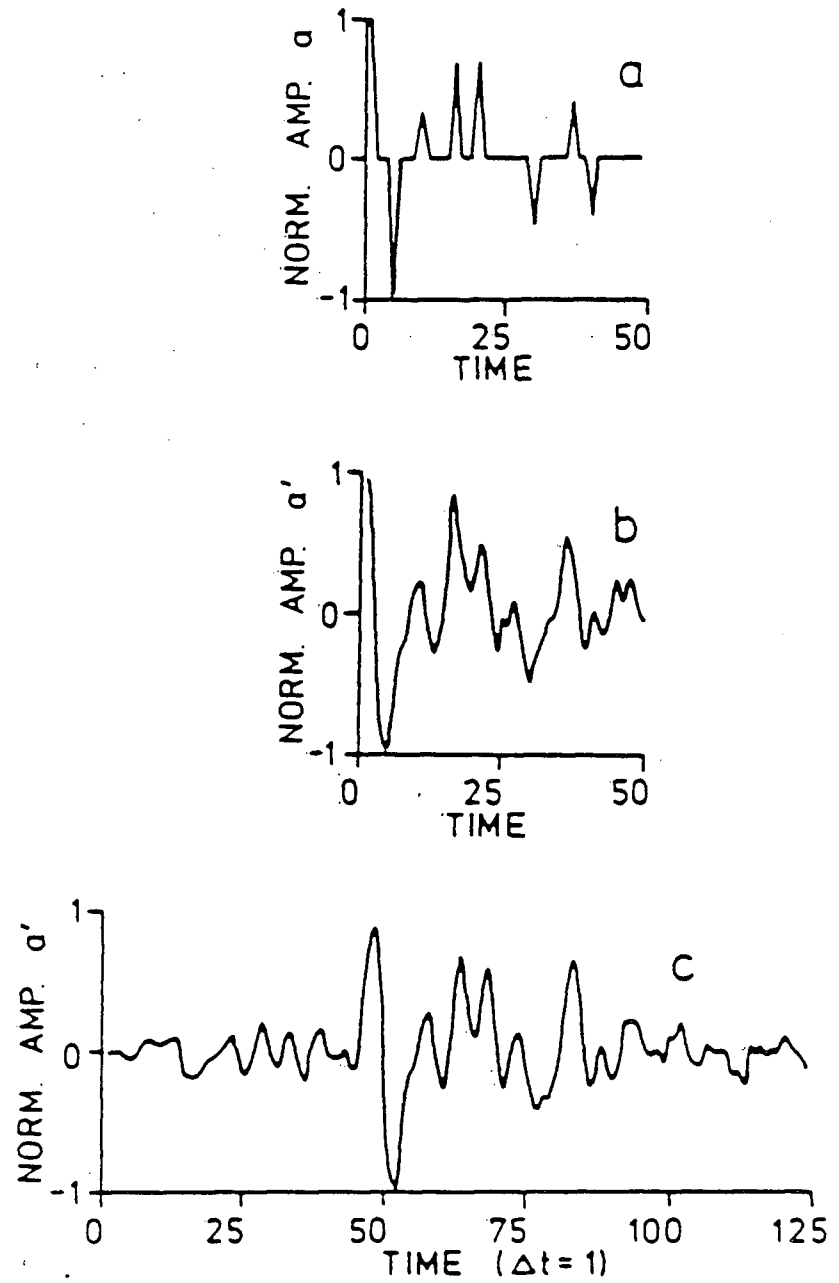

Figure 2-6

(a) Normalized reconstructed response function obtained by applying the frequency domain filter (2.14) to the noise-free seismogram in Figure 2-2c. (b) Normalized response function recovered from the noisy seismogram in Figure 4a using the frequency domain filter with $c^2 = 0.02 \max \{|W|^2\}$. (c) Reconstruction of response function resulting from application of the time domain filter (2.15) to the trace in Figure 2-4a, with $c' = 0.05R_0$.

2.9 CONCLUSIONS

Using a linear programming formulation, we have shown that it is possible to reconstruct a spiky signal from a small portion of its Fourier spectrum. The recovered signal bears a close resemblance to the original spike sequence. The minor differences which can sometimes be observed are manifestations of the non-uniqueness inherent in any underdetermined linear inverse problem.

To test its effectiveness in the presence of noise, the reconstruction method has been applied to the seismic deconvolution problem when the wavelet is known. The influence of noise has been suppressed by discarding those spectral data which are most seriously contaminated and by including only the remaining reliable data in the computations. Furthermore, when solving for the spike amplitudes, the reliable data are not satisfied exactly but rather to an accuracy consistent with the perceived level of noise. In synthetic examples with 10 percent random noise, this method has produced highly resolved deconvolved traces. In each case the output bears a close similarity to the generating spike sequence.

Although the effect of random errors in deconvolution has been considered in some detail, the reconstruction method is readily adaptable to other types of noise. Large amplitude sinusoidal noise, for example, would produce a very obvious

signature in the frequency domain, thus facilitating recognition (and subsequent rejection) of unreliable frequencies.

The deconvolution method proposed here is simple to implement, given the wide availability of linear programming routines. Although we have not conducted a serious study of comparative costs, it is to be expected that the linear programming method will be somewhat more expensive than most existing deconvolution techniques. However, any additional expense is offset by the high quality of the linear programming output, consisting as it does of spikes separated by zeros, in contrast to the broadened peaks and side lobes which typify conventional least-squares deconvolution.

CHAPTER III: ACOUSTIC IMPEDANCE INVERSION AND WELL-LOG CONSTRAINTS

3.1 INTRODUCTION

The following is a short summary of some of the essential points brought up by Scheuer (1981) and Oldenburg et al. (1983). For complete details the reader is referred to the original papers.

Geological environments which are characterized by a relatively small number of sharp impedance discontinuities are likely to produce reflectivity functions which are well approximated by sparse spike trains. In such environments, the full-band reflectivities produced by linear programming (LP) deconvolution constitute a good representation of the true earth reflectivity function and can be subsequently used for the calculation of the acoustic impedance function. As shown by Peterson et al. (1955) and Waters (1978, p. 219), the relationship between the reflectivity function r(t) and the acoustic impedance $\xi(t)$ is approximately:

$$r(t)=1/2\ d[\ln\ \xi(t)]/dt \qquad (3.1)$$

This approximation is acceptable for reflection coefficients smaller than 0.3, in which case we may write:

$$\xi(t)=\ \xi(0)\ \exp\ [2\ \int_{o}^{t} r(u)\ du] \qquad (3.2)$$

or after taking the logarithm of (3.2):

$$\eta(t)=\ \ln\ [\xi(t)/\xi(0)]\ =\ 2\ \int_{o}^{t} r(u)\ du \qquad (3.3)$$

From equation (3.3) we see that seismogram inversion can be readily achieved if full-band, multiple-free seismograms are available. The remainder of this work is dedicated to the development of tools which will allow reliable reconstruction of full-band reflectivity sections from the observed band-limited stacked sections.

We start by stating that the straight forward technique presented in chapter II is not sufficient to ensure successful inversion. Although a fairly large number of geological environments conform with the sparse reflectivity assumption, an even larger number will contain at least a number of time windows in which this assumption is violated. Consider for example a geological environment containing a number of transition zones characterized by a slowly changing impedance function. Such transition zones give rise to a densely populated

reflectivity series which cannot be described as sparse. Consequently, the reflectivities obtained by the LP deconvolution are not expected to constitute a good representation of the true earth reflectivity and hence their conversion to log relative impedance (Equation 3.2) will not yield meaningful results. To overcome this problem and increase the reliability of the obtained impedance section it is necessary to introduce additional information into the inversion process.

The target of this chapter and Chapter IV is the generation of a complete set of linear relations combining information from the stacked section, the sonic well-log and the stacking velocities. This set is subsequently solved to yield a full-band reflectivity function which is consistent with all the available information.

3.2 EXTERNAL CONSTRAINTS IN IMPEDANCE INVERSION

External information about the reflectivity can be introduced into the inversion if the corresponding knowledge can be expressed in the linear form:

$$a_i = \sum_{j=1}^{N} A_{ij} \cdot r_j \qquad (3.4)$$

For each such constraint, a and all the A 's must be known. The possibility that a is not known exactly can be handled by specifying only its bounds, to within the desired uncertainty. That is,

$$a_i - \delta_i \leq \sum_{j=1}^{N} A_{ij}\, r_j \leq a_i + \delta_i \qquad (3.5)$$

The full set of equations contains a number of Fourier transform inequalities (as per eqation 2.11) plus external constraints of the form specified in equation (3.5) above.

3.3 POINT VELOCITY CONSTRAINTS-WELL LOG INFORMATION

When well-log information is available, its cautious incorporation into the inversion is highly desirable. In this section we develop the set of relations required for this operation. For the purpose of the following development we model the digitized reflectivity function as a Dirac comb, we write:

$$r(t) = \sum_{n=0}^{N-1} r_n\, \delta(t-n\Delta) \qquad (3.6)$$

where, δ symbolizes the Dirac delta function,
and Δ the sampling interval.
Substituting equation (3.6) into (3.3), exchanging the order of

summation and integration, and integrating the result term by term, we get:

$$\eta(t) = 2 \sum_{n=0}^{N-1} r_n \, H(t-n\Delta) \qquad (3.7)$$

with H denoting the Heaviside step function.

Equation (3.7) states that the logarithm of the relative impedance at time 't' is equal to twice the sum of the reflection coefficients in the time window zero to 't' seconds. This equation allows constraints to be applied to the constructed reflectivity if the density and velocity are known for specific two-way travel times.

In general, we assume that both r(t) and $\eta(t)$ are not known accurately; hence, a constraint at a given time 't' is of the form:

$$\eta(t) - \delta\eta(t) \leq 2 \sum_{n=0}^{N-1} r_n \, H(t-n\Delta)$$

$$\text{and} \quad \eta(t) + \delta\eta(t) \geq 2 \sum_{n=0}^{N-1} r_n \, H(t-n\Delta) \qquad (3.8)$$

with $\delta\eta(t)$ being the estimated error.

One can also assume a density power law, such as:

$$\rho(t) = \text{constant } [v(t)] \qquad (3.9)$$

with v(t) being the velocity versus two-way travel time profile.

Invoking this assumption equation (3.7) becomes:

$$\eta(t) = \ln [v(t)/v(0)] = [2/(1+a)] \sum_{n=0}^{N-1} r_n H(t-n\Delta) \qquad (3.10)$$

3.4 DISCUSSION

The importance of external constraints in the reconstruction of full-band reflectivity functions cannot be overemphasized. In a normal seismic experiment the acquired data is characterized by a relatively narrow frequency band and hence the construction of full-band reflectivity functions is a strongly underdetermined inverse problem. Consequently, the technique presented in chapter II will attain an acceptable solution only if the true earth reflectivity function is well approximated by a sparse spike series. The incorporation of the velocity constraints into the inversion reduces the allowed solution space and relaxes the strictness of the conditions previously imposed on the sparseness of the constructed reflectivity function. For example, the problem of a reflectivity function which includes a number of transition zones in an otherwise sparse reflectivity background can now be tackled with very encouraging results. Furthermore, the inversion of properly scaled stacked seismograms supported by the corresponding well-log information can be translated directly into physically meaningful impedance or pseudo-velocity functions, thereby supplying valueable information for

quantitative interpretation of the observed data.

CHAPTER IV: RMS VELOCITIES AND RECOVERY OF THE ACOUSTIC IMPEDANCE

4.1 INTRODUCTION

The paper by Oldenburg, Scheuer, and Levy (1983) (hereafter referred to as OSL) investigated the problem of recovering the acoustic impedance from normal incidence reflection seismograms. That work began by using the simple convolutional model for a reflection seismogram

$$x(t)=r(t)*w(t) \tag{4.1}$$

where $x(t)$ is the seismogram, $r(t)$ is the reflectivity function, $w(t)$ is the source wavelet, and the symbol * denotes the convolution operation. If $v(t)$ is an inverse filter which shapes $w(t)$ "as well as possible" into a Dirac delta function, then the best estimates for $r(t)$ are the unique averages

$$\langle r(t)\rangle=r(t)*a(t) \tag{4.2}$$

where $a(t)=w(t)*v(t)$ is called the averaging function. Note that $a(t)$ is bandlimited because $w(t)$ is, and hence $\langle r(t)\rangle$ is, at best, a band-limited representation of the reflectivity function. The consequences of integrating $\langle r(t)\rangle$, or using its discretized form in the standard acoustic impedance recursion

formula, was shown to yield a band-limited representation of the true impedance. More precisely, it was shown that only averages

$$\langle \eta(t) \rangle \simeq \eta(t) * a(t) \qquad (4.3)$$

could be recovered. In equation (4.3), $\eta(t)=\ln(\xi(t)/\xi(0))$ where $\xi(t)$ is the acoustic impedance at time t, and a(t) is the same band-limited averaging function that was obtained in deconvolving the initial seismogram. The loss of the low frequencies makes a geological interpretation of $\langle \eta(t) \rangle$ very difficult.

The solution offered by OSL was to abandon the appraisal technique which yields unique averages of the acoustic impedance and instead, attempt to construct a broadband reflectivity function which reproduced the seismic data. The basic difficulty with such an approach is the inherent nonuniqueness in the solution. There exists an infinity of acceptable models and these can differ greatly from one another. This nonuniqueness can be conquered only if model space is restricted sufficiently so that the only acceptable models are like the true earth and differ from each other in at most small scale features. In OSL, model space was restricted by first introducing the layered earth so that the reflectivity function was represented as

$$r(t) = \sum_k r_k \delta(t-\tau_k) \qquad (4.4)$$

In equation (4.4) r_k is the reflection coefficient at the base

of the k'th layer, and τ_k is the two-way travel time to that layer.

Clearly r(t) as represented by equation (4.4) has the potential for being broadband since a delta function has energy at all frequencies. Moreover, an acoustic impedance having a minimum of structural detail can be found by constructing an r(t) in the form of equation (4.4) which has the fewest number of layers. This led to the development of two solutions. The first was a linear programming (LP) algorithm which minimized

$$\phi = \int |d\eta(t)/dt| \, dt = 2\sum_k |r_k| \tag{4.5}$$

The LP computations were carried out in the frequency domain using the method of Levy and Fullagar (1981). That algorithm constructs a broadband reflectivity whose spectrum agrees with the measured spectrum within the energy band of the wavelet, and has a spectrum consistent with that of equation (4.4) outside the band. The second solution modelled the Fourier transform of the reflectivity function as an autoregressive (AR) process and predicted unmeasured portions of the reflectivity spectrum from the spectral values within the band of the wavelet.

It was found that the nonuniqueness could be further controlled by introducing additional constraints into the construction algorithms. The LP solution was particularly

amenable to such modification. OSL were able to use the unique averages of the reflectivity function to constrain the polarity of the reflection coefficients and also to weight the objective function so that sizeable reflection coefficients would not appear at those times where the unique averages indicated they should not. Lastly, and importantly, they also showed how impedance constraints could be incorporated directly into the solution. In extending the autoregressive approach, Walker and Ulrych (1983) showed how the original AR formulation could be modified so that it also could include impedance constraints. Thus, impedance information from a nearby well, an estimate of a basement impedance, or a recognized marker zone with known impedance could be input directly into the LP or AR algorithms.

It would seem that such constraints would so restrict model space that the only nonuniqueness would be relegated to ambiguity of fine scale structure. OSL showed that this often appears to be the case when the earth is adequately modelled by a set of homogeneous layers. However, there are numerous instances when a layered earth is not justified because the impedance changes slowly and continuously with depth. Such transition zones or 'ramps' can cause problems with the construction procedures because

$$r(t) \simeq 1/2 \; d/dt \; [\; \ln\{\xi(t)/\xi(0)\}]$$

can be arbitrarily small if $d\xi(t)/dt$ is sufficiently small. Slow changes in the impedance therefore produce very small

reflections and hence such changes are essentially annihilators for the reflection seismic problem; that is, they are functions which produce no observable data. Large components of such annihilators can be added to any acceptable reflectivity function without degrading substantially the misfit to the data. Clearly, more information is required to control this form of nonuniqueness. A major purpose of this chapter is to show how extra information derived from RMS (stacking) velocities can be incorporated directly into the LP and AR algorithms.

There are two ways in which RMS velocities can be included in the construction algorithms. The first, and simplest, would be to compute a minimum structure velocity function from the RMS velocities and then incorporate approximate impedance constraints directly by setting the density equal to unity and prescribing $\xi(t)=v(t)$ as point constraints in the construction algorithms. This method has the potential for producing good results but it brings to light a problem of fundamental importance. The RMS velocities are averages of the interval velocity $v(t)$, but knowledge of only a few inaccurate RMS velocities does not permit one to place pointwise bounds on $v(t)$. Mathematically, $v(t)$ can have any value at a particular time, but physically, it is constrained within the limits imposed by the available geological lithologies. In principle therefore, it is not possible to estimate errors for $v(t)$ and hence it is generally poor practice to incorporate impedance constraints inferred directly from a constructed model.

An alternative method is possible. Its basis is the

realization that the RMS velocities are averages of the interval velocity and therefore the only unique information available is encompassed in the averages $\langle v(t) \rangle$. Our goal will be to investigate these averages and show how information contained in them can be used to produce constraints for the LP and AR construction algorithms.

The development of the solution to our objective is divided into three sections. We begin by inverting RMS velocities to recover information about the interval velocity. Algorithms for computing flattest L_1 (absolute value) and L_2 (least squares) norm models will be presented. Both of these algorithms are stable when applied to noisy data and both can incorporate known constraints on the velocity. The next stage involves use of the linear appraisal methods of Backus and Gilbert (1970) to summarize our information about the interval velocity. This analysis quantifies the loss of resolving power at increased time along the record and also illustrates the importance of data errors. The final section shows how to include the information contained in the RMS velocities into the acoustic impedance construction algorithms. This is done by first constructing an acceptable interval velocity model and then using linear appraisal to obtain unique averages of $v^2(t)$ or $v(t)$. The desired constraints, in the form of linear combinations of the reflection coefficients, can be computed directly with that information.

4.2 : INVERSION OF RMS VELOCITIES: MODEL CONSTRUCTION

In this section we shall show how to construct an interval velocity model from a given set of RMS velocities. This problem has been addressed in a large number of publications over the last three decades [c.f. Dix (1955), Taner and Koehler (1969), Taner et al. (1970), Levin (1971), Schneider (1971, Everett (1974), Krey (1976), and Hubral and Krey (1980)], but our approach will be somewhat different. In particular we shall show how observational errors and point velocity constraints can be incorporated directly into the construction of an interval velocity. Also, we present two construction algorithms: one produces a continuous velocity structure, and the other generates a layered earth with transition zones. The flexibility afforded by these algorithms allows one to generate many different types of velocity structures which fit the observations. The interpreter can therefore choose that algorithm (and adjustable parameters) which develops an interval velocity structure coinciding with the desired type of geological stratification.

Our methods incorporate errors from the outset and consequently it is important to understand their sources and magnitudes. An excellent description of the possible sources of error associated with the estimation of stacking velocity is given in Hubral and Krey (1980). There are two principal types of errors: those which result in biased stacking velocity estimates, for example, signal bandwidth (Stone, 1974) and

spread-length bias (Al-Chalabi, 1974); and those which result in random errors (such as statics, event interference, etc). In most of the following work we shall assume that the total observational inaccuracy of each datum can be represented by a Gaussian random variable with zero mean. However, in the linear programming construction, biased errors are included in a natural way.

We begin by casting the problem in an appropriate framework, that of linear inverse theory. The basic equation relating the RMS velocity V(t) to the interval velocity v(t) is

$$V^2(t) = 1/t \int_o^t v^2(u)du \qquad (4.6)$$

When the RMS velocities are known only at discrete times t_j, j=1,N, the apppropriate equations are

$$V_j^2 = V^2(t_j) = 1/t_j \int_o^{t_j} v^2(t)dt \qquad j=1,N \qquad (4.7)$$

The objective of a construction algorithm is to find a model v(t) which satisfies the N equations (4.7) to a degree consistent with the assumed statistical errors on V_j. This is easily accomplished by minimizing some norm of the model while using equations (4.7) as constraints. A variety of useable norms are available but our selection is motivated by a desire to construct a model that has a minimum of structural detail. The two norms used here are

$$\phi_1 = \int_0^{t_m} w(t)|m(t)|dt \tag{4.8}$$

and

$$\phi_2 = \int_0^{t_m} w(t)m^2(t)dt \tag{4.9}$$

where

$$m(t)=dv^2(t)/dt \tag{4.10}$$

In these equations t_m is the maximum record time, and $w(t)$ is a positive weighting function which we shall later adjust to suit our needs. Both ϕ_1 and ϕ_2 involve the gradient of $v^2(t)$ and hence minimizing either of these will produce a constructed velocity model with few oscillations.

To begin the construction we first integrate equation (4.7) by parts and use (4.10) to obtain

$$V_j^2 - v^2(0) = \int_0^{t_m} 1/t_j \cdot (t_j - t)H(t_j - t)m(t)dt \tag{4.11}$$

where $H(t)$ is the Heaviside step function. Another datum equation can be found by integrating (4.10) to get

$$v^2(t_k) - v^2(0) = \int_0^{t_m} m(t)H(t_k - t)dt \tag{4.12}$$

Equation (4.12) is important if some a priori knowledge about the velocity at time t_k is available. It will permit us to construct interval velocities subject to point constraints.

A constructed velocity model can be obtained by minimizing either ϕ_1 or ϕ_2 subject to using equations (4.11) and/or (4.12) as constraints. The velocity obtained by minimizing ϕ_1 will be referred to as the flattest L_1 norm model, while the model obtained by minimizing ϕ_2 will be called the flattest model.

A velocity structure which will be used as a common example throughout this investigation is shown in Fig. 4-1a. The corresponding RMS velocities, computed from equation (4.6), and the reflection seismogram, bandlimited to 10-35 Hz, are shown in fig. 4-1b and 4-1c, respectively. Seventeen RMS data were selected at times coinciding with large reflection events; the times and velocities are given in Table 4-1 and indicated by arrows in Fig. 4-1c.

To begin the constructions we shall compute the flattest model. This is accomplished by using a standard spectral expansion technique. Since the method is well known, it will not be outlined here. However, a reader who is unfamiliar with the approach is referred to Parker (1977) for details and to Oldenburg and Samson (1979) or OSL (1981) for typical applications.

The flattest model which reproduces the accurate RMS data is shown in Fig. 4-2a. The true velocity is superposed upon the constructed model and it is apparent that the flattest model is

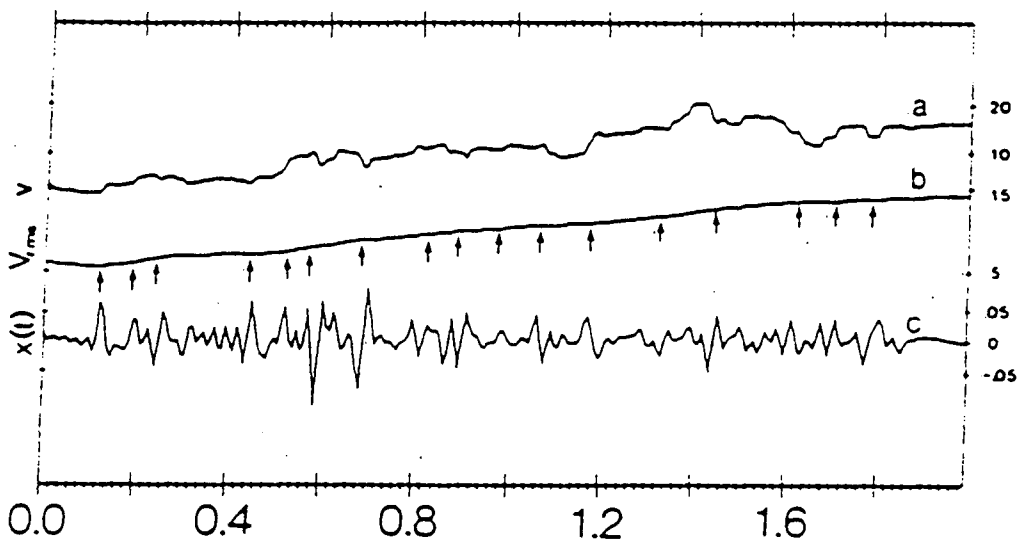

Figure 4-1

The true velocity structure is shown in (a). The RMS velocities corresponding to the velocity in (a) are shown in (b). The arrows indicate those RMS velocities that will be used in the inversion. For both (a) and (b) the scales on the right are in kft/sec. The reflection seismogram, bandlimited to 10-35 Hz. is shown in (c).

a good approximation to the true model.

The flattest model norm expression for ϕ_2 (equation 4.9) includes a weighting function w(t). That such a function might be useful arises from the following observation. The flattest model is that one whose gradient (squared) is as small as possible. Yet stacking velocities can be obtained only when there is a significant reflection, and that is at times corresponding to large gradients in impedance. This physical information can be incorporated by designing a weighting function which is small (significantly less than unity) near times t corresponding to stacking velocity data, and unity at other times. The weighting function used here is a sum of Gaussians. We have chosen

$$w(t) = \max\{1 - \Sigma\, c\, \exp[-\gamma(t-t\,)^2]\ ,w\quad\}$$

(4.13)

where the coefficients c control the amplitude of the weighting, γ controls its width, and w is a parameter which prevents the weighting from getting too small. In practical applications reasonable estimates of c and γ may be inferred directly from the velocity analysis diagram. For the current example, the effects of admitting a Gaussian weighting with $c = 0.9$ and $\gamma = 1000$ are shown in Fig. 4-2c. The resultant velocity structure is more 'blocky' than that given in Fig. 4-2a, and is very similar to the Dix result. This is expected. As c approaches 1.0 and for sufficiently small w and

sufficiently large γ_j, large gradients will be permitted only at the RMS times t_j. These are the same times at which the velocities can change with the Dix formulation.

Lastly, the effects of incorporating six velocity constraints (see Table 4-1 for magnitudes and times) are shown in Fig. 4-2d. No Gaussian weighting was applied in this example.

The previous example shows that the flattest model construction can produce good results when the data are accurate. Real data however, are always inaccurate, and if an algorithm is to be useful it must be stable in the presence of noise. The standard Dix formula fails in this regard when applied directly to noisy data. The analytic inverse to equation (4.6) is

$$v(t) = V(t) \{1 + 2tV'(t)/V(t)\} \tag{4.14}$$

and the Dix formula is merely a discretized version of (4.14). Instability arises because errors in V(t) are greatly amplified when estimating V'(t). Moreover, the instabilites worsen with increased record time because of the linear dependence on t in the right hand side of (4.14).

To illustrate the effects of errors we shall invert RMS data obtained by adding Gaussian random noise to the true data in Table 4-1. The inaccurate data and their standard deviations

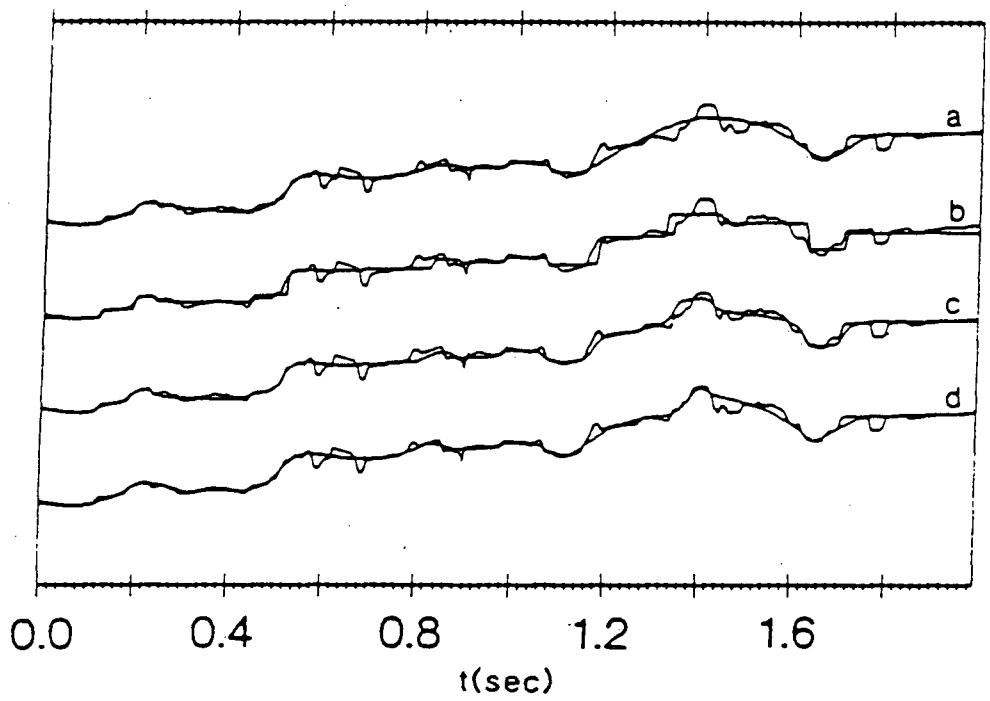

Figure 4-2

The flattest model obtained from inverting seventeen accurate RMS velocities is shown in (a). That model, as well as all others in this figure, are superposed on the true velocity structure. The model generated from the Dix formula is shown in (b). The velocity in (c) was obtained by using the flattest model formulation but weighting the norm so that large gradients could appear at those times corresponding to RMS velocity data. The flattest model constructed from the RMS data and six additional point velocity constraints is shown in (d).

	Velocity	Standard deviation
Accurate rms velocities	5.104	—
	5.556	—
	6.067	—
	6.540	—
	6.798	—
	7.405	—
	8.043	—
	8.742	—
	9.034	—
	9.397	—
	9.736	—
	9.977	—
	10.711	—
	11.544	—
	12.306	—
	12.385	—
	12.568	—
Inaccurate rms velocities	5.126	.08
	5.521	.08
	6.061	.10
	6.547	.10
	7.012	.10
	7.483	.10
	7.879	.13
	8.655	.13
	9.096	.15
	9.675	.15
	9.621	.15
	9.915	.15
	10.791	.17
	11.449	.18
	12.324	.20
	12.583	.20
	12.429	.20
Point-wise velocity constraints	6.647	.01
	12.828	.01
	11.236	.01
	20.278	.01
	13.029	.01
	16.815	.01

TABLE 4-1

The first portion of the table contains the seventeen accurate RMS velocities and their times (depicted by arrows in Fig 4-1b) corresponding to the example used in this chapter. The second portion of the table contains the seventeen inaccurate RMS velocities and their standard deviations. The last portion contains the values, standard deviations, and times of the six pointwise velocity constraints used in the inversions.

are also given in Table 4-1.

The results from inverting with the Dix formula are shown in Fig. 4-3a. Clearly, relatively small data errors have caused significant deterioration in the constructed velocity. In particular, the Dix model displays structural detail near t=1.0 seconds which is purely an artifact of the additive noise.

If an algorithm is to be robust, it must not be required to fit inaccurate data exactly. The algorithm should produce predicted responses V_j^p, which are acceptably close, but not exactly equal to, the observations V_j^o. We shall assume that the errors on the RMS velocities are independent and Gaussian with zero mean, and that the standard deviation of the jth datum is σ_j. Then

$$\chi^2 = \sum_{j=1}^{N} \{ (V_j^o - V_j^p) / \sigma \}^2 \qquad (4.15)$$

denotes the chi-squared misfit between the observations and the predicted RMS velocities. In construction, we should attempt to generate a model which has a χ^2 value that is neither too big nor too small. The expected value of χ^2 is approximately N if N is greater than about 5. A model that generates a χ^2 much less than N reproduces the observations too well and it will display features that are merely artifacts of the noise . Alternatively, a model that generates a χ^2 much greater than N has fit the data too poorly and hence information about the interval velocity which is contained in the data will have been discarded. Figs. 4-3b and 4-3e illustrate this effectively. The constructed

models have χ^2 values of 36, 17, 11 and 1. Since N=17, the preferred model based upon a χ^2 criterion is that shown in Fig. 4-3c. That velocity is a smooth representation of the true velocity and a comparison with the constructed model in Fig. 4-2b gives some insight about the loss of information due to data errors.

We shall now turn to the construction of the L_1-norm flattest model. Our goal is to minimize the norm given in equation (4.8) subject to data constraints in equation (4.11) and (4.12). We do this by first introducing a partition $\{0=\bar{t}_1, \bar{t}_2, \ldots \bar{t}_n = t_m\}$ and parameterizing m(t) such that it is a constant m_i on the i'th partition element. Equations (4.11) and (4.12) can then be written as

$$V^2(t_j) - v^2(0) = \sum_{i=1}^{n} a_{ij} m_i \qquad (4.16)$$

where $$a_{ij} = 1/t_j \int_{\bar{t}_{i-1}}^{\bar{t}_i} (t_j - t)\, H(t_j - t)\, dt$$

and $$v^2(t_j) - v^2(0) = \sum_{i=1}^{n} b_{ij} m_i \qquad (4.17)$$

where $$b_{ij} = \int_{\bar{t}_{i-1}}^{\bar{t}_i} H(t_j - t) \cdot dt$$

The discretized form of the objective function is

$$\phi_1 = \sum_i w_i |m_i| \qquad (4.18)$$

where w_i is a weight for the i'th partition element. As in the

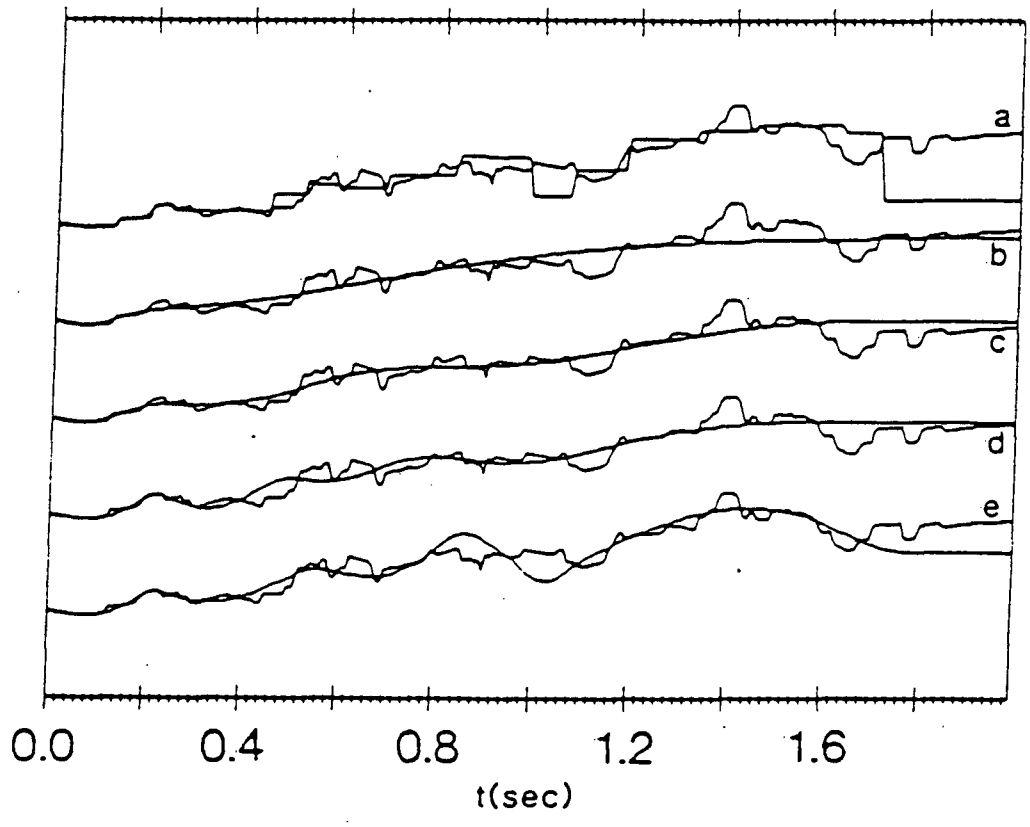

Figure 4-3

Seventeen inaccurate RMS data are inverted. The results from the Dix formula are shown in (a). Profiles in (b) - (e) represent flattest model velocity constructions whose χ^2 misfit values are respectively 36, 17, 11, and 1. The true velocity structure is superposed upon all curves.

flattest model construction, these weights can be altered to produce different models. Here, however, we shall set

$$w_i = (\bar{t}_i - \bar{t}_{i-1}).$$

This choice normalizes the changes in $d(v^2(t))/dt$ corresponding to each time interval.

The minimization of equation (4.18) subject to the constraints in (4.16) and (4.17) is easily carried out using linear programming techniques. Estimated errors in the data are readily incorporated by writing the constraints as inequalities.

If there are N data constraints, the linear programming solution will return at most N nonzero values of m, meaning that the constructed velocity model will have at most N partitions with nonzero gradients. Also by parameterizing more finely about the RMS times, t_j, we ensure that the model construction can put in large gradients of $v^2(t)$ at those times. It is expected therefore, that the L_1 norm flattest model will produce good estimates of the true velocity structure when the earth is layered.

The L_1 norm flattest model obtained by inverting the accurate RMS data is shown in Fig. 4-4a. It is noted that this model is similar to its L_2 counterpart in being generally a smooth version of the true velocity. However, it has also correctly achieved the large gradients expected near the RMS data times. The constructed model obtained by incorporating the accurate point velocity constraints is shown in Fig. 4-4b.

The stability of this algorithm in the presence of noise is illustrated in Figs. 4-4c and 4-4d. In Fig. 4-4c we have shown the model constructed from the inaccurate RMS data of Table 4-1. This result is clearly superior to that of the Dix construction on the same data, shown in Fig. 4-3a. Our results are further improved by adding inaccurate point velocity constraints; see Fig. 4-4d.

4.3 : LINEAR APPRAISAL

The construction methods provide ways to obtain a minimum structure velocity which will reproduce the observations. Yet there are infinitely many acceptable models and it is important to determine what unique information about the interval velocity can be found directly from the data. Such an appraisal analysis is carried out by using the methods of Backus and Gilbert (1970). Again, their work is well known and only the barest details will be presented here. The reader is referred to Backus and Gilbert (1970) for a theoretical basis, and to Parker (1977) or Oldenburg and Sampson (1979) for additional exposition and examples.

Given equations of the type

$$e_j = \int_0^{t_m} v^2(t) \cdot G_j(t) dt$$

(see equation (4.7)), then unique averages of the form

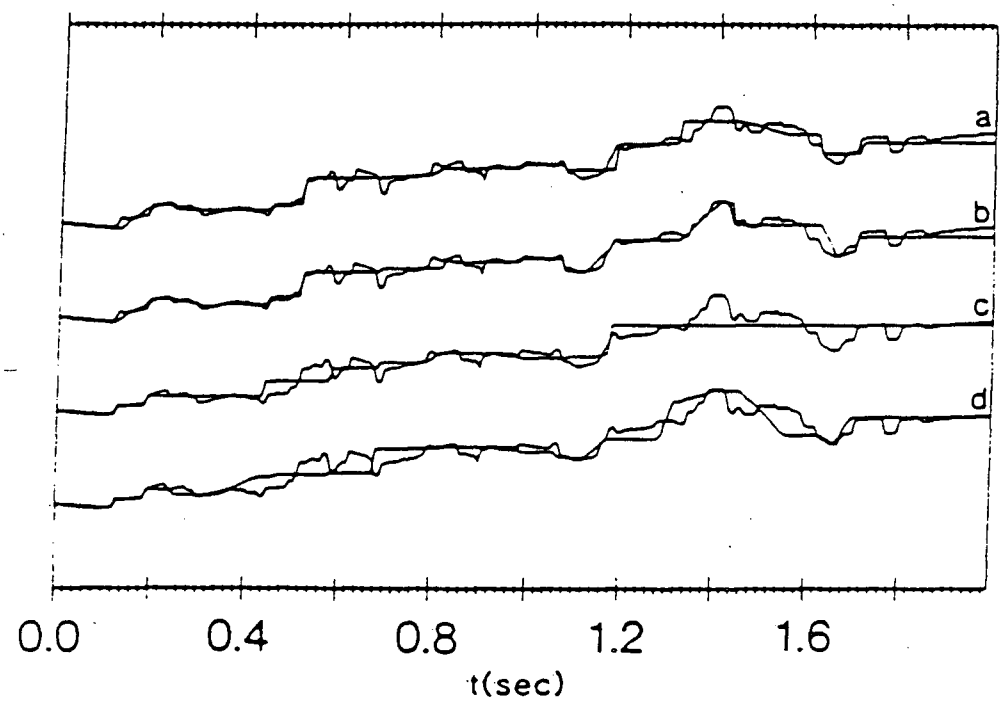

Figure 4-4

The L1-norm flattest model obtained by inverting seventeen accurate RMS velocities is shown in (a). The addition of six accurate point velocity constraints is shown in (b). Analogous results with inaccurate data are shown in (c) and (d) respectively.

$$\langle v^2(t_0)\rangle = \int_0^{t_m} v^2(t)A(t,t_0)dt \qquad (4.19)$$

can be generated by finding a set of N coefficients $\{a_j\}$ such that the kernel functions, $G_j(t)$, can be shaped into an averaging function centered on t_0. That is, we want to find $\{a_j\}$ so that the averaging function

$$A(t,t_0) = \sum_j a_j(t_0)G_j(t) \qquad (4.20)$$

is, in some sense, like a Dirac delta function centered on t_0. The variance of $\langle v^2(t_0)\rangle$ is

$$\epsilon^2(t_0) = \sum_{j=1}^{N} a_j^2 \sigma_j^2 \qquad (4.21)$$

where σ_j is the standard deviation of each datum e_j. The quadratic form to be minimized to obtain the optimal $\{a_j\}$ is

$$\phi(t_0) = \cos\theta \cdot \int_0^{t_m} (A(t,t_0 - \delta(t-t_0)^2\, dt + \sin\theta \cdot \sum_j a_j^2\sigma_j^2 + \lambda(1 - \int_0^{t_m} A(t,t_0)dt) \qquad (4.22)$$

In equation (4.22), θ $(0 \le \theta \le \pi/2)$ is the tradeoff parameter used to sacrifice resolution in $\langle v^2(t_0)\rangle$ for gain in statistical accuracy, and λ is a Lagrange multiplier for the unimodular constraint. Estimates of $\langle v^2(t_0)\rangle$ and its standard error $\epsilon(t_0)$ are available for any value of θ. In practical applications

where the data are inaccurate, the value of θ should always be greater than zero; that is, some resolution should always be sacrificed.

We shall restrict our attention to the inaccurate data given in Table 4-1. The tradeoff diagram for those data are shown in Fig. 4-5. The loss of resolving power with increasing record time is clearly displayed. In fact, for $t<0.5$ averages having standard deviation less than 0.5 km/sec and having resolution widths equal to the difference between two adjacent RMS times are available. This corresponds to the greatest resolving power possible. For $t \geq 1.5$ and $\epsilon \leq 0.5$, the best resolution is 0.45 seconds even though adjacent RMS times are .12 seconds. In Fig. 4-6a we have plotted tradeoff curves for $t_0=0.55$ seconds and $t_0=1.25$ seconds. Selected averaging functions are shown in Figs. 4-6b and 6c. Those in Fig. 4-6b correspond to $\theta=0$ and those in Fig. 4-6c each have a width of 0.45 seconds. This serves to illustrate how the averaging functions spread out as resolution is sacrificed in order to gain statistical reliability.

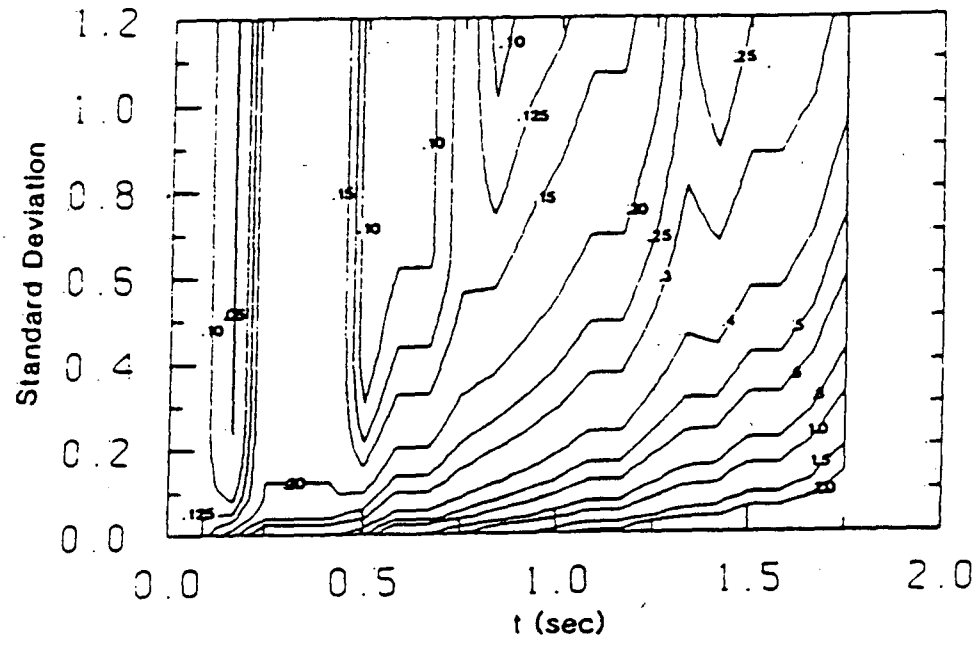

Figure 4-5

Trade-off diagram for RMS velocity inversion. The standard deviation of the average value is plotted as the ordinate. Contour values are in seconds and they represent a width of the averaging function evaluated by computing $1.0/A(t_o,t_o)$. No widths exist for t_o > 1.78 seconds since this exceeds the maximum time for an RMS datum. Consequently, all of the kernel functions are zero beyond t=1.78 and so is the averaging function.

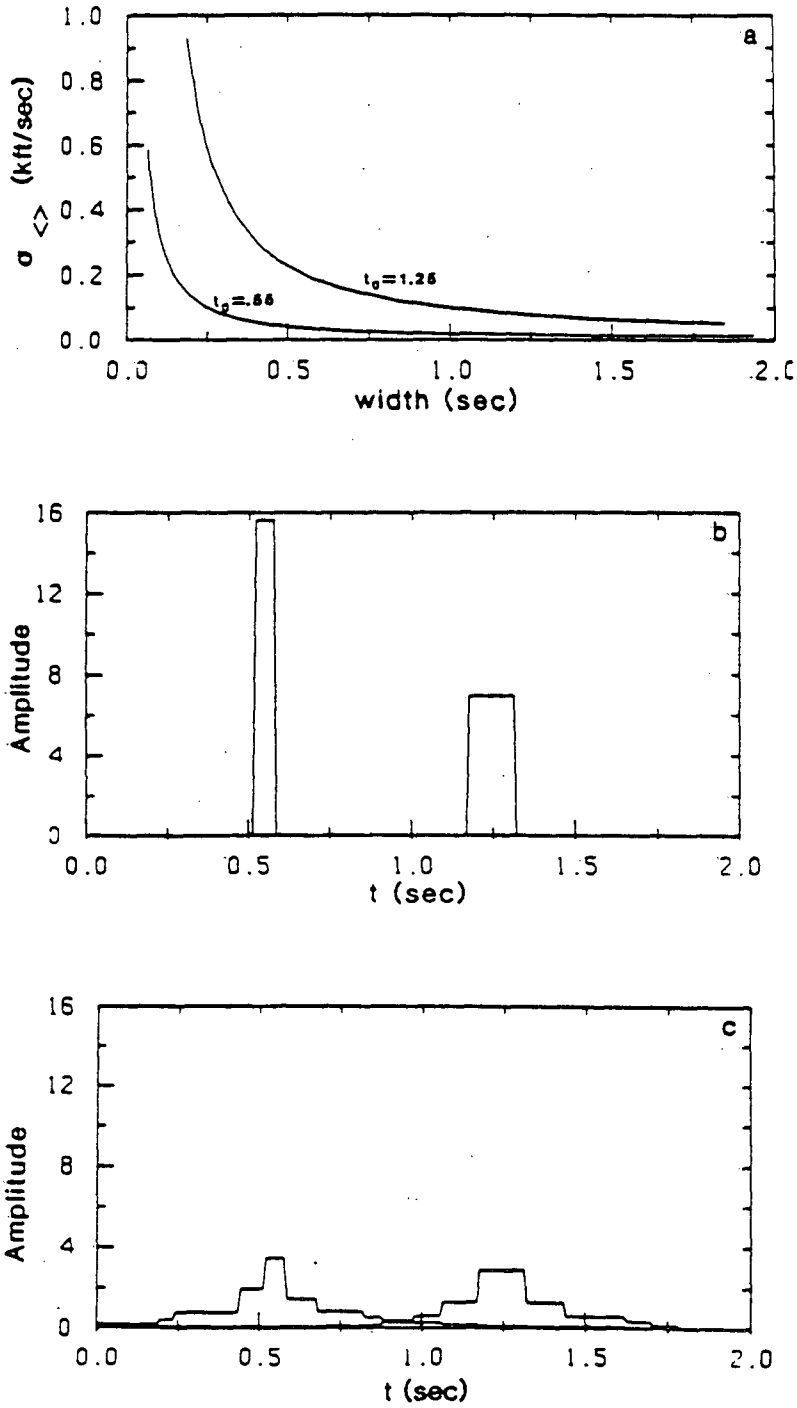

Figure 4-6

Trade-off curves for t_0=0.55 seconds and t_0=1.25 seconds are shown in (a). Maximum resolution averaging functions for these two times are shown in (b). Averaging functions which have a width of 0.45 seconds are shown in (c).

4.4 : DERIVATION OF THE IMPEDANCE CONSTRAINTS

The LP or AR broadband reflectivity construction algorithms can incorporate constraints of the form

$$\sum_{i=1}^{n} \beta_{ik} r_i = \gamma_k \pm \delta\gamma_k \qquad (4.23)$$

where r_i are the unknown reflectivity coefficients in a time window (t_1,t_2), β_{ik} are a set of constants for the k'th constraint, γ_k is the constraint value, and $\delta\gamma_k$ is an estimated error.

Our goal is to use the RMS velocities $V(t_j)$, $j=1,...N$ and their estimated errors to find constraints in the form of equation (4.23). We shall accomplish this by first choosing a time t_0 in the interval (t_1,t_2) and then computing the Backus-Gilbert localized averages

$$\langle v^2(t_0)\rangle = \int_0^{t_m} v^2(t)A(t,t_0)dt \qquad (4.24)$$

Equation (4.24) will then be manipulated so that it has the form of equation (4.23). The desired set of constraints to be input into the construction algorithms is obtained by carrying this procedure out for a number of times t_0 within the interval (t_1,t_2).

We begin with the linearized form of the acoustic impedance,

$$\xi(t) = \xi(0)\ \exp[2\cdot\int_0^t r(u)du] \tag{4.25}$$

and define

$$\eta(t) = \ln\{\xi(t)/\xi(0)\} = 2\cdot\int_0^t r(u)\ du \tag{4.26}$$

In order to proceed further, we need to determine the relationship between velocity and impedance. This specification depends upon the assumptions made concerning the density and usually one of two choices is selected. Either the density variations are assumed to be unimportant, in which case $\xi(t)$ is set equal to $v(t)$ and hence

$$v(t) = v(0)\cdot\exp[\eta(t)] \tag{4.27}$$

or the density is assumed to depend upon a power of the velocity. That is,

$$\rho(t) = C\cdot v^{\alpha}(t) \tag{4.28}$$

where C is a constant. The value of α is often chosen to be near 0.25. If equation (4.28) is assumed then

$$v(t) = v(0)\ \exp[p\eta(t)]$$

(4.29)

where $p=1/(1+a)$. Clearly (4.27) is a special form of (4.29) and so we shall keep the generality afforded by the power law representation and let $p=1$ when density variations are to be neglected.

By squaring equation (4.29), and substituting into (4.24) we get

$$\langle v^2(t_0)\rangle = \int_0^{t_m} v^2(0)\, \exp[2p\eta(t)]\, A(t,t_0)dt \pm \delta_{\langle\rangle} \tag{4.30}$$

where $\delta_{\langle\rangle}$ is the error in $\langle v^2(t_0)\rangle$ arising from observational uncertainties. After expanding the exponential and using the unimodularity of the averaging function this may be written as

$$\int_0^{t_m} \eta(t)\cdot A(t,t_0)\cdot dt = 1/2p\{ \langle v^2(t_0)\rangle/v^2(0) - 1 - \sum_{k=2}^{\infty} (2p)^k/k! \int_0^{t_m} \eta^k(t)\, A(t,t_0)\, dt\} \pm \delta_{\langle\rangle}/2pv^2(0) \tag{4.31}$$

The intergral on the left can be written as

$$\int_0^{t_m} \eta(t)\cdot A(t,t_0)\cdot dt = I_1 + \int_{t_1}^{t_2} \eta(t)\cdot A(t,t_0)\cdot dt + I_2 \tag{4.32}$$

where

$$I_1 = \int_0^{t_1} \eta(t) \cdot A(t,t_0)\ dt$$

and

$$I_2 = \int_{t_2}^{t_m} \eta(t) \cdot A(t,t_0) \cdot dt$$

By substituting equation (4.26) into (4.32) and interchanging the order of integration we get

$$\int_0^{t_m} \eta(t) \cdot A(t,t_0)\ dt = I_1 + I_2 + I_3 + 2 \cdot \int_{t_1}^{t_2} r(u) \cdot \underline{\beta}(u,t_0)\ du \qquad (4.33)$$

where

$$I_3 = \eta(t_1) \cdot \int_{t_1}^{t_2} A(t,t_0) \cdot dt$$

and

$$\underline{\beta}(u,t_0) = \int_u^{t_2} A(t,t_0) \cdot dt$$

Equation (4.33) can now be written as

$$\int_{t_1}^{t_2} r(u) \cdot \underline{\beta}(u,t_0)\ du = -1/2\ \{I_1 + I_2 + I_3\} + 1/4p\ \{\langle v^2(t_0)\rangle / v^2(0) - 1 - \sum_{k=2}^{\infty} (2p)^k L_k\} \pm \delta_{\langle\rangle} / 4pv^2(0) \qquad (4.34)$$

where

$$L = 1/k! \int_0^{t_m} \eta^k(t)\, A(t,t_0)\, dt \qquad (4.35)$$

A discretized version of the integral on the left hand side of equation (4.34) is of the form required for the constraint. The only difficulty that remains is to evaluate the right hand side of that equation. There are some special circumstances in which this evaluation is easily carried out. If the averaging function is confined to the region (t_1,t_2), and if $\eta(t)$ is small enough so that terms L_k can be neglected for k>2, then the right hand side of equation (4.34) reduces to

$$-(1/2p)\ \eta(t_1) + 1/4p\ \{\langle v^2(t_1)\rangle/v^2(0) - 1\ \} \pm \delta_{<,}/4p\ v^2(0) \qquad (4.36)$$

This quantity is determined if the impedance at t_1 is known. Unfortunately, these conditions rarely occur in practice. Usually, the averaging function cannot be completely confined to the region (t_1,t_2). Also, the impedance is often observed to vary by a factor of 2 or more in realistic data sections. This means that η is greater than ln 2, and hence the power series representation requires more than just the linear term; that is, the integrals L_k cannot be neglected.

The basic difficulty then is that an evaluation of the right hand side of equation (4.34) requires knowledge of $\eta(t)$, or equivalently the model for which we are attempting to solve. Our choices are to reformulate the problem and solve the fully

nonlinear problem or to attempt to find a good estimate of the right hand side through some other means. We shall adopt the latter choice and accomplish our objective by using the RMS velocities and interval velocity constraints to construct a best estimate, $v_c(t)$, of the true earth velocity v(t). The previous section of this paper showed that the constructed models can reasonably be expected to emulate the broad scale features of v(t) but will exhibit few, if any, of the rapid changes of velocity that are so important to the final geological interpretation. Nevertheless, such a $v_c(t)$ will suffice here since the constraints in (4.34) involve only integrals of $\eta(t)$.

In the following examples we have elected to use the flattest model with a weighting function of unity. As a type example, we shall invert the bandlimited seismogram in Fig. 4-1 and attempt to recover the velocity structure in the time window (0.4,1.4) seconds. The results of applying an unconstrained LP algorithm to the seismogram within the window of interest are shown in Fig 4-7a. The failure of the construction is dramatically illustrated by superposing the true velocity on the LP solution. It should be pointed out that this example was contrived to make the LP solution fail; nevertheless, the chosen velocity structure does not seem unrealistic and we can appreciate that similar failures of the LP or AR algorithms may occur in practice.

Information from the seventeen accurate RMS velocities in Table 4-1 was added in the following manner. First we generated high resolution averaging functions (θ=0) and obtained the

corresponding values of $\langle v^2(t_o)\rangle$ at twelve equally spaced values of t_o in the inverval (0.4, 1.4). The flattest model (Fig. 4-2a) was constructed, and the constraints of equation (4.34) were calculated. The LP solution was computed and the velocity was recovered by using the standard recursion formula. That velocity is shown in Fig 4-7b. The excellent agreement with the true velocity illustrates the importance of including information from RMS velocities. The correspondence between the interval velocity recovered from the LP construction and the flattest model from which constraints were generated is shown in Fig. 4-7c.

We have shown how an appraisal analysis which generates linear averages of $\langle v^2(t)\rangle$ can be used to provide constraints for the construction algorithms. This average has the form of equation (4.19) and it is unique in that any model $v^2(t)$ which reproduces the RMS data will have the same average when its inner product is taken with the averaging function A(t). There is, however, another possiblity for computing an average. Equation (4.10) can be written as

$$e_j = \int R_j(t)\cdot v(t)\, dt \qquad j=1,\ldots N \tag{4.37}$$

where $R_j(t)=G_j(t)\cdot v_c(t)$ are modified kernel functions and $v_c(t)$ is a constructed velocity function. Using equation (4.37), it is possible to obtain Backus-Gilbert averages of the velocity rather than velocity squared. That is,

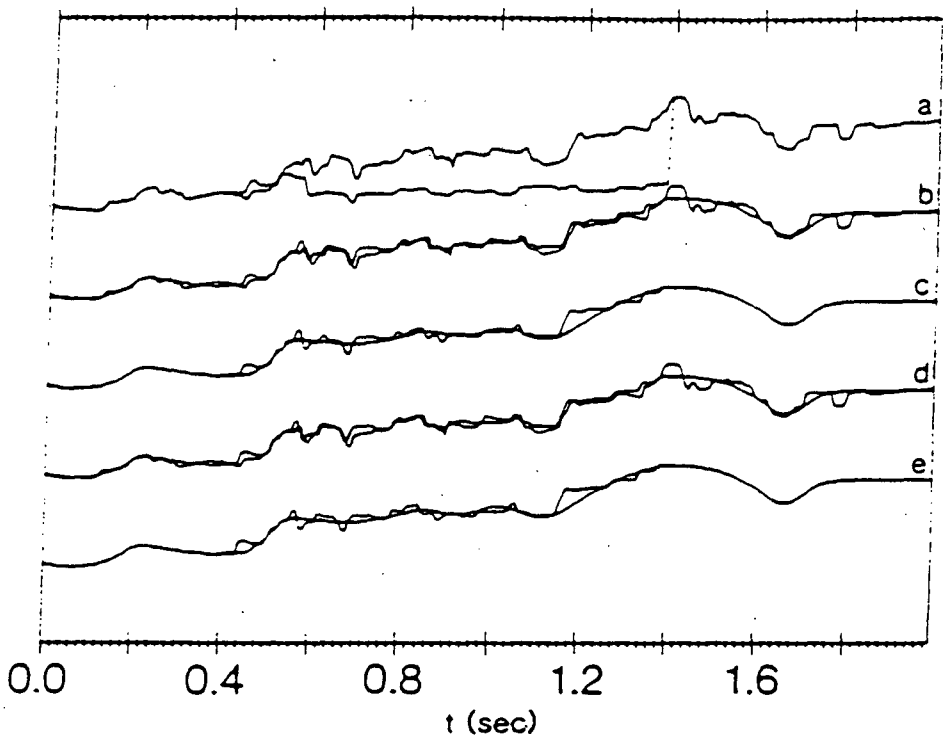

Figure 4-7

The true velocity structure, and the recovered interval velocity when no RMS constraints were used, are shown in (a). The inversion was carried out only on the time window (0.4-1.4) seconds. Shown in (b) is the recovered interval velocity when RMS constraints using averages $\langle v^2(t_0)\rangle$ were incorporated into the inversion. The recovered velocity in the time window (0.4-1.4) seconds is inserted into the flattest model obtained by inverting the RMS data alone. The entire profile (0.0-2.0) seconds is then superposed upon the true velocity structure. The correspondence between the flattest model and the LP reconstruction is shown in (c) where these two functions have been superposed. The results in (d) and (e) are analagous to those in (b) and (c) except that averages $\langle v(t_0)\rangle$ were used to generate constraints for the linear programming algorithm.

$$\langle v(t_0)\rangle = \int_0^{t_m} v(t)\cdot A(t,t_0)\cdot dt \qquad (4.38)$$

where the averaging function A(t) is now a linear combination of the kernels $R_j(t)$. The interpretation of the uniqueness of $\langle v(t_0)\rangle$ is that all models which are linearly close to $v_c(t)$ will have the same average $\langle v(t_0)\rangle$. If $v_c(t)$ is a good estimate for the gross earth velocity, this additional restriction should prove beneficial.

Manipulating (4.38) in the same manner as used to generate equation (4.34) produces

$$\int_{t_1}^{t_2} r(u)\cdot \underline{\beta}(u,t_0)\cdot du = -1/2\ \{I_1 + I_2 + I_3\} + 1/2p\ \{\langle v(t_0)\rangle/v(0) - 1 + \sum_{k=2}^{\infty} p^k L_k\} \pm \delta_{\langle\rangle}/2pv^2(0) \qquad (4.39)$$

where $\delta_{\langle\rangle}$ is the error of $\langle v(t_0)\rangle$. Again, the discretized form of the left hand side yields the desired constraint. A comparison of equation (4.39) with (4.34) illustrates another advantage of the nonlinear form of the Backus-Gilbert averages. The integrals L_k in the infinite summation in (4.39) are no longer premultiplied by 2 as they were in equation (4.34). Thus fewer terms need be taken, and computations are thereby reduced.

The results of using constraints based upon averages $\langle v(t)\rangle$ are shown in Fig. 4-7d. The reconstructed velocity has been superposed upon the true velocity and agreement between the two

functions is good. We also note that for this example there appears to be little difference in the results from using $\langle v(t) \rangle$ rather than $\langle v^2(t) \rangle$. We do not know whether this is a general statement but it appears to be so in the examples that we have done. Because of the advantages already stated, the remainder of the paper will use only averages $\langle v(t) \rangle$ to generate the constraints.

The example in Fig. 4-7 shows that high quality constraints can be generated from RMS velocities which are accurate. Yet such precise data are never available in practice and it is important to investigate the effects of data inaccuracies. Realistic constraints must be written as

$$\gamma_j - \delta\gamma_j \leq \sum_i \beta_{ij} r_i \leq \gamma_j + \delta\gamma_j \qquad (4.40)$$

where $\delta\gamma_j$ is an error estimate for γ_j. An examination of (4.39) shows that observational errors increase $\delta\gamma_j$ in two ways. First, the averages $\langle v(t_0) \rangle$ (or $\langle v^2(t_0) \rangle$) are inaccurate because of statistical errors in the data. The standard deviation of $\langle v(t_0) \rangle$ is given by equation (4.21) and this must be incorporated as an error in the right hand side of (4.39). Secondly, the evaluation of the integrals I_1, I_2 or L_k requires that a good representation of the low frequency components of $v(t)$ be present in the constructed velocity $v_c(t)$. Yet from Section 4.2, it is expected that similarities between $v_c(t)$ and $v(t)$ will be degraded as the errors increase. The errors in evaluating the integrals, incurred by using $v_c(t)$ rather than

the true $v(t)$, should also be included in the $\delta\gamma_j$ in equation (4.40). For the work done here we shall assume that this contribution to the error can be ignored and we will concentrate upon the statistical errors arising from the Backus-Gilbert appraisal.

At each time t_0, many averages $\langle v(t_0)\rangle$, their standard deviations, $\epsilon(t_0)$, and their associated averaging functions, $A(t,t_0)$, are available. The question arises as to which average provides the most useful constraint. Choosing an average with a large standard deviation can make $\delta\gamma_j$ so large that the constraint becomes impotent. Alternatively forming averages which are very accurate may require the sacrifice of so much resolution that information contained in the RMS data has been needlessly lost.

It is doubtful that a strategy exists which will work optimally in all cases, but the following attack is reasonable. Of primary concern is the error on the constraint. To keep this sufficiently small we require that $\langle v(t_0)\rangle$ have a relative error no greater than α percent. If no average exists with this error, then the average having two times the minimum standard deviation ($\theta = \pi/2$) is selected. The results in Figs. 4-8b and 8c show the recovered interval velocities when α = 25% and 5%. They are not greatly different and hence the value of α does not appear to be too critical.

The recovered velocities in Figs. 4-8b and 8c are greatly improved over those in Fig. 4-7a where no RMS constraints were used, but as expected, the agreement between the true and

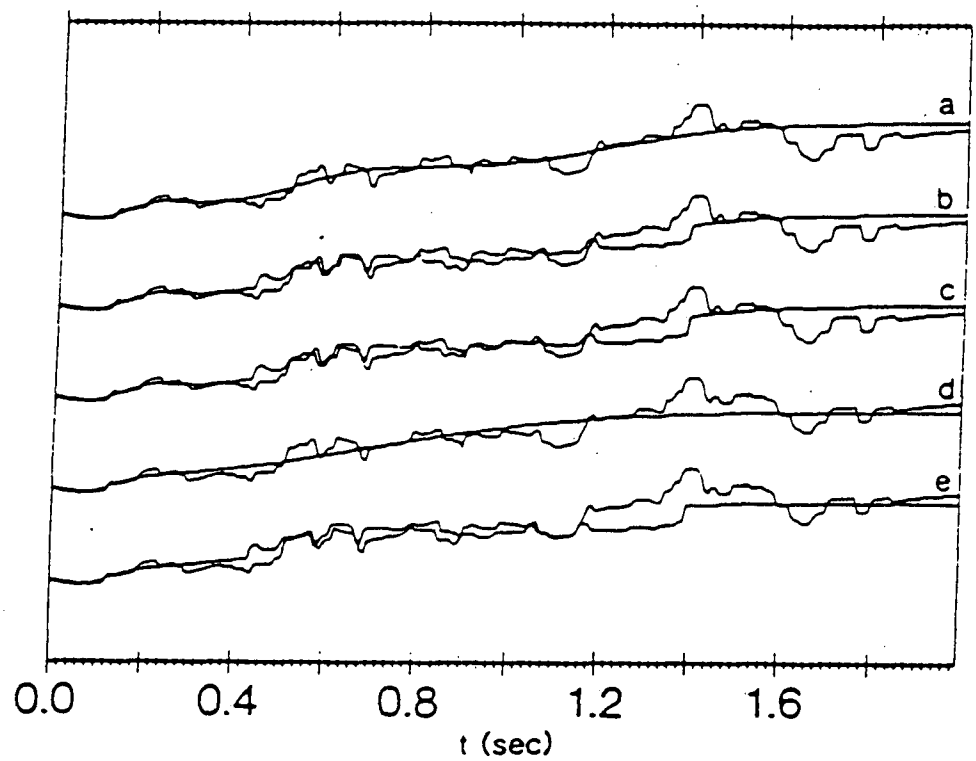

Figure 4-8

The flattest interval velocity model obtained by inverting the inaccurate RMS constraints in Table 4-1 is shown in (a). It is superposed upon the true velocity. Figures (b) - (c) respectively show the interval velocity recovered from the LP solution when averages $\langle v(t_0) \rangle$ have a relative error of α = 25% and 5%. Figure (d) shows the flattest model when the RMS errors in Table 4-1 are trebled. The LP construction, using these erroneous data and α=25%, is shown in (8e).

recovered velocities is not as good as when the data were accurate. To see how the degradation increases with increased errors on the RMS data we have redone the calculations after trebling the errors in Table 4-1. The results are shown in Figs. 4-8d and 8e. They are somewhat disappointing; major discrepancies between the true and reconstructed velocities are apparent, particularly in the interval 1.0 - 1.4 seconds.

It appears that the strategy outlined so far can work well when the data are reasonably accurate. However, the usefulness of the RMS data diminishes rapidly if the errors become too large. When large errors are to be contended with, it is best to alter slightly the above approach. We propose the following steps.

We first construct a best estimate for the interval velocity by inverting RMS velocities along with point velocity constraints if they are available. Next we form a high resolution averaging function for an arbitrary time t_o in the same manner as before. However, instead of using $\langle v(t_o)\rangle$ calculated from equation (4.38), we compute

$$\langle v\ (t_o)\rangle = \int_o^{t_m} v_c(t)\ A(t,t_o)\ dt$$

where $v_c(t)$ is the constructed interval velocity model. In addition, we assign a relative error of ν percent to $\langle v_c(t)\rangle$ where ν depends upon how closely we wish the final constructed model to look like $v_c(t)$. In effect, this approach forces the final velocity obtained from the LP solution to look like the

constructed model.

It must be understood that the results obtained from this method are less certain than those obtained from the initial strategy. There will be other models which satisfy the RMS velocities and the reflection seismogram constraints, but we are restricting our best guess to be that one which looks most like $v_c(t)$. This means that if $v_c(t)$ is a good approximation to $v(t)$, our final velocity structure should be close to the true earth velocity, but if $v_c(t)$ is greatly wrong, then our results will be in error.

In Fig. 4-9 we show the results of using averages $\langle v_c(t) \rangle$ to develop the LP constraints. The LP velocity recovered after assigning an error of ν = 5% is shown in Fig. 4-9b. The result is considerably better than that shown in Fig. 4-8e which began with the same erroneous RMS data.

It is obvious that the current strategy will work better as $v_c(t)$ becomes closer to the true $v(t)$. Improved results should therefore be expected if point velocity constraints are included in the inversion. The degree of improvement is shown in Figs. 4-9c and 9d where six interval velocity constraints (see Table 4-1 for locations and values) were included in the construction of $v_c(t)$. The agreement between the true and recovered interval velocities in Fig. 4-9d is excellent.

It is perhaps too much to expect that six velocity constraints might be known. More commonly, only the velocity at a large reflector (perhaps coinciding with a major unconformity) might be available. With this in mind the analysis was redone

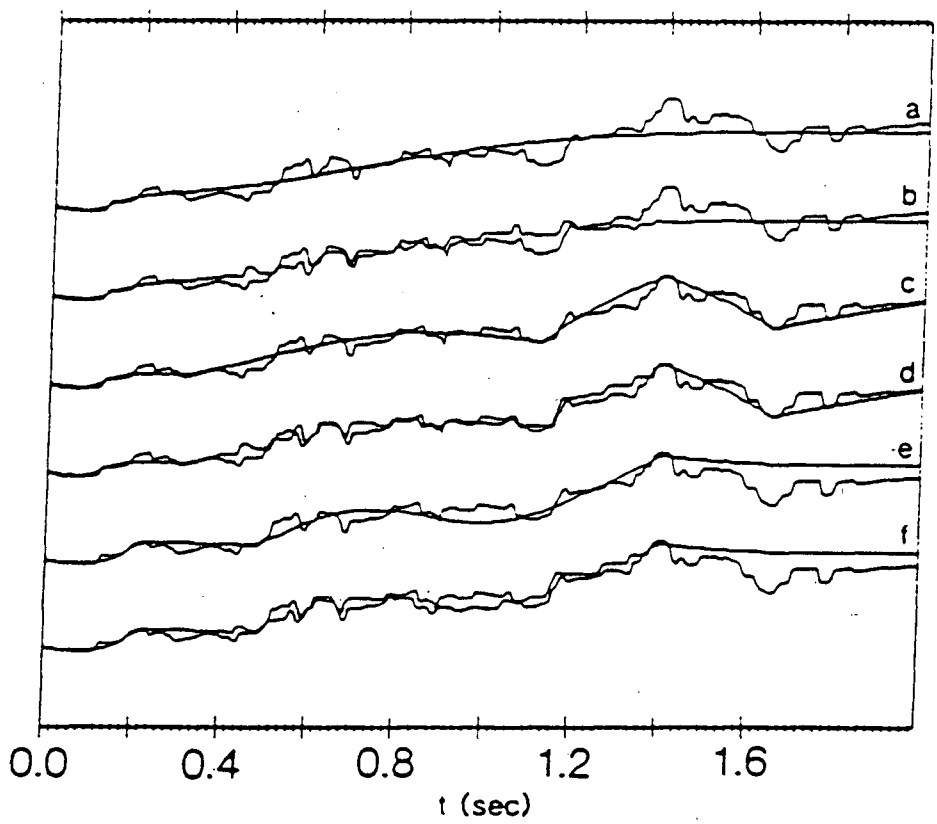

Figure 4-9

The flattest model obtained by inverting the inaccurate RMS data in Table 1 is shown in (a). That velocity is used to form averages <v(t)> which are arbitrarily assigned an error of ν=5% and then used as constraints in the LP solution. The results are shown in (b). The effects of adding six inaccurate point velocity constraints into the construction of the interval velocity is shown in (c) and (d). The flattest model interval velocity has been reproduced in (c) and the velocity recovered from the LP construction is shown in (d). Figures (e) and (f) are the same as (c) and (d) except that only one velocity constraint (at t=1.4 seconds) has been used in the interval velocity construction.

after using only the single velocity constraint at $1.\bar{4}$ seconds. The constructed velocity $v_c(t)$ is shown in Fig. 4-9e and the interval velocity obtained from the LP algorithm is shown in Fig. 4-9f. The agreement between the two velocities is very good.

4.5 SUMMARY

The primary goal of this chapter has been to incorporate information from stacking velocities directly into the LP or AR construction algorithms. To accomplish this we considered two separate inverse problems. In the first problem, RMS velocities as well as point velocity constraints were inverted to find a low frequency interval velocity. Our philosophy has been to construct only velocities having a minimum of structure and we have achieved this goal by minimizing the gradient of the squared velocity in a 1-norm or 2-norm sense. Some flexibility has been introduced by including a weighting factor in the norm to be minimized. The rationale for the weighting was that stacking velocities are obtained only at those times corresponding to significant reflections and hence the constructed model should be allowed to have large gradients at those times. Both the L_1-norm flattest model, and the L_2-norm flattest model with a Gaussian weighting, will generate models of this type. It is difficult to say which norm and which

weighting will produce the best results. Most likely there are data sets and particular geologic environments in which either algorithm will be superior to the other. For the work carried out here we have used only the L_2-norm flattest model without any weighting and have found it to perform satisfactorily.

The important improvement of our construction algorithms over the Dix formula is one of stability. The Dix formula is a discretized version of the analytic inverse, and is inherently unstable. Oscillations in the recovered velocity will always appear when the data are inaccurate because of the need to find the time derivative of the RMS velocity. Alternatively, the algorithms presented here fit the observations only to within a degree justified by their error. Consequently, small scale structural detail that may be an artifact of the noise is generally not included in our models. Also our methods admit the direct incorporation of point velocity constraints into the inversion. This has no counterpart in the Dix formula.

In the second inverse problem, we use the RMS velocities to extract unique information about the average value of the velocity or its square. The expression for these averages is manipulated into a form that can be handled by the LP and AR algorithms.

The methods developed in the paper seem to work well when the RMS velocities are reasonably accurate. However, if the observational uncertainties become too large, the error in the constraint value may increase to the point where the constraint is ineffective. Attempts to reduce the errors by increasing the

width of the averaging function may not be productive if too much resolution must be lost to achieve the desired accuracy. In such circumstances an alternate strategy must be developed. We have proposed that the constraints supplied to the LP or AR algorithms be generated using high resolution averaging functions. However, the large calculated uncertainties in the associated constraint values should be ignored, and new artificially small errors assigned. By doing this we are presuming that the calculated smooth version of the interval velocity is 'closer' to the true velocity than the errors and the nonuniqueness would technically indicate.

In addition to the RMS data, any available bounds on velocities at specific times should be incorporated into the inversion. The norm to be minimized and the weighting function should be chosen by their ability to produce the right 'type' of velocity function for the particular geological environment. When an entire section is to be inverted it may be advisable to invert stacking velocities from many traces across the section, smooth the output, and use these results as a best guess for the low frequency velocity structure. The recovery of the acoustic impedance may then continue after forming averages of the interval velocity over reasonable resolution widths. These averages can be assigned errors in accordance with the confidence that the interpreter has in his constructed low frequency velocity. The computations to obtain the numerical value of the constraint and the appropriate linear combination of the reflection coefficients can proceed exactly as before.

The LP or AR algorithms can then be used to construct a best estimate of the full band reflectivity and substitution of those results into the standard recursion formula produces a best estimate of the impedance.

It is now seen that the recovery of the acoustic impedance from the band limited seismograms involves four linear inverse problems. The first is appraisal deconvolution to determine unique averages of the reflectivity function. The inclusion of information from stacking velocities requires the construction of a low frequency interval velocity which is consistent with estimated RMS velocities and point velocity constraints, and it also requires a Backus-Gilbert appraisal to obtain unique averages of the velocity. The Fourier transform of the averages of the reflectivity function, the constraints from the RMS velocities, and any additional impedance constraints are then used in a final construction algorithm to produce an acoustic impedance which is consistent with all available geological and geophysical information.

CHAPTER V: MULTI-TRACE SIMPLEX ALGORITHM IN SEISMIC DATA ANALYSIS

5.1 INTRODUCTION

Advantages associated with the use of linear programming in the solution of certain geophysical problems have been pointed out in a number of recent publications. Applications of the method to signal analysis, wavelet deconvolution, amplitude spectrum estimation, and acoustic impedance inversion have been described in Claerbout and Muir (1973), Taylor et al. (1979), Levy and Fullagar (1981), Deeming and Taylor (1981), Oldenburg et al. (1983), Levy et al. (1982), and Oldenburg et al. (1984). However, despite its utility and robust performance when applied to these problems, the method is still not widely used. To a large degree this is probably attributable to the large computational effort usually required in the solution of linear programming problems.

Attempts to increase the efficiency of linear programming are described in Deeming and Taylor (1981) and Oldenburg et al. (1983). The former elected to use the conjugate sub-gradients method, which is shown to have computational advantages over the standard Simplex method when the problem solved exceeds a certain size. The latter introduced 'polarity constraints' and objective function weighting to both reduce the size of the problem, and to force a shorter solution search. Although the

computational effort was decreased significantly, the preimposed conditions on the solution could result in distortion or bias in certain cases, such as for small amplitude events in near proximity to large amplitude reflections.

We present here an alternative approach based on certain manipulations of the Simplex method, which when applied to seismic sections exhibiting a reasonable trace-to-trace correlation, will result in significantly shorter processing time.

5.2 SIMPLEX ALGORITHM (BACKGROUND)

In the begining of this section we give an intuitive description of the Simplex algorithm. A short mathematical presentation will follow. As the reader will note, our description includes only the information we feel is necessary for the understanding of the proposed manipulations; for more details the reader is referred to Gass (1964), and Claerbout and Muir (1973).

A general linear programming problem is of the form:

$$\text{minimize (or maximize) } \bar{c}^T \cdot \bar{x}$$

subject to:

$$A \cdot \bar{x} \geq \bar{b}$$

$$(\text{ or } A \cdot \bar{x} \leq \bar{b})$$

and

$$I \cdot \bar{x} \geq \bar{0}$$

where $\bar{c}$ is an (Nx1) vector of objective function coefficients,

$\bar{x}$ is an (Nx1) vector of unknowns,

$\bar{b}$ is the (Mx1) vector containing the RHS,

A is the (MxN) matrix of constraints,

I is the (NxN) identity matrix,

$\bar{0}$ is an (Nx1) vector whose elements are zeros,

and M and N, are the number of constraints and variables, respectively.

We will use a simple two variable example to define and describe certain necessary terms by geometrical means. Consider the problem;

$$\text{maximize } c_1x_1 + c_2x_2$$

subject to:

$$a_{11}x_1 + a_{12}x_2 \leq b_1$$

$$a_{21}x_1 + a_{22}x_2 \leq b_2$$

$$x_1 \geq 0$$

$$x_2 \geq 0$$

Geometrically this problem is expressed as:

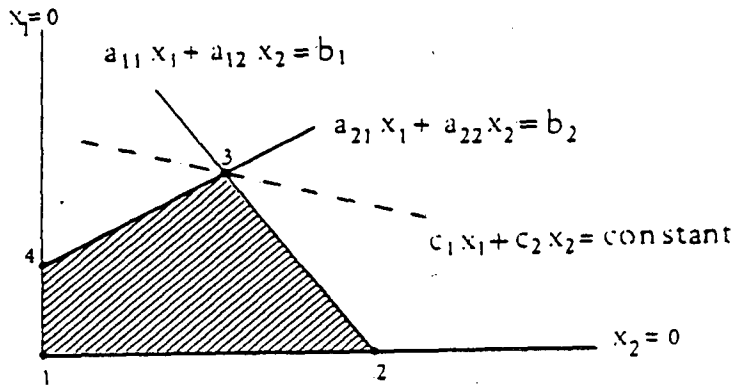

FIGURE 5.1

TERMINOLOGY

(a) The hatched area is called the solution solid; all possible solutions to the problem are contained in this space. (note, in 2-space this is an area, in 3-space this is a volume, etc.)

(b) The solution solid is bounded by N+M constraint equations; $A \cdot \bar{x} = \bar{b}$, and $I \cdot \bar{x} = \bar{0}$. (note, in 2-space these are lines, in 3-space they are planes, etc.) The points where N of these equations intersect are called 'extreme feasible points'. It is easy to see that each of these intersections defines a vector with at most M non-zero elements. In Figure 5-1, the extreme feasible points are marked by the numbers 1, 2, 3, and 4.

(c) The objective function is represented by the family of lines $c_1x_1 + c_2x_2 =$ constant. This function specifies a unique solution to the problem provided it is not 'parallel' to any of the constraints.

A basic theorem of linear programming states that the optimal solution to a linear programming problem is an extreme feasible point (Gass, 1964, pg.46-53) (i.e. in Figure 5-1 the solution will be one of the points 1, 2, 3, or 4). The Simplex algorithm is based on this theorem. The algorithm starts by finding an extreme feasible point (usually $x_j=0$, $j=1..N$, for example, point 1 in Figure 5-1 above), and then hops from one extreme feasible point to another in a way that will ensure a continuous improvement in the value of the objective function.

When no further improvement is possible, the current extreme feasible point is the desired optimal solution.

Since the number of extreme feasible points searched in the process of finding the solution determines the run time and execution cost, we wish to minimize this number. To achieve this goal one may take any of the following routes:

(a) using a gradient method (Claerbout and Muir, 1973), one may seek at each step the direction of search which will yield the best possible improvement in the objective function. Thus the number of steps necessary to achieve the desired extremum is hopefully decreased. Unfortunately, there is no guarantee that the total number of steps will be decreased, and in any event the amount of calculation required at each step of the gradient method is large enough to add doubt to the profitability of this operation.

(b) Assume that some 'a priori' knowledge of the sought solution is given. It is then possible to reduce the number of Simplex steps required in the solution of a linear programming problem using the following options:

(1) modifying the desired objective function in such a way that the Simplex algorithm will choose a 'short' path toward the solution. In the deconvolution problem this modification involves the assumption that the processed seismic trace contains information concerning reflector positions and relative amplitudes which is approximately true for at least the major reflections. This type of modification is described in detail in

Oldenburg et al. (1983), and Scheuer (1981).

(2) starting the Simplex search at an extreme feasible point which is 'close' to the sought solution. For example, consider the problem outlined in Figure 5-1. Assume that the solution we seek is extreme feasible point (3). A Simplex search starting either at point (2), or (4), will reach the solution in a smaller number of steps than a search initialized at (1). In the processing of stacked seismic sections we generally do not expect the reflectivities to change drastically across adjacent traces; that is, we expect the solution of the ith trace to define an extreme feasible point which is 'close' to the solution of the ith+1 trace. By starting the Simplex search at this point we will avoid the cost associated with the operations necessary to move from an arbitrary starting point to the 'vicinity' of the solution.

The meaning of the terms 'close' and 'vicinity' in the context of this work can be understood through the example shown in Figure 2 below:

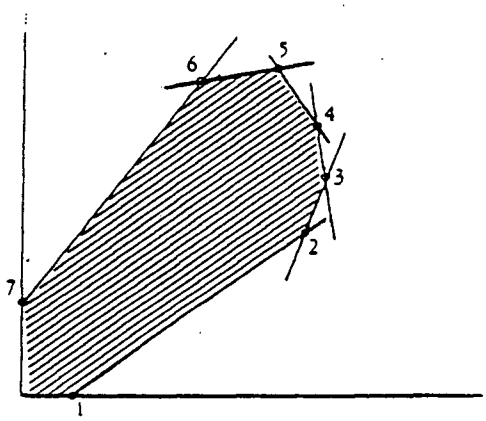

FIGURE 5.2

In this figure, 'extreme feasible point' (7) is algorithmically closer to 'extreme feasible point (5) than is point (2), although point (2) is closer to (5) in a Euclidian sense. Keeping this in mind, we use the term 'closer' in the rest of this work as meaning Euclidian closer, but with the hope that it also translates into meaning algorithmically closer.

5.3 BASIC FORMULATION OF THE ALGORITHM

Consider the problem;

$$\text{minimize } H(x) = \bar{c}^T \cdot \bar{x}, \quad \text{subject to}$$

$$x_i \geq 0 \quad , \qquad A \cdot \bar{x} \geq \bar{b} \quad , \qquad (i=1...N)$$

where A is an (MxN) matrix. We can convert the inequalities into equalities by introducing slack variables y_i ($y_i \geq 0$, i=1...M).

$$\begin{bmatrix} & | & \\ A & | & I \\ & | & \end{bmatrix} \begin{bmatrix} \bar{x} \\ - \\ \bar{y} \end{bmatrix} = V\,\bar{x}' = \bar{b}$$

where V is an (M x N+M) matrix. Denoting the jth column of V by $\bar{v}_j$ we have

$$\sum_{j=1}^{N+M} x'_j \cdot \bar{v}_j = \bar{b}$$

Now, assume that we already know an extreme feasible point, for example, x'^0 :

$$x'^0_i = x_i \qquad i=1...M,$$

$$= 0 \qquad i>M$$

(Recall that an extreme feasible point is characterized by at most M non-zero variables). We then write:

$$\sum_{i=1}^{M} x_i'^{0} \cdot \bar{v}_i = \bar{b} \qquad (5.1)$$

The corresponding value of the objective function is:

$$H_1 = \sum_{i=1}^{M} x_i'^{0} \cdot c_i \qquad (5.2)$$

Assuming that the vectors $\bar{v}_i$, i =1..M are linearly independent, they form a basis of the M space. If the MxM matrix B is constructed using $\bar{v}_i$, i=1...M as its columns then we may write:

$$\bar{v}_j = \sum_{i=1}^{M} s_{ij} \cdot \bar{v}_i \quad \text{for} \quad j=1....N+M. \qquad (5.3)$$

$$\text{where} \quad S = B^{-1} \cdot V$$

Define

$$h_j = \sum_{i=1}^{M} s_{ij} \cdot c_i - c_j \qquad (5.4)$$

We now wish to establish whether replacing any of the variables corresponding to the current basis with some other variable, for example, x_k', will yield farther reduction in the objective function value. Subtracting 'p' times equation (5.3) from equation (5.1), with j=k, we obtain:

$$\sum_{i=1}^{M} (x_i'^{0} - p\, s_{ik}) \cdot \bar{v}_i + p \cdot \bar{v}_k = \bar{b} \qquad (5.5)$$

where p is an arbitrary non-negative constant to be determined, and $M < k \leq N+M$. Our new solution is then $\bar{x}'^{1}$ (with potentially M+1 non-zero values):

$$x_i'^{1} = x_i'^{0} - p \cdot s_{ik} \quad , \quad i = 1....M$$

$$x_k'^{1} = p$$

The resulting value of the objective function would be:

$$H_2 = \sum_{i=1}^{M} (x_i'^{0} - p \cdot s_{ik}) \cdot c_i + p \cdot c_k = H_1 - p \cdot h_k \qquad (5.6)$$

By choosing $p = x_l'^{0} / s_{lk}$ $(1 \leq l \leq M)$, we set the value of the lth element of $\bar{x}'^{1}$ to zero, thereby introducing $x_k'^{1}$ into the set of active variables and excluding $x_l'^{1}$ from this set. The new values of the basis variables will be:

$$x'^{1}_{i} = x'^{0}_{i} - x'^{0}_{l}\, s_{ik}/s_{il} \qquad i \neq l \qquad (5.7)$$

$$x'^{1}_{i} = x'^{0}_{l}/s_{lk} \qquad i = l$$

To ensure the non-negativity of the current solution, the value of p must be:

$$p = \min_{i} \; (x'^{0}_{i} / s_{ik}); \quad \text{for all } i \text{ with } s_{ik} \geq 0 \qquad (5.8)$$

Since we wish H_2 to be smaller than H_1, the variable introduced into the basis must have its corresponding value of $h_k > 0$, as seen from equation (5.6). In general, this variable is associated with the largest h_j, although this does not necessarily ensure the best improvement in H, since the corresponding p may be small. Once the decision is made as to which variable leaves the basis, and which (x'^{1}_{k}) enters, the new set of variables is calculated via equation (5.7), and the h_j values necessary for the next decision using equation (5.4). This process can then be continued until the optimal solution is reached.

It is important to understand that in determining $\bar{x}'^{0}$ and $\bar{x}'^{1}$, we have actually solved M equations with M unknowns of the form ; $B^0 \cdot \bar{x}'^{0}_{t} = \bar{b}$, and $B^1 \cdot \bar{x}'^{1}_{t} = \bar{b}$, respectively. The vectors $\bar{x}'^{0}_{t}$ and $\bar{x}'^{1}_{t}$ are just truncated versions of the complete solutions $\bar{x}'^{0}$ and $\bar{x}'^{1}$ from which the zero elements have been excluded. The columns of B^0 and B^1 are the column vectors of V appropriate for the non-zero elements $\bar{x}'^{0}_{t}$ and $\bar{x}'^{1}_{t}$, respectively. At each ensuing iteration, the choice of the new basis determines a new B^i, and the values of $\bar{x}'^{i}_{t}$ (and thus $\bar{x}'^{i}$) can then be computed.

We call the attention of the reader to the fact that the vectors $\bar{x}'^{i}$ constitute extreme feasible points. Thus the

correspondence between the geometrical and algorithmic descriptions is clear.

Although each Simplex iteration necessitates a solution of the system $B \cdot \bar{x}_i = \bar{b}$, this solution does not take the full number of steps usually required. Standard Simplex routines find it computationally more expedient to store $B^{-1} \cdot A$, and $B^{-1} \cdot \bar{b}$, and update these at each iteration (Gass, 1964, pg.96-113). Because A contains B, $B^{-1} \cdot A$ will always contain the unit matrix I. As this needs not be stored in matrix form, it is possible to store B^{-1} in its place. We will use this information for the definition of a starting extreme feasible point in the next section.

5.4 SOLVING MULTIPLE RELATED PROBLEMS

Consider a set of problems of the form;

minimize $\Phi_i = \bar{c}_i^T \cdot \bar{x}_i$ subject to

$A_i \cdot \bar{x}_i = \bar{b}_i \quad , \quad x_{ij} \geq 0$ for all i and j ;

with the condition that $\bar{x}_{i+1}$ is 'close' to $\bar{x}_i$. A technique for an efficient solution to this type of a problem was proposed in Gass,1964, pg.143-144. The gist of it was that the starting extreme feasible point not be chosen arbitrarily, but rather is chosen using some a priori information about the solution form. In the following, we apply this technique (multi-trace Simplex) with some modifications.

We distinguish the following cases:

(a) A_i and $\bar{c}_i$ are invariant for all i.

(b) A_i and $\bar{b}_i$ are invariant for all i.

(c) A_i is invariant for all i.

(d) All of A_i, $\bar{b}_i$, and $\bar{c}_i$ change with i, but $\bar{x}_{i-1}$ is expected to be similar to $\bar{x}_i$.

Case (a)

Suppose that we have already solved the first problem; min $\bar{c}_1^T \cdot \bar{x}_1$, subject to $A_1 \cdot \bar{x}_1 = \bar{b}_1$, ; $x_{1j} \geq 0$, for all j, by the Simplex method. At this point we also possess the inverse basis B_1^{-1}. The vector $\tilde{x}_{2t} = B_1^{-1} \cdot \bar{b}_2$, when properly ordered in $\tilde{x}_2$, defines an extreme feasible point. We then use this point which hopefully is 'close' to the desired solution $\bar{x}_2$, to start the new Simplex search. When $\bar{x}_2$ is attained, we also have the new inverse basis B_2^{-1} which together with $\bar{b}_3$ defines the starting extreme feasible point $\tilde{x}_3$ to be used in the solution of the third problem. We continue in this fashion until the desired number of problems is solved.

Case (b)

In this case the solution $\bar{x}_1$ is already an extreme feasible point for the next problem. Utilizing equation (5.4) the values of h_j can be updated using $\bar{x}_1$ and $\bar{c}_2$, and the Simplex search is restarted. The process continues similarly for $\bar{x}_2$, etc. An alternative approach to the one outlined above is to work on the dual problem, (Gass 1964, pg.83-95) using the sequence of operations described in case (a).

Case (c)

Given the solution $\bar{x}_1$, B_1, and B_1^{-1}, we proceed as in case (a)

to find $\tilde{x}_2$ (an extreme feasible point pertaining to the second problem). Using $\tilde{x}_2$, and $\bar{c}_2$, we utilize equation (5.4) to update h_j, and proceed with the Simplex search starting at $\tilde{x}_2$. The process is repeated until the desired number of problems is solved.

Case (d)

In this case we use a combination of the cases outlined above. However, the crux of the approach is heavy objective function weighting used in a first pass on each problem.

Given the solution $\bar{x}_1$, we weight the objective function $\bar{c}_2$ in such a way that the non-zero elements in $\tilde{x}_2$ will be in nearly the same locations as those of $\bar{x}_1$. We then utilize equation (5.4) to update h_j with the desired objective function $\bar{c}_2$ (as outlined in case (b)), and restart the algorithm at extreme feasible point $\tilde{x}_2$. Once $\bar{x}_2$ is obtained we use it to weight the initial objective function for $\tilde{x}_3$, then proceed in this manner until the desired number of problems is solved.

5.5 APPLICATION TO SEISMIC DATA

Given a stacked section, our objective is to recover a spiky reflectivity section corresponding to the given data. The details of how a full-band reflectivity section is determined from the band-limited input section using linear programming

(LP) is described in chapters 2, 3 and 4 and in Levy and Fullagar (1981), Oldenburg et al. (1983), Scheuer (1981), and Oldenburg et al (1984). Consequently, we will give only the barest details.

The problem to be solved is of the form:

minimize $\bar{c}^T \cdot \bar{x}$, subject to,

$$A \cdot \bar{x} \geq \bar{b}, \text{ and } x_i \geq 0 \qquad \text{for all } i.$$

The matrix A may consist of three distinct blocks:

$$A = \begin{array}{|c|}\hline \text{IFT} \\ \hline \text{WLC} \\ \hline \text{RMS C} \\ \hline \end{array}$$

The block IFT represents the constraints associated with the inverse Fourier transform, and it is assumed to be invariant for a given set of data. The blocks WLC and RMS C are associated with well-log constraints and RMS velocity constraints, respectively. These blocks may or may not be present in the problem. Furthermore, when present, they may be changing across the section. (i.e. A may then be changing across the section; case (d) of the previous section).

We start by asserting that for reasonable quality seismic data the assumption that the ith+1 trace is similar to the ith

trace holds true except for sections corresponding to very complex geology. Furthermore, since the same energy source is used in the experiment, it can be expected that after the appropriate balancing (processing) is used the signal energy is concentrated in a given frequency band which is independent of trace index.

If we avoid the use of objective function weighting and polarity constraints, we encounter a problem corresponding to the one outlined in case (a). If we desire objective function weighting, the problem we confront is the one outlined in case (c). Imposing polarity constraints involves problems similar to the types described in cases (b) and (d). Other combinations of problem characteristics are possible, but for practical purposes we restrict our attention to those outlined above.

5.6 EXAMPLE

For the purpose of assessing the performance of the algorithm we have used the set of real data shown in Figure 5-3. Before applying the algorithm we have phase-corrected and deconvolved the data using a minimum entropy approach. Additionally, to improve the signal to noise ratio we have used 3-trace principal component analysis (Oldenburg et al (1983)). The results are shown in Figure 5-4. We then applied the LP algorithm to the data of Figure 5-4 using the following modes:

a) objective function weighting, no polarity constraints.

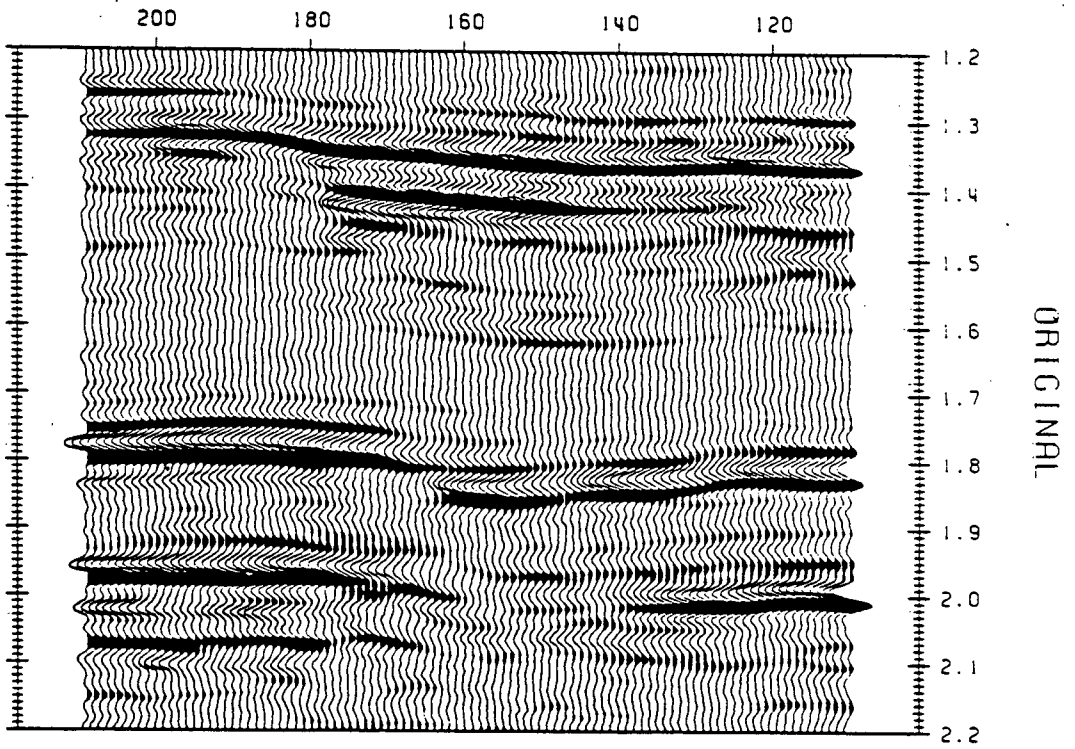

Figure 5-3

Stacked section featuring a reasonable trace to trace correlation.

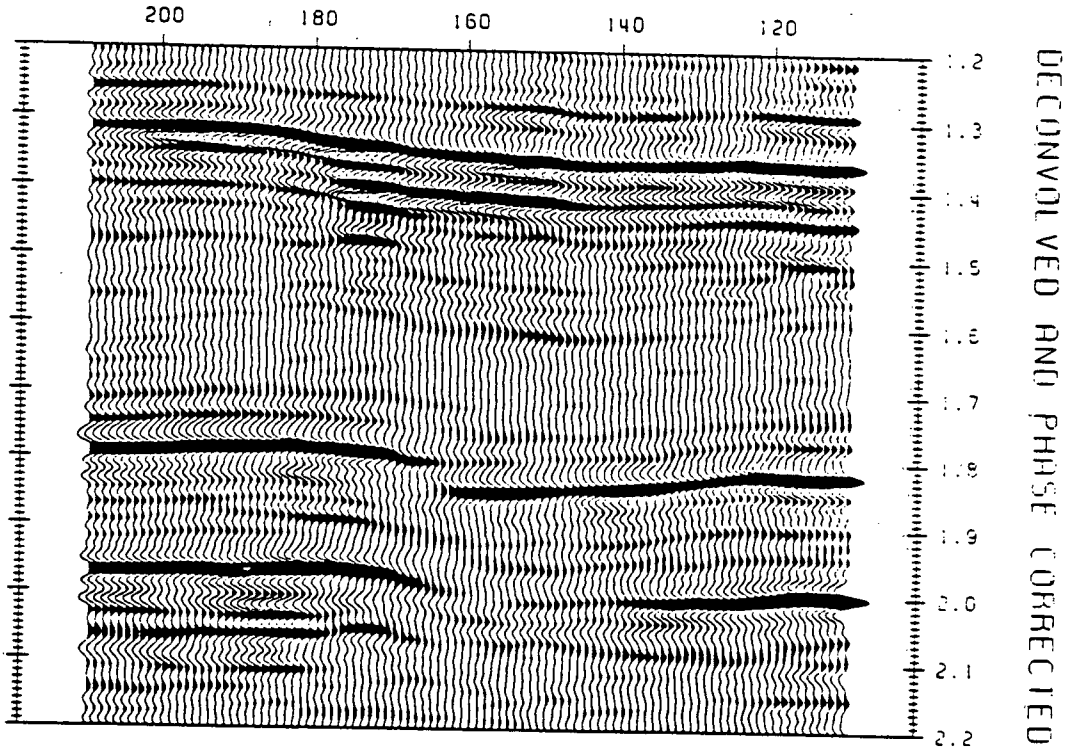

Figure 5-4

The data of Figure 5-3 after spectral whitening, phase correction and the application of three-trace principal component SNR enhancement.

b) polarity constraints, no objective function weighting.

c) no polarity constraints, no objective function weighting

d) polarity constraints and objective function weighting

Modes (a) to (d) were executed twice,once with the multi-trace Simplex approach, and again with the trace-by-trace Simplex approach. For reasons of run efficiency and memory requirements, the data were processed in short windows of 64 samples each. The CPU run times (Vax 11/780) are given in Table 5.1. In most cases the multi-trace Simplex approach proves to be more efficient than the trace-by-trace approach, with the exception being mode (c). For this mode numerical checks showed that although the last solution seems to be 'close' to the current one, the Simplex search may lead to it in a round-about path. This is not unexpected, since in this case both the starting solution and the objective function are updated from the previous, so that our supposition that geometric 'closeness' equals algorithmic 'closeness' breaks down. It should be noted however, that for a linear programming run executed in mode (c), the CPU run time is reduced (for this set of data) by a factor of four.

Finally, in order to compare processing results, we present in Figure 5-5 the reflectivity obtained via the multi-trace Simplex (mode (c)), and that associated with the trace-by-trace Simplex (mode (d)), shown in Figure 5-6. These results generally agree quite well, except in some small amplitude events. This should be expected, since the objective function weighting tends to discriminate against those events.

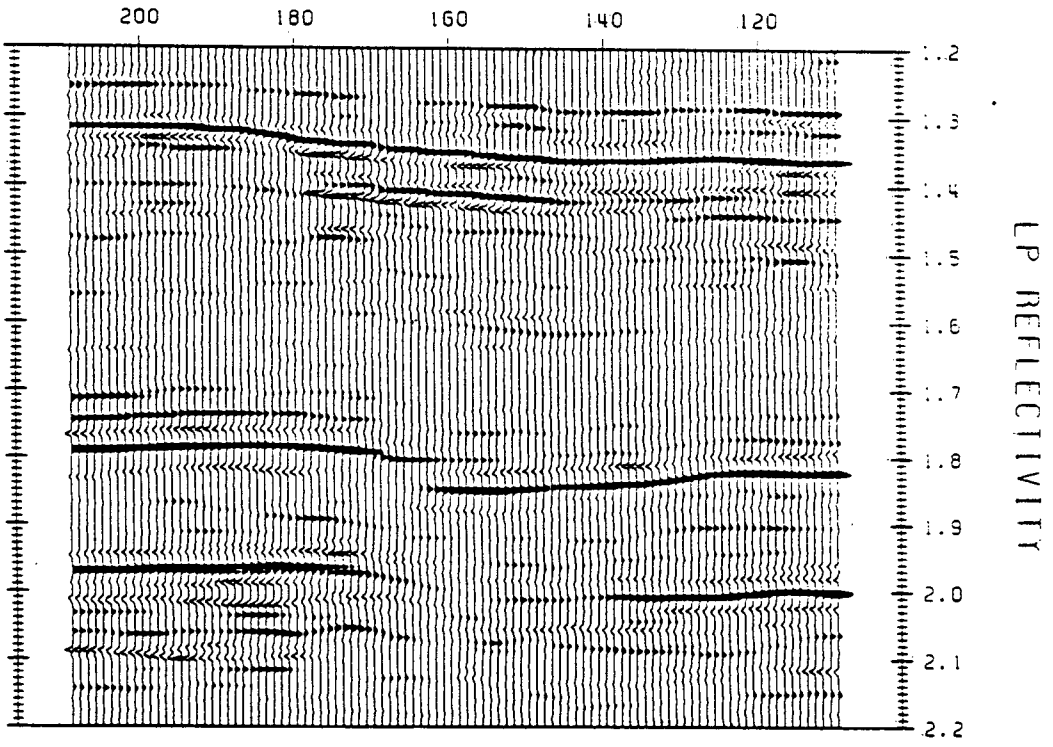

Figure 5-5

The data of figure 5-4 after linear programming deconvolution with the multitrace simplex mode.

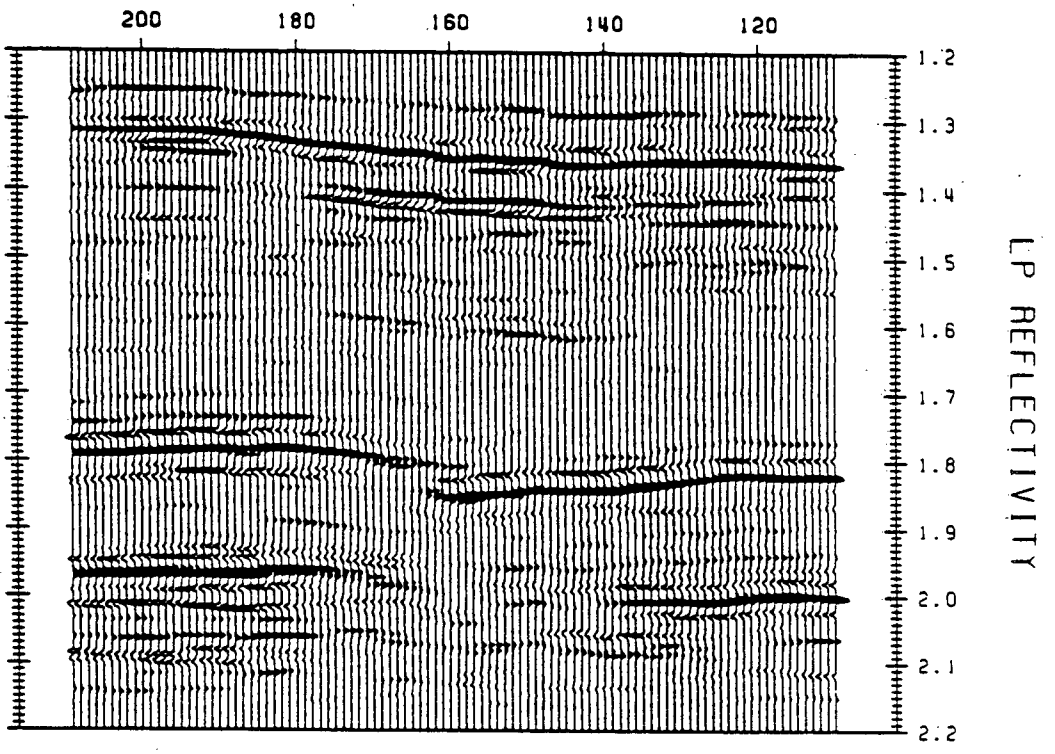

Figure 5-6

The data of figure 5-4 after linear programming deconvolution with objective function weights and polarity constraints.

For completeness we attach the pseudo-impedance section corresponding to the reflectivity of Figure 5-5. This section is shown in Figure 5-7 in line plot, and in Figure 5-8 in grey shades plot. The impedance produced ties well with a velocity log obtained in a nearby well (not shown here). The improvement of the section in Figure 5-8 over that of Figure 5-3 is quite clear and does not require elaboration.

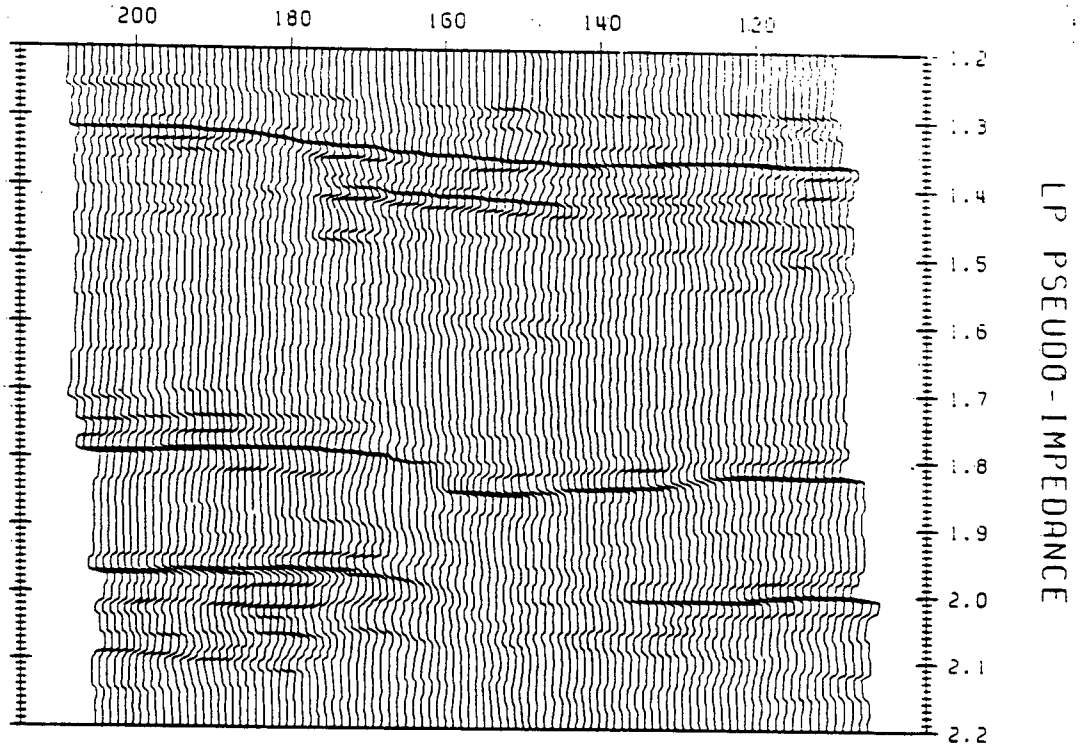

Figure 5-7

The pseudo-impedance section obtained via the integration of the data in figure 5-5.

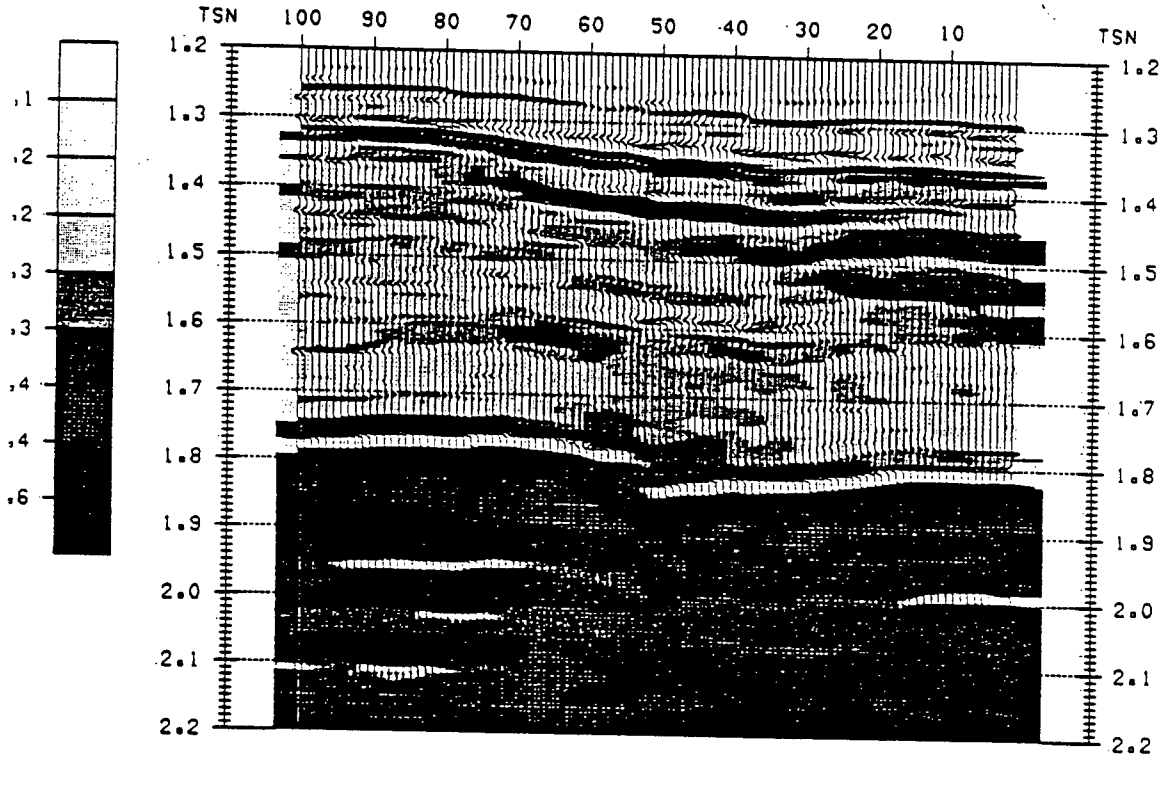

Figure 5-8

Pseudo-impedance section overlaid on the full band LP reflectivity. This type of display seems to enhance the interpretability of the data.

Table 5.1

MW	MP	NFAST	CPU (sec.)
1	1	0	789.7
1	1	1	1232.7
0	0	0	2976.4
0	0	1	713.4
1	0	0	1398.4
1	0	1	1358.1
0	1	0	1305.8
0	1	1	1175.0

Note: MP.....0 no polarity constraints used
.....1 polarity constraints used
MW.....0 no objective function weighting
.....1 objective function weighting used
NFAST..0 trace by trace Simplex used
..1 multi-trace Simplex used

Data contains: 100 traces, one second long each, sampling interval 0.004 sec, frequency band 12-40 Hz.

5.7 SUMMARY

A number of options which yield an increase in the efficiency of the linear programming method were discussed. These methods do not require that certain features of the model be predetermined or selectively weighted, as is the case with previous techniques (Oldenburg et al. 1983, and Scheuer, 1981). The result is that now the linear programming method can be used to process reflection seismic data in a variety of different modes, all in reasonable execution time. Comparison of the results of the processing (Figures 5-8) to the input data (Figure 5-3) demonstrates the efficacy of the method.

CHAPTER VI: PRE-INVERSION SCALING OF REFLECTION SEISMOGRAMS

6.1 INTRODUCTION

As described in the previous chapters, approaches to the estimation of acoustic impedance from reflection seismograms involve construction of a full-band reflectivity section from the input bandlimited section. Some of these approaches also advocate the direct incorporation of well-log and stacking velocity information into the estimation process. An impediment to these methods for both the conversion of the full-band reflectivity to impedance, as well as the incorporation of the velocity information, is the lack of true amplitude information in the stacked section. Due to difficulties in data acquisition and subsequent processing, the final stacked section will generally require scaling prior to the impedance inversion process.

To understand the importance of correct scaling, let us assume that the estimated reflection series $\tilde{r}_j$, j=1,...N, is a scaled version of the true reflection series r_j , j=1,...N; that is:

$$\tilde{r}_j = a \cdot r_j \quad \text{for all } j \tag{6.1}$$

with a being a real constant, and r_j being the jth reflection coefficient.

The impedance, $\zeta_j = \rho_j \cdot v_j$, is calculated from the estimated reflection series using the linearized approximation (see Oldenburg et al, 1984):

$$\begin{aligned} \zeta_j &= \zeta_0 \exp\left[2 \sum_{i=1}^{j-1} \tilde{r}_i\right] \\ &= \zeta_0 \exp\left[2 \cdot \alpha \sum_{i=1}^{j-1} r_i\right] \end{aligned} \qquad (6.2)$$

It is clear that incorrect values of the acoustic impedance are obtained if α is much larger or much smaller than 1. Furthermore, in this case, the set of external constraints applied to the reflectivity construction will be incapable of supplying true physical meaning. Hence, the inconsistency between the information contained in the seismograms and that supplied by the external constraints will annihilate the advantage to be gained by inversion of the combined data set.

To avoid this inconsistency, we propose a method for the estimation of the scale factor α using the observed seismograms, and their associated stacking velocities and well-log impedances when available.

6.2 METHOD

6.2.1 GENERAL

For the purpose of scaling we recognize two types of information routinely available to processors of seismic data. The first type can be obtained directly from the bandlimited stacked section and we consider it as the relative information. The second set of information is available from well-logs or from stacking velocities and it is termed here as the absolute information. The proposed scaling algorithm makes use of a linear relationship (true for reflection coefficients smaller than 0.3), which allows direct comparison between those two information sets and hence the estimation of the scaling factor a.

Although we will be considering only the case of a time independent scaling factor (as reflected by equation (6.1)), our method can be applied to cases of a time dependent scaling function by applying the analysis to a number of successive time windows and then interpolating the results.

6.2.2 THE CONSTRUCTION OF SPIKY REFLECTIVITY FUNCTION - RELATIVE INFORMATION

The proposed method of scale factor evaluation is based on recently introduced algorithms which use the information contained in band-limited seismograms to predict the missing portions of the frequency band. These algorithms include a linear programming approach (Taylor et al. 1979; Levy and Fullagar 1981; Scheuer 1981; and Oldenburg et al. 1983), an autoregressive technique (Scheuer,1981; Oldenburg et al. 1983; and Walker and Ulrych 1983), and a non-linear reflectivity estimation (Bilgeri and Carlini, 1981). For the benefit of the interested reader, we have included in Appendix 6-A a short description of the autoregressive deconvolution scheme.

The final result in all these schemes is a 'spiky', full band reflectivity series, $\tilde{r}_j$, $j=1,\ldots N$. In the following, we assume that the predicted low frequencies obtained via the application of these deconvolution algorithms, followed by integration and exponentiation of the resultant reflectivities (as in equation (6.2)), will yield reasonable estimates of the trend of the impedance function in at least some time windows. Since the reflectivity functions $\tilde{r}_j$ to be integrated are scaled by some arbitrary real factor yet to be determined, these functions constitute our scaled, or relative information.

6.2.3 WELL-LOGS OR STACKING VELOCITIES - ABSOLUTE INFORMATION

Our absolute information is obtained from either the inversion of stacking velocities to give interval velocities, or directly from well-log data.

1. Absolute Information from Well-Log Data

When both velocity and density logs are available, we can directly calculate the acoustic impedance as a function of time. If the density-log is not available we assume a density-velocity power law (that is, $\rho=A\cdot v^{p}(t)$), and estimate the acoustic impedance using the relationship:

$$\zeta(t) = A\cdot v^{1+p}(t). \qquad (6.3)$$

Note that substituting A=1, and p=0 in the above density power law amounts to the constant density approximation, while A=0.23 and p=0.25 is the usual power law as suggested in Anstey, 1977 (p.88).

2. Absolute information from Stacking-Velocities

When only stacking velocities are available, the inversion algorithms described in Oldenburg et al. (1984) give acceptable representations (v^{c}_{j}, j=1,...N) of the true interval velocity (v^{t}_{j}, j=1,...N). Again, using the density power law given above, we convert $v^{c}(t)$ to estimated impedance. A detailed description

of the stacking to interval velocity inversion schemes used in this work was given in Chapter IV.

6.2.4 COMPARISON OF THE ABSOLUTE AND THE RELATIVE INFORMATION.

The estimation of the scaling factor a is effected by comparison of the absolute and relative information at selected time windows. To allow this comparison, we rewrite the approximate relation between reflectivity and impedance given in equation (6.2), thereby introducing the pseudo-impedance, η:

$$\ln(\zeta_j/\zeta_0) = \eta_j = 2\sum_{i=1}^{j-1} r_i \qquad j > 1$$

$$= 0 \qquad j = 1 \qquad (6.4)$$

Assuming a time independent scaling function, we substitute equation (6.1) into (6.4) to get our relative pseudo-impedance estimates from the constructed full-band reflectivities:

$$\tilde{\eta}_j = 2a\sum_{i=1}^{j-1} r_i \qquad j > 1$$

$$= 0 \qquad j = 1 \qquad (6.5)$$

Our estimate of the absolute pseudo-impedance from well-log data will be:

(a) density log available

$$\bar{\eta}_j = \ln(\zeta_j / \zeta_0)$$

or (using equation 6.3): (6.6)

(b) density log unavailable

$$\bar{\eta}_j = (1+p)\cdot \ln(v_j^t / v_0^t)$$

Similarly, from interval velocities inverted from stacking velocities, our estimate of the absolute pseudo-impedance is:

$$\bar{\eta}_j = (1+p)\cdot \ln(v_j^c / v_0^c) \qquad (6.7)$$

Since the pseudo-impedance $\tilde{\eta}_j$ is linear with respect to the scale factor a, comparison of $\tilde{\eta}_j$ and $\bar{\eta}_j$, (j=1,....N) will yield the desired scaling factor a.

6.2.5 CONSIDERATIONS PERTAINING TO THE USE OF STACKING VELOCITIES FOR SCALING.

As the reader may have already realized, the velocity inversion algorithms described in Chapter IV are strictly applicable to a one dimensional earth. Consequently, when steeply dipping events are evident on the stacked section, the proposed algorithm is not likely to yield reasonable results unless some correction is applied to the stacking velocities prior to inversion (see for example, Kesmarky 1977). Furthermore, since the interval velocity profile obtained from the inversion of the stacking velocities is at best an average of the true velocity curve, a point by point comparison of $\tilde{\eta}$ and $\bar{\eta}$ is undesirable. Instead, box-car averages over a number (N/M) of windows (each M samples long), are used to get a series of estimates of the scale factor:

$$a_i = \frac{\sum_{j=(i-1)M+1}^{i\cdot M} \tilde{\eta}_j}{\sum_{j=(i-1)M+1}^{i\cdot M} \bar{\eta}_j}, \qquad i=1,N/M \qquad (6.8)$$

The final estimate of the scale factor for the seismogram is obtained from the median of the series $\{ a_i \}$, so as to avoid incorporation of statistical outliers in this estimate.

6.2.6 CONSIDERATIONS PERTAINING TO LOCALIZED SPIKING DECONVOLUTION FAILURES.

The approach summarized in equations (6.5), (6.6), (6.7) and (6.8) suffers from the dependence of values of $\tilde{\eta}$ at any given time on the correctness of preceding values at smaller times, that is:

$$\tilde{\eta}_j = 2 \sum_{i=1}^{j-1} r = \tilde{\eta}_{j-1} + 2\tilde{r}_{j-1}.$$

Since slow changes in earth impedance as a function of depth will not produce a clear manifestation in the recorded reflection data, they may not appear in the pseudo-impedances $\tilde{\eta}$ obtained via summation of the reflectivities from either linear programming or auto-regressive spiking deconvolution. However, the shape of the pseudo-impedance curve in some given time windows may still be correct. Thus, to reduce the effects of the dependency of $\tilde{\eta}$ on previous values, only the relative changes in pseudo-impedance in each window are considered. That is:

$$a = \frac{\sum_{j=(i-1)M+1}^{i\cdot M} (\tilde{\eta}_j - \tilde{\eta}_{(i-1)M})}{\sum_{j=(i-1)M+1}^{i\cdot M} (\bar{\eta}_j - \bar{\eta}_{(i-1)\cdot M})} \qquad (6.9)$$

Furthermore, due to the nature of both the LP and the AR deconvolution algorithms (both search for minimum structure solutions), it is expected that better shape-wise estimates of $\tilde{\eta}$ will be obtained at regions of rapid impedance changes. Therefore, a values from windows corresponding to this type of impedance zone may be weighted more heavily in the final median calculation. The detection of this type of impedance zone and the assignment of the appropriate weights is based on the degree of correlation exhibited by $\tilde{\eta}$ and $\bar{\eta}$ in the given time window. This correlation factor is estimated from the dot product of these two functions.

6.3 SYNTHETIC EXAMPLES

6.3.1 LAYERED EARTH MODEL WITH WELL DEFINED LAYER BOUNDARIES.

The reflectivity function (Figure 6-1a) corresponding to the true velocity model of Figure 6-1d has been calculated under the assumption of constant density. After band-limiting this

reflectivity function (10-50Hz), adding 5% random noise, and scaling the result by a factor of 100, we obtained the synthetic data shown in Figure 6-1b. Using this synthetic as an input to the linear programmming (LP) deconvolution routine, the resultant full band reflectivity $\tilde{r}$ is constructed and plotted in Figure 6-1c. $\tilde{r}$ constitutes our relative information.

Using the true velocity model of Figure 6-1d, we have estimated the RMS velocity curve shown in Figure 6-1e. Five selected points of the latter (marked on Figure 6-1e), together with a point constraint of 12 Kfeet/sec at 1.8 sec (assumed to be available from well-log information) were used in the Backus-Gilbert flattest-model inversion (Oldenburg et al. 1983), to yield the estimated interval velocity, our absolute information (Figure 6-1f).

Using equations (6.5), and (6.7), we obtain pseudo-impedances $\tilde{\eta}$ and $\bar{\eta}$, shown in Figure 6-2b and 2c, respectively. We then applied equation (6.8) with N=512 and M=128, to get a series of four estimates of the scale factor a. These are listed in Table 6-1 for the corresponding time windows.

As seen from Figure 6-2, both $\tilde{\eta}$ and $\bar{\eta}$ resemble the true pseudo-impedance (Figure 6-2a) quite well. Hence, as expected, the final estimated value of 122 for the scale factor is in good agreement with the true value of 100.

Table 6-1:
Scale factor evaluation for example in Fig. 2 and 3.
N=512, M=128
True scale factor=100

i	a
1	71
2	148
3	122
4	105

Median = 122.
Mean = 112.

To complete the process, we have rescaled the input seismogram (Figure 6-1b) by a=1/122, and performed the acoustic impedance inversion (LP), using the synthetic seismogram and a set of stacking velocity constraints (Oldenburg et al. 1984). The final result overlayed on the true impedance curve is shown in Figure 6-3.

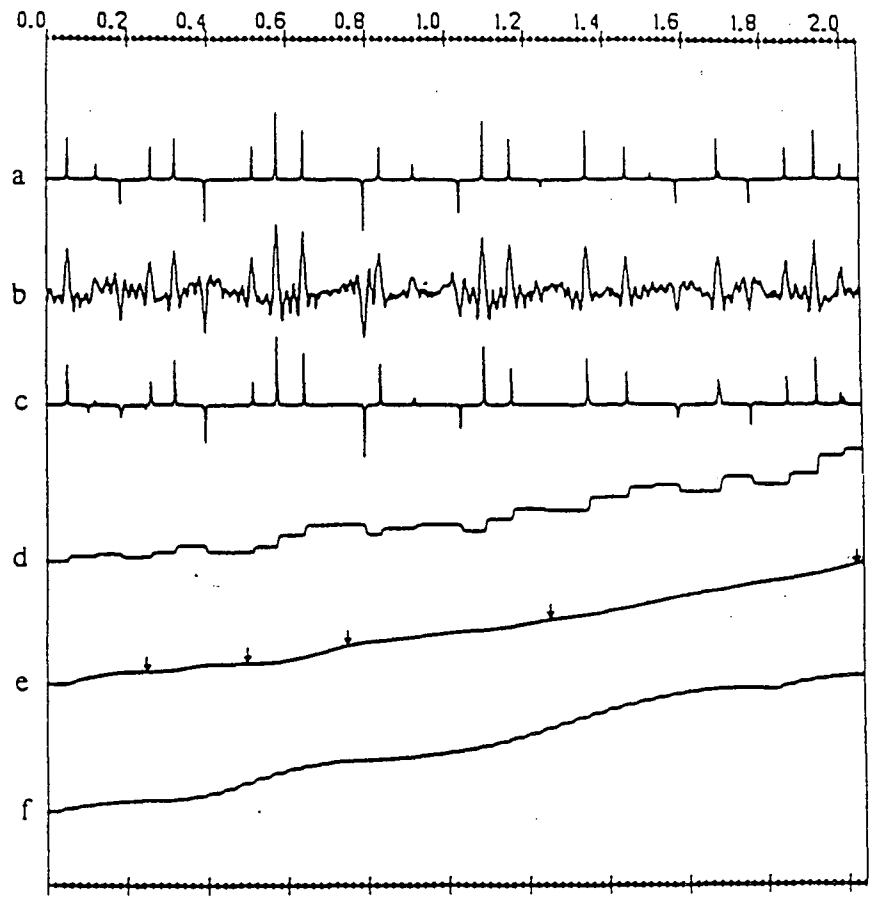

Figure 6-1

(a) The reflectivity series corresponding to the velocity model of Figure 6-1d. (b) The series in (a) after the application of a 10-50 hz. bandpass filter and the addition of random noise. (c) The series in (b) after LP deconvolution. (d) The true velocity model. (e) RMS velocity corresponding to the velocity model in (d). (f) The estimated interval velocity obtained from the five RMS picks marked on (e) via the Backus-Gilbert inversion.

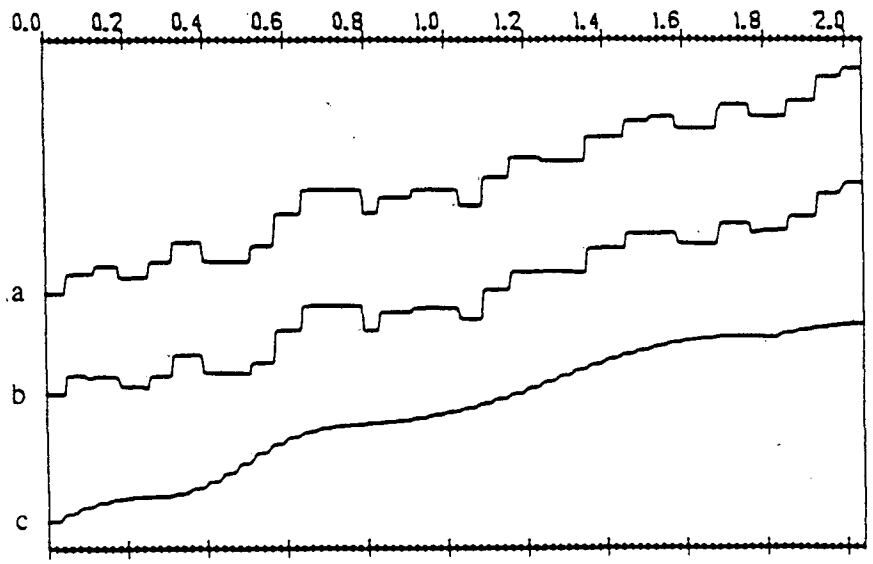

Figure 6-2

(a) The true pseudo-impedance function. (b) The pseudo-impedance function calculated from the constructed LP reflectivity. (c) The pseudo-impedance function calculated from the constructed interval velocity model.

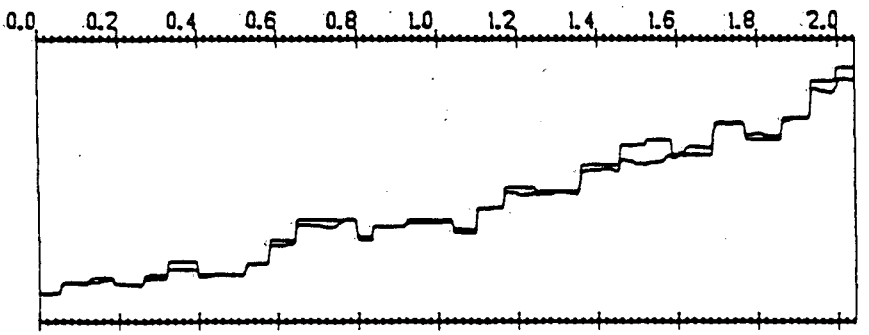

Figure 6-3

The reconstructed acoustic impedance function obtained via constrained inversion. The seismogram in Figure 6-1b was scaled by a factor of 1/122 and the result together with the set of stacking velocities (marked on Figure 6-1e) was used in the inversion. The true velocity model is overlaid on the figure.

6.3.2 LAYERED EARTH MODEL WITH SLOWLY VARYING IMPEDANCE ZONES.

As was discussed previously, both the LP and AR deconvolution algorithms minimize an objective function which implies minimum earth structure. Consequently, it can be expected that the relatively small reflection coefficients (relative amplitude is defined by frequency band-width and error allowance used in the deconvolution) will not be manifested in the estimated reflectivity function $\tilde{r}$. Due to these omissions, conversion of $\tilde{r}$ into pseudo-impedance $\tilde{\eta}$ may yield results which are substantially different (in a global sense) from those given by the true earth model. However, in time windows which do not include large ramp-like impedance components, the representation given by $\tilde{\eta}$ may still be shape-wise acceptable. When this is the case, the scaling algorithm summarized by equations (6.5), (6.6), (6.7) and (6.9) is still expected to yield reasonable results.

To demonstrate the viability of the proposed scaling scheme in an environment which contains ramp-like impedance components, we have constructed the true velocity profile shown in Figure 6-4d. The associated true reflectivity, and RMS velocity curve are shown in figures 6-4a and 4e, respectively. We band-pass (10-50Hz) the reflectivity of Figure 6-4a, add 5% random noise, and scale it by a factor of 100 to obtain the synthetic seismogram (Figure 6-4b) to be used in this example.

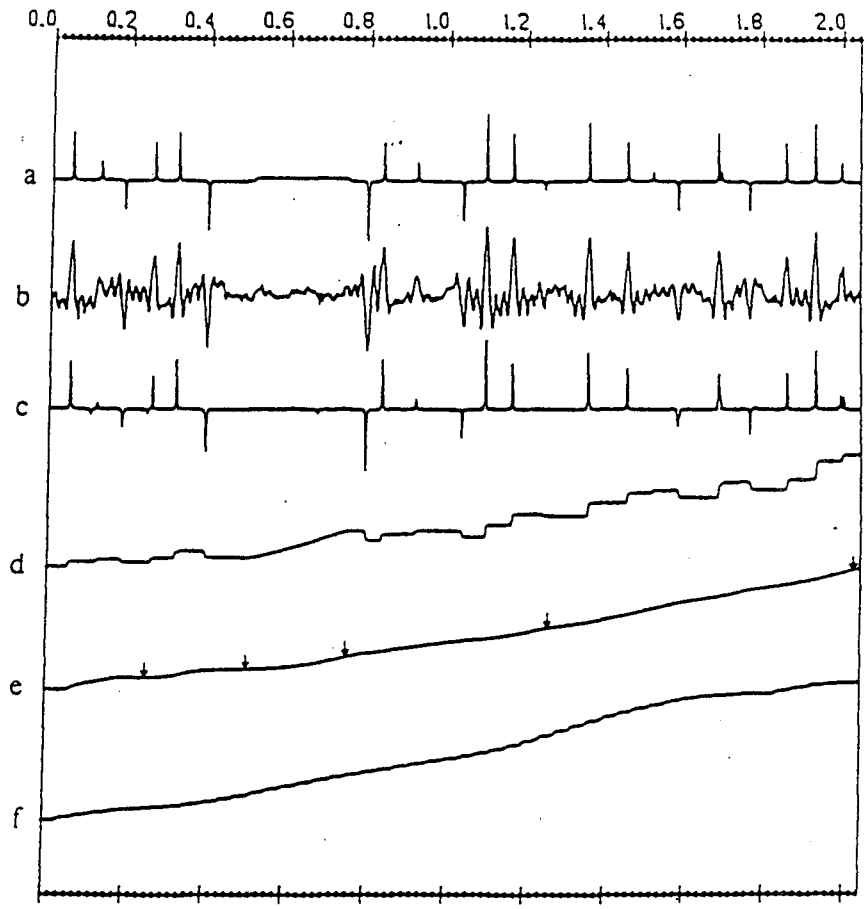

Figure 6-4

Same as Figure 6-1. This time, a ramp-like component is added to the velocity model between 0.5 and 0.7 seconds. (a) The reflectivity series corresponding to the velocity model of Figure 6-4d. (b) The series in (a) after the application of a 10-50 hz. bandpass filter and the addition of random noise. (c) The series in (b) after LP deconvolution. (d) The true velocity model. (e) RMS velocity corresponding to the velocity model in (d). (f) The estimated interval velocity obtained from the five RMS picks marked on (e) via the Backus-Gilbert inversion.

Application of the linear programming deconvolution to the data of Figure 6-4b, yields the full-band reflectivity estimate $\tilde{r}$ (Figure 6-4c), while the inversion of the RMS velocities (pick positions for inversion purposes are marked in Figure 6-4e) gives the estimated interval velocity profile of Figure 6-4f. Using equations (6.5) and (6.7) we converted the data in figures 6-4d, 4c, and 4f into pseudo-impedance and the results are shown in Figure 6-5a , 5b, and 5c, respectively. Inspection of Figure 6-5 reveals good shape-wise agreement between the true pseudo-impedance and the one estimated from $\tilde{r}$ for windows 1, 3, and 4. However, the correlation exhibited in the second window (corresponding to the ramp-like impedance structure) is quite poor. Using equations (6.8) and (6.9) on the data of Figures 6-5b and 5c with N=512 and M=128, we obtain the series of estimated scale factors a which is summarized in Table 6-2. The median of the series calculated by equation (6.8) is 61, while that corresponding to equation (6.9) is 97. Obviously, the latter estimate is good and suggests that a scaling algorithm based on equations (6.5), (6.6) (or (6.7)), and (6.9) can produce acceptable results even when the LP deconvolution scheme fails at some isolated time windows. It is that set of equations which will be used throughout the remainder of this work.

Table 6-2:

Scale factor evaluation

for example in Fig. 6-5.

N=512, M=1.28

True scale factor = 100

I	α(from eq.6.6)	α(from eq.6.7)
1	72.	72.
2	23.	-4.
3	44.	129.
4	61.	97.

Median (from eq. 6.8) = 61.

Mean (from eq. 6.8) = 50.

Median (from eq. 6.9) = 97.

Mean (from eq. 6.9) = 73.

Again we complete the process by running the LP acoustic impedance inversion algorithm on the data of Figure 6-4b scaled by 1/97 with a set of constraints obtained from the inverted interval velocity (shown in Figure 6-4f). The result, overlayed on the true velocity function is shown in Figure 6-6.

6.4 REAL DATA EXAMPLES

In the following examples we demonstrate the application of the above scaling method to cases where: (a) only well-log information is available and (b) only stacking velocities are available. Our input stacked sections (sampled at 4Ms), have been subjected to a normal (pre-stack) processing sequence which included predictive deconvolution for short period multiple suppression. Subsequently (post-stack), we have whitened the spectral band (10-40Hz) and corrected the phase of the interpreter's wavelet so that the residual wavelet is presumed zero-phase. These final sections constitute the input to our scaling algorithm.

6.4.1 SCALING DATA USING WELL-LOG INFORMATION

Given the stacked section shown in Figure 6-7 and the velocity log corresponding to a well in the vicinity of trace 70 (Figure 6-8), we wish to prescale our data for subsequent

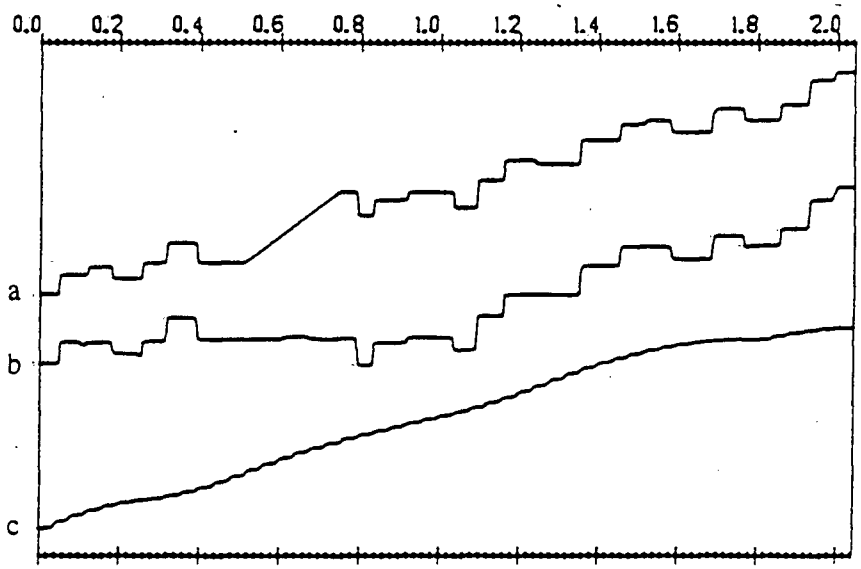

Figure 6-5

(a) The true pseudo-impedance function. (b) The pseudo-impedance function calculated from the reconstructed LP reflectivity. (c) The pseudo-impedance function calculated from the constructed interval velocity model.

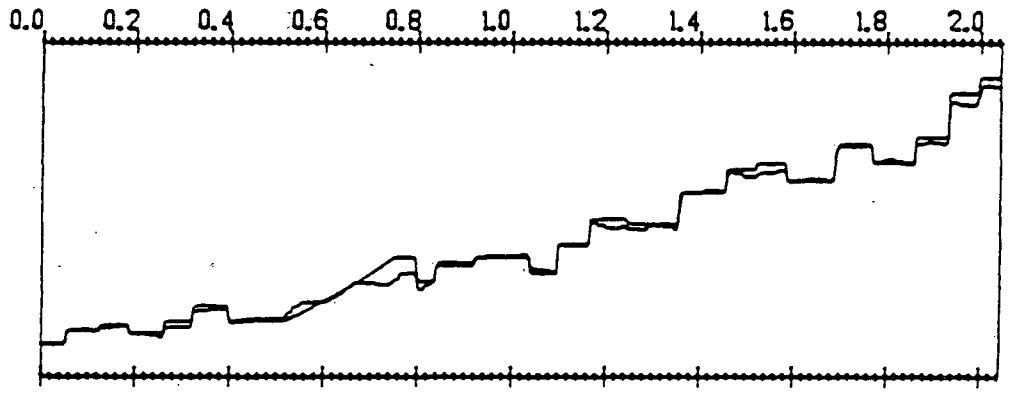

Figure 6-6

The velocity function obtained from the constrained inversion superimposed on the true velocity model. Input consists of the scaled seismogram (Figure 6-4b) and five stacking velocity estimates (marked on Figure 6-4e).

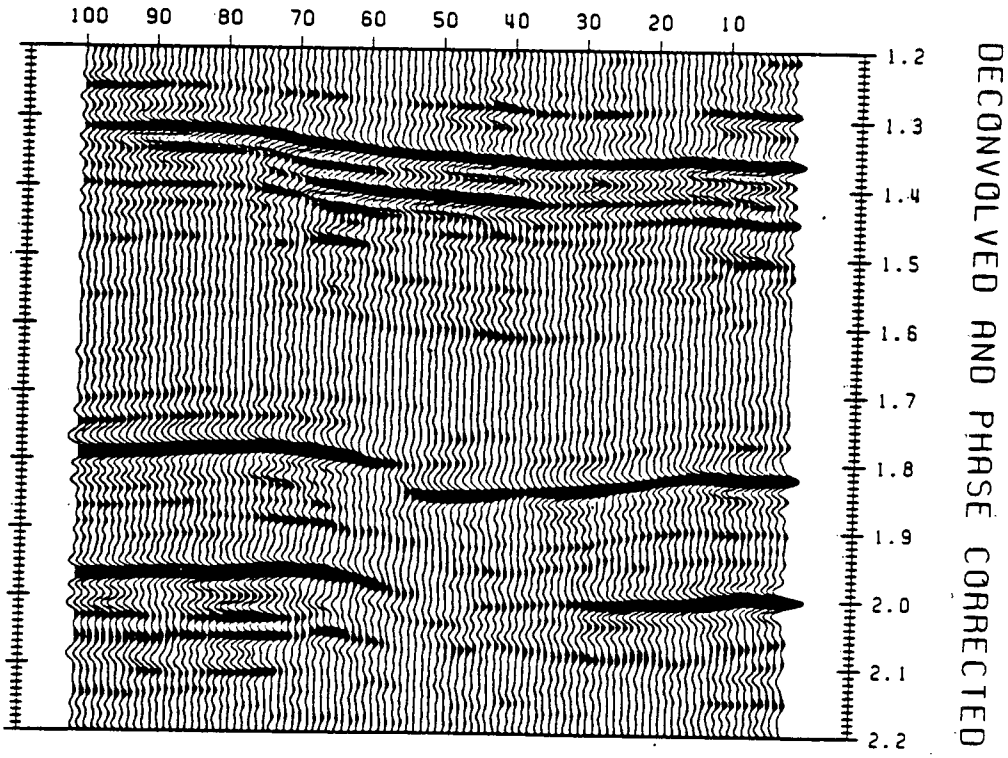

Figure 6-7

Input seismograms after post stack spectral whitening and phase correction.

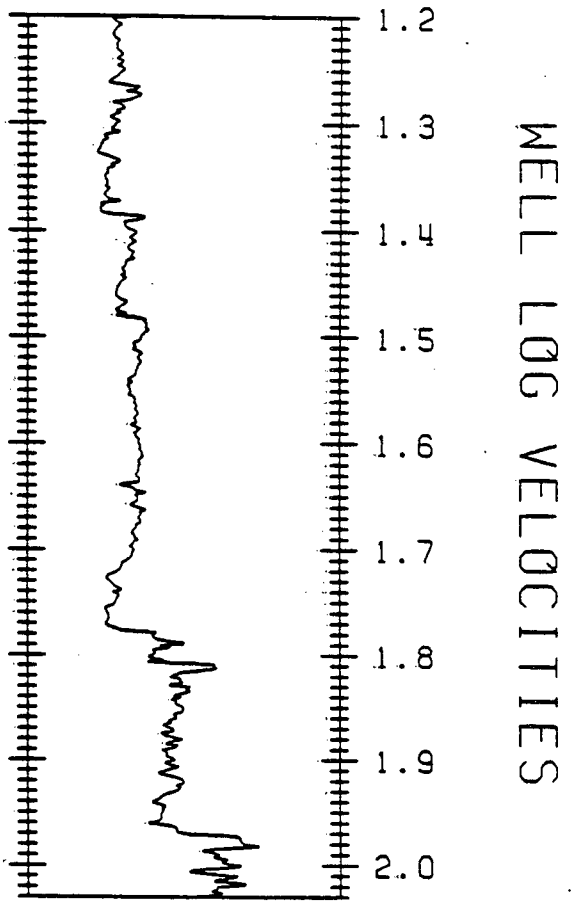

Figure 6-8

Sonic log from a well at the vicinity of trace 70.

impedance inversion processing.

The first step required in our scaling scheme is the spiking deconvolution of the input data set. Figure 6-9 represents the output of the linear programming deconvolution applied to our input. This wide-band reflectivity is assumed to be a reasonable representation of the local primary reflectivity function, and upon integration it yields the calculated pseudo-impedance section shown in Figure 6-10. Inspection of the latter result shows that the low frequency trend exhibited by the velocity log has been reproduced faithfully. Consequently, direct comparison of the calculated pseudo-impedance to the well-log pseudo-impedance is likely to produce the desired scaling factor. We have compared these quantities for the near-well traces (#'s 60 to 80) and the resultant scaling factor was found to be 1.3.

As a last step in our process we have rescaled the original data, interpolated a number of velocities with their associated confidence bounds along a number of constraint horizons (marked on Figure 6-10), and executed the acoustic impedance inversion procedure using the scaled data and the afore mentioned constraints. Figure 6-11 represents the final output of the impedance inversion scheme. In this figure we have overlayed the pseudo-velocities (grey shades) over the wide band constrained reflectivity section (this reflectivity section is consistent with the observed well-log information).

Our final results are in a form suitable for normal

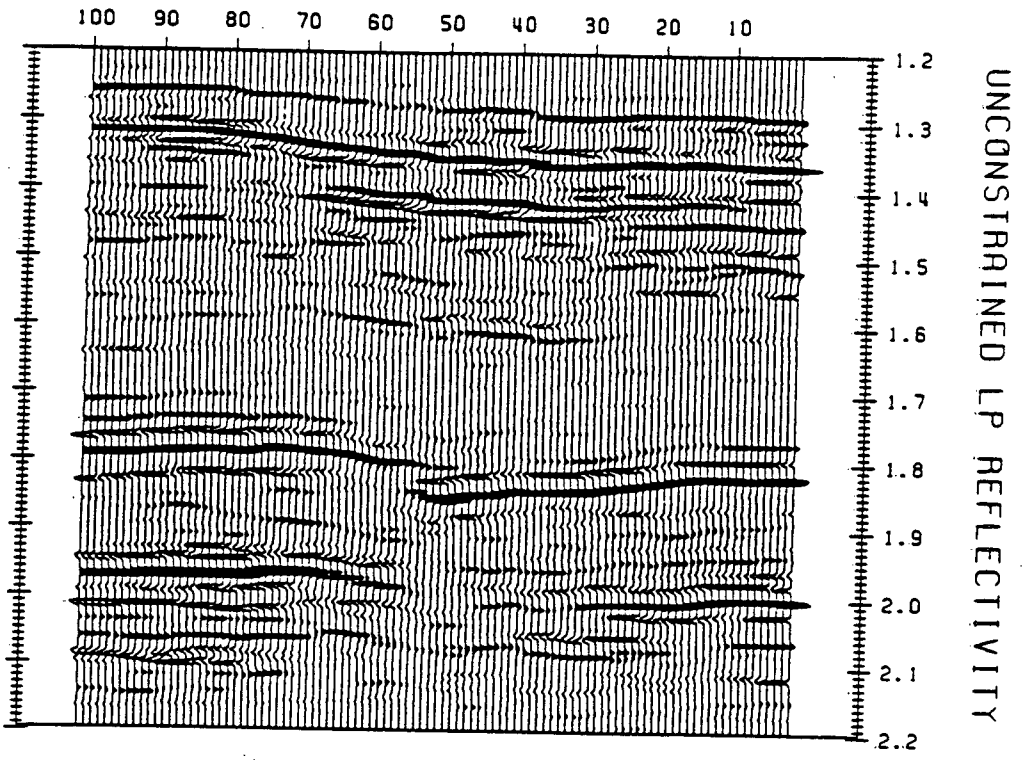

Figure 6-9

The data of Figure 6-7 after application of linear programming deconvolution.

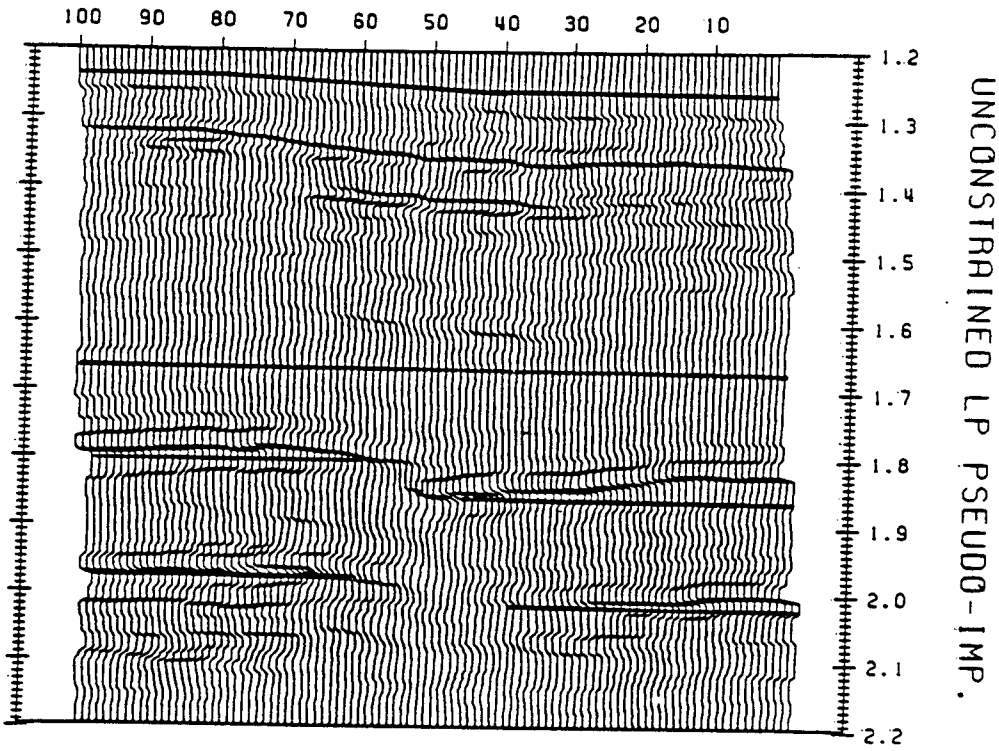

Figure 6-10

The pseudo-impedance section obtained via the integration of the data in Figure 6-9. These data were used in conjunction with the sonic log for the estimation of a scaling factor.

interpretation work. Furthermore, with appropriate caution (as indicated by the constraint's confidence bounds supplied to the inversion), they may also be used for inference of some petrophysical parameters like porosity, fluid saturation and overpressure (Angeleri and Carpi, 1982, Bilgeri and Ademeno, 1982). These parameters are measurable at the well site, and may be extrapolated away from this site by comparing pseudo-velocity values along a given formation to those observed on the near well traces.

6.4.2 SCALING DATA USING STACKING VELOCITY INFORMATION

When well-log information is not available, and the observed local geology is appropriate (that is, no steeply dipping structures are present), it is possible to use the stacking velocities for scaling purposes.

Given the data of Figure 6-12, and the corresponding set of stacking velocities we start our scaling scheme by inverting the stacking velocity set via the Backus-Gilbert methodology. The result of this inversion, that is the smooth representation of the interval velocities (Figure 6-13), is converted to a pseudo-impedance section.

Next, we have applied the linear programming deconvolution to the data of Figure 6-12 and converted the output wide-band reflectivities to a pseudo-impedance section. Direct comparison of these two information sets yields a scaling factor of .008.

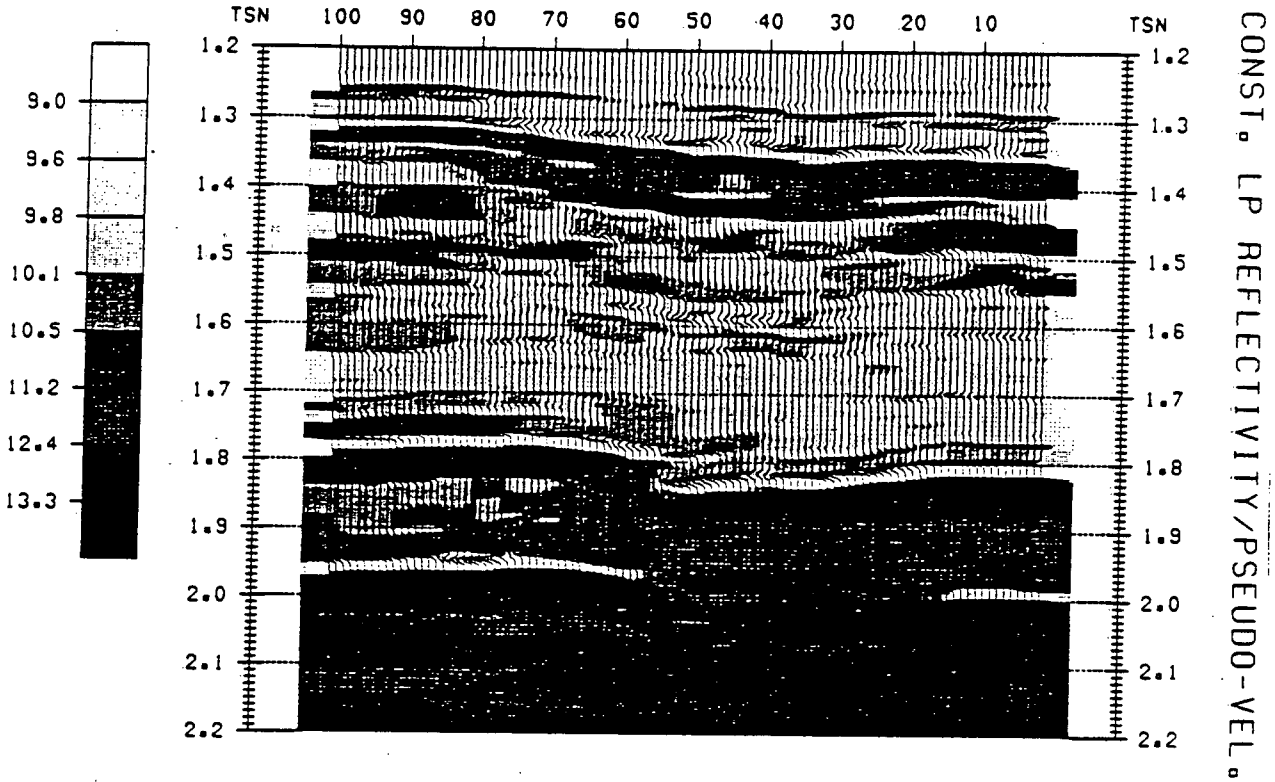

Figure 6-11

The result of a constrained inversion. Full band reflectivity section is overlaid on top of the pseudo-velocity section. Grey shades represent velocities in Kfeet/sec.

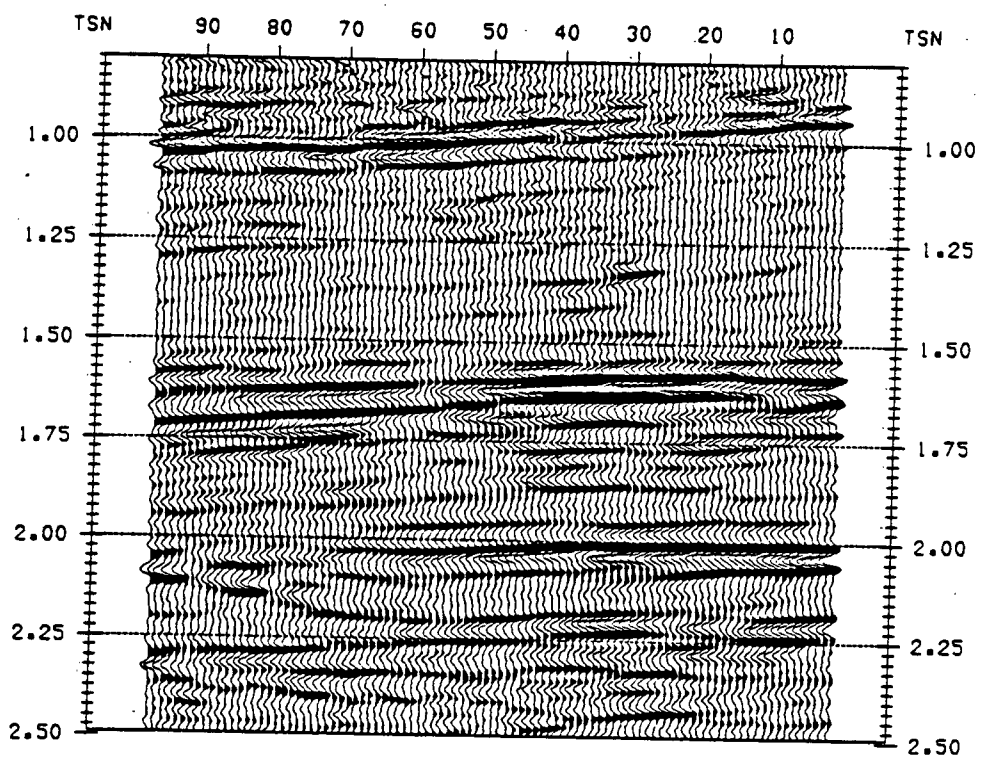

Figure 6-12

Input stacked section.

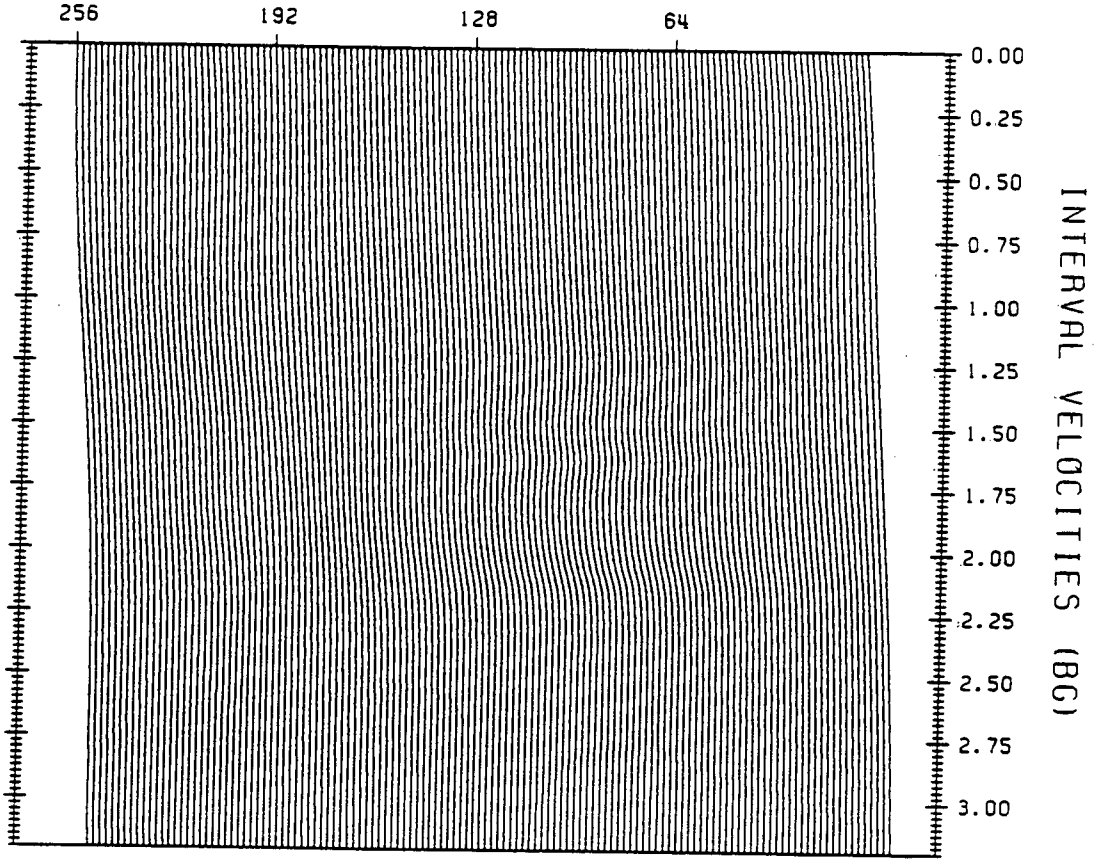

Figure 6-13

Interval velocity section obtained by the inversion of a set of stacking velocity profiles corresponding to the data in Figure 6-12. These interval velocities were used in conjunction with the unconstrained pseudo-velocities in the calculation of the required scaling factor.

Lastly, we have rescaled the original data, and executed the acoustic impedance inversion procedure using stacking velocity constraints (Oldenburg et al 1984). The obtained pseudo-velocities overlayed on the constrained wide-band reflectivities are shown in Figure 6-14. Again, the final output of our inversion appears to produce high quality results in which the obtained reflectivities are consistent with the observed stacking velocities. Interpretation of these results is in our opinion easier than that of the original section, while a higher degree of confidence can be placed on these results since a larger information set has been used in its construction.

6.5 CONCLUSION

We have presented a scaling method designed as a preparatory step to the acoustic impedance inversion of reflection seismograms. This method, which is applicable to cases where either well-log or stacking velocities are available, is shown to yield good results on data collected in a number of exploration areas. Nevertheless, in areas where the local impedance functions do not contain a number of sharp impedance discontinuities the proposed scheme may fail to yield acceptable results.

The design of our algorithm is limited to those inversion techniques which are capable of yielding a first order approximation to the low frequencies generally missing in normal

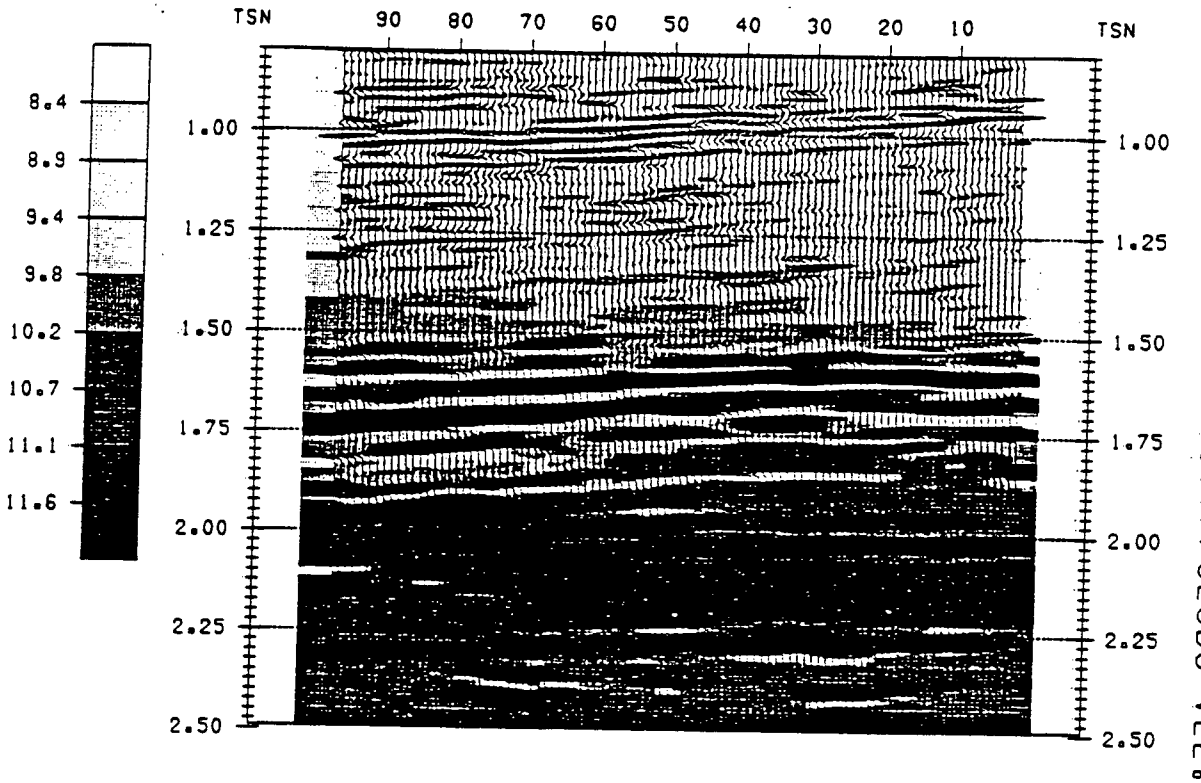

Figure 6-14

The result of a constrained inversion (with stacking velocities) as applied to the data of Figure 6-12. Full-band reflectivities are overlaid on the pseudo-velocity section. Grey shades represent velocities in Kfeet/sec.

seismic work. The use of these algorithms, supplemented by well-log information and stacking velocities, opens the door to powerful data processing techniques which utilize a larger information base to obtain both more reliable reflectivities, as well as the associated pseudo-velocity section.

CHAPTER VII: PRE-INVERSION CORRECTION OF WAVELET RESIDUAL PHASE

7.1 INTRODUCTION

The goal of most standard processing sequences is to produce a CDP stacked section in which each trace can be considered to be the earth's reflectivity function convolved with a zero phase wavelet. During the processing sequence every effort is made to eliminate the effects of the source signature and multiples, and to correct for instrument recording response, transmission losses, and attenuation. The deconvolution procedures normally used to correct for these effects make a number of assumptions concerning the phase properties of the effects themselves. When these assumptions are violated, as they often are, the deconvolved output may not exhibit the desired zero-phase interpreter's wavelet and a further phase correction will be required.

Phase distortions arise for a variety of reasons. We will give some of the causes here and in doing so, we shall distinguish between effects which operate directly on the source signature (for example, dispersion or processing filters), and those which arise due to our limited resolution and thereby cause 'apparent' phase shifts (e.g. interfering events like ghosts or short peg-leg multiples).

The effects of dispersion, attenuation, and supercritical

reflection on a given source signature have been extensively discussed in the seismological literature over the past 50 years. Examples of the phenomenae for simple models are given in Robinson (1979, 1980a and 1980b) where the modelling and removal of attenuation related dispersion via the Fourier scaling theorem is described. The effects of supercritical reflections have been studied by Arons and Yennie (1954). They isolated a set of water bottom reflections and showed how the phase of the wavelet is altered for post-critical reflections. The phenomenon of supercritical reflection is discussed in detail by Aki and Richards (1980).

Phase distortions are also incurred through the application of deconvolution filters. Most readers are familiar with these effects and hence we will only touch upon the matter lightly. The calculation of deconvolution filters is based upon a number of assumptions which are, at times, inconsistent with the conducted field experiment. In the case of an explosive source, it is generally assumed that both the corresponding source signature and the propagation effects are minimum phase (Futterman, 1962; Knopoff, 1964; Sherwood and Trorey, 1965; and Wuenschel, 1965). Due to recording and processing effects, the above assumption is only partly met, and hence the application of minimum phase deconvolution to field data may introduce an undesired phase distortion.

A numerical problem of great importance also arises because of the band-limited nature of the recorded seismogram. Even if the excitation source is truly minimum phase, the calculation of the

phase spectrum from the observed amplitude spectrum requires information from portions of the spectrum which are not available to the processor. In conventional minimum phase deconvolution algorithms, the above problem manifests itself in the form of an ill conditioned autocorrelation matrix whose condition number can be improved by the addition of a "white-noise" constant to its diagonal terms. As expected, the magnitude of the "white noise" parameter is an important factor in the calculation of the desired inverse operator, but it's value can also significantly alter the phase of the residual wavelet.

When a Vibroseis source is considered, there are complexities involving the interaction of the vibrator hydraulics, the baseplate, and the earth's surface. The total effect of this interaction is to introduce an unknown phase distortion onto the observed Klauder wavelet (Frazer, 1983). Furthermore, the conventional processing route which employs minimum phase deconvolution followed by phase correction (Ristow and Jurczyk, 1975), suffers from the same numerical problem discussed previously (see for example Gibson and Larner, 1983).

Finally, given the frequency band limitations imposed by field and processing procedures, we may also encounter 'apparent' phase distortions which are caused by event interference. This type of distortion is extremely troublesome since it may give rise to rapid phase variations across the observed data. For example, let us consider the case of a stack of thin beds with laterally changing thicknesses. If the two-way travel time of the wave through any of

these thin beds is shorter than the time duration of the source signature, arrivals from horizons which are deeper than this stack of thin beds will feature a characteristic signature which may differ substantially from that associated with the shallower events. Furthermore, since the thicknesses of the beds are also changing laterally, the associated 'apparent' phase distortions may create severe interpretation dificulties.

The complications inherent in estimating the phase distortion introduced by the many effects mentioned above mean that the phase of the final interpreter's wavelet is not well determined even when the most careful processing has been carried out. This presents major difficulties for further interpretation and post-stack processing techniques. For example, linear programming spiking deconvolution (Levy and Fullagar, 1981) and acoustic impedance inversion (Oldenburg et al., 1983, and Oldenburg et al., 1984) require that the interpreter's wavelet is zero phase.

The goal of this work is to show how the residual phase of a seismic wavelet may be estimated directly from the data and how the data may then be phase adjusted. We assume at the outset that all of the phase distortions mentioned previously can be modelled by a wavelet whose phase is altered by a frequency independent constant (for further details see Appendix 7-A). This is certainly the correct assumption for modelling supercritical reflections but it is only approximately true for other effects like dispersion which arises from constant Q attenuation (Futterman, 1965; Robinson, 1980(a)). Nevertheless, Levy et al. (1983) have used the constant

phase-shift convolutional model and the Karhunen-Loeve transformation in order to effect phase correction of isolated events exhibiting frequency dependent phase distortions (see Appendix 7-B). The results of their approach were very encouraging so long as the analysed frequency band-width of the signals did not exceed about two and a half octaves. This gives us added confidence that we can apply the constant phase shift model to the work presented here.

In this work we will also adopt the convolutional model for the seismic signals. The residual phase of the seismic wavelet will be estimated by first rotating each seismic signal using a frequency independent phase shift. This rotation will be carried out for a number of phases between $-\pi/2$ and $\pi/2$. The varimax norm of the phase rotated signals is measured, and the trace which exhibits the highest norm value is chosen as the desired phase corrected representation. The varimax norm thus lies at the heart of our computational procedure and the justification for using this norm is presented in the next section.

7.2 METHOD AND EXPLANATORY EXAMPLES

The goal of this section is to develop a method whereby the phase of the residual wavelet can be determined directly from the data. The algorithm to be developed here is based on a model in which the seismogram s(t) is represented by the convolution of a reflectivity function r(t) with a possibly phase shifted zero-phase wavelet $w(\epsilon,t)$, that is,

$$s(t) = r(t) * w(\epsilon,t) \tag{7.1}$$

This is the same model used by Levy and Oldenburg (1981) in their approach for carrying out a deconvolution in the presence of phase shifted signals (see Appendix 7-A). In equation (7.1), $w(\epsilon,t)$ is related to the zero-phase wavelet w(t) by

$$w(\epsilon,t) = \cos\epsilon\, w(t) + \sin\epsilon\, \mathcal{H}[w(t)] \tag{7.2}$$

where $\mathcal{H}[\ ]$ denotes the Hilbert transform.

The form of equations (7.1) and (7.2) is, as we have already discussed in the introduction, a reasonable mathematical model for many of the effects observed on real signals. Let us consider the set of phase shifted replications $w(\epsilon,t)$ shown in Figure 7-1. Our first goal is to find a norm, which when it accepts $w(\epsilon,t)$ as its argument, has an extremum when $\epsilon=0$. That is, the norm is extremized

when it operates on a zero phase wavelet.

The Varimax norm has precisely the properties that we look for. The varimax of the time series $\{s_i\}$ (i=1,N) is defined by

$$V(s) = \frac{\sum_i s_i^4}{(\sum_i s_i^2)^2} \qquad (7.3)$$

This norm was used by Wiggins (1978) to indicate 'spikiness' and it served as the core of his minimum entropy deconvolution algorithm. The maximum value of the varimax for any time series is unity and this occurs when $\{s_i\}$ is a single spike at some arbitrary time sample. On the other hand, the varimax attains a minimum when the series consists of equal amplitude elements at each time sample.

Since a zero-phase wavelet contains the majority of its energy in a relatively narrow time duration (i.e. its major lobe), it is expected that V(w(0,t)) is larger than V(w(ϵ,t)) for $\epsilon \neq 0$. Indeed, a plot of the varimax as a function of ϵ for a Klauder wavelet (Fig. 7-1b) verifies our expectations. We note that V(ϵ) is maximized when $\epsilon=0$, as desired, and that the varimax curve looks very much like a sinusoid. We also note that the period of this sinusoid is 180° and that V(ϵ) is also maximized when $\epsilon=\pi$. This curve indicates a fundamental ambiguity which is evident directly from equation (7.3); the varimax of a time series and of its polarity reversed counterpart are equal. This ambiguity in polarity is something that may have to be corrected at a later stage, after the phase correction has been completed.

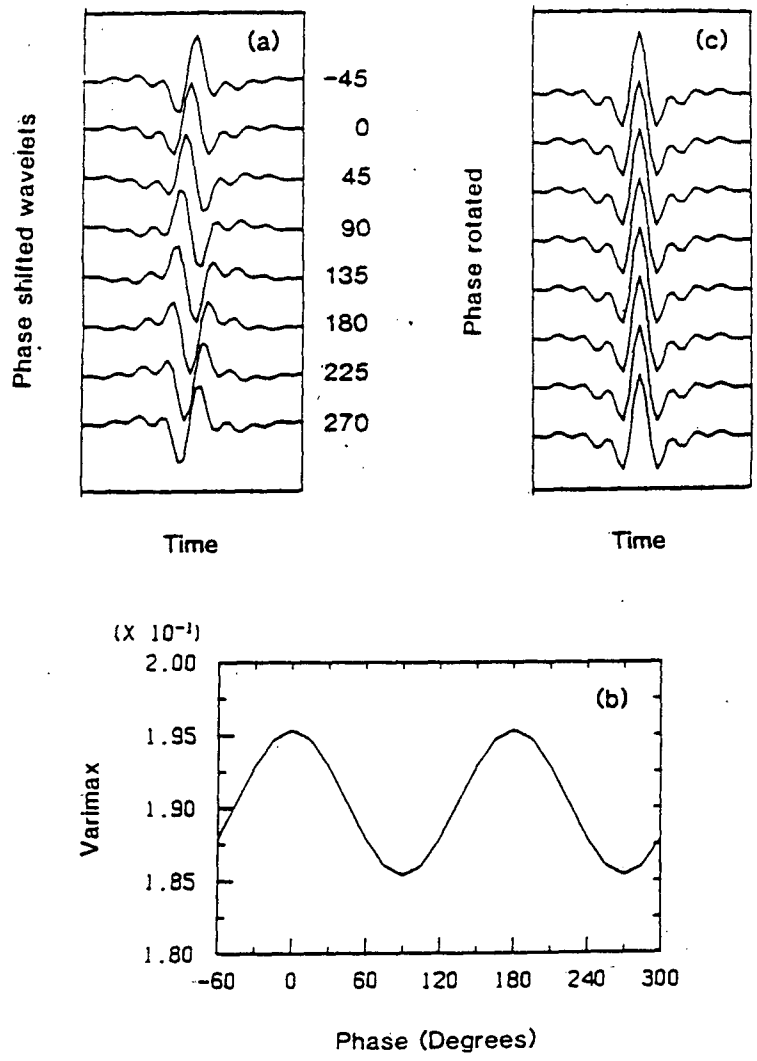

Figure 7-1

In panel (a) a Klauder wavelet has been phase rotated in steps of 45°. The varimax of the rotated wavelets, plotted as a function of phase shift are given in (b). Application of the automatic phase correction algorithm to each of the traces in (a) is shown in (c).

The goal of an automatic phase correction (APC) algorithm is first to estimate the residual phase of each trace and then to perform the desired rotation to zero-phase. To effect this correction, our algorithm operates in the following series of steps:

I. Equations (7.2) and (7.3) are used to compute the varimax $V(\epsilon)$ of the analysed signal for rotation angles ϵ ranging from +90° to -90°.

II. $V(\epsilon)$ is inspected to identify the angle ϵ_{max} which yields the highest value of the varimax.

III. The observed signal is rotated by ϵ_{max} to obtain the phase corrected signal.

IV. For multitrace data the results are inspected and possible corrections for polarities are made.

The results of the application of our algorithm to the set of wavelets shown in Figure 7-1a, are given in Figure 7-1c.

To demonstrate the effects of the band limitation upon the varimax norm measurement we define a quantity S which measures the standout of the varimax peak above the varimax low for the signal being analysed:

$$S = \frac{V_{max} - V_{min}}{V_{min}} \times 100$$

Using this definition we calculate S for a set of sinc functions bandlimited by a trapezoidal filter with corner frequencies f_1, f_2, f_3, and f_4. Typical variations of S are seen in Table 7-1. We notice that the standout is particularly affected by the low frequency cutoff. This is an important observation and it has meant that in doing the varimax calculations on complicated seismic signals we have made considerable effort to keep (f_1, f_2) as low as possible. In those cases where the low frequency cutoff of the seismic signal has been too high, we have first extended the seismic spectrum toward lower frequencies by using the autoregressive approach of Oldenburg et al., (1983) and Ulrych and Walker, (1983) ; see Appendix 6-A. We shall discuss this in further detail later when we consider more complicated signals which have a small varimax standout.

To gain some idea about the applicability of our constant phase model to a more realistic situation, we will consider the wavelet represented by the Z transform $(1.1-Z)^2 x (1.7-Z)^{13}$. Fifteen different wavelets, ranging successively from minimum to maximum phase (delay), have been generated by transferring one zero at a time from the outside to the inside of the unit circle. These wavelets and the corresponding varimax curve are shown in figures 7-2a and 7-2b, respectively. We see that the varimax is maximized for the second wavelet and that this wavelet is a reasonable approximation to a symmetric, that is zero phase wavelet. The estimated phase angle

(f_1, f_2) Hz \ (f_3, f_4) Hz	30-35	40-45	50-55	60-65
1-5	44	53	60	65
5-10	6	15	23	31
10-15	.004	.8	4	10

TABLE 7-1

The varimax standout for the bandlimited sinc function is plotted as a function of (f_1, f_2), the low frequency taper and (f_3, f_4), the high frequency taper. The numbers shown in the table are the varimax peak standouts defined by the equation given in the text.

adjustments required to rotate each trace to zero phase are shown in Fig. 7-2c and the rotated traces are displayed in Fig. 7-2d. It seems, at least for the simple case presented above, that the constant phase-shift approximation did a reasonable job in converting various delay wavelets into an approximate zero-phase representation.

The previous two examples show that the varimax norm can be used to select the zero phase wavelet when the reflectivity function consists of a single spike. The next question to be investigated is whether the approach will give good results when the reflectivity function is more complicated. We know at the outset that for any given source signal, a reflectivity function can be devised to make the method fail. Consider the example offered in Fig. 7-3a. There a zero phase wavelet has been convolved with a dipole reflectivity function to produce a seismogram which looks very much like a 90° phase-shifted wavelet. Application of the varimax norm indicates that this trace should be shifted by 90° to make it zero phase and this phase rotation produces the phase corrected trace shown in Figure 7-3b. The method can therefore fail and it is important to remember this. This single counter example also shows that no mathematics can be developed to prove that our method of using the varimax norm will always produce the correct phase shift. Nevertheless, a single dipole is not a geologically realistic reflectivity function. Geologic reflectivities are much more complex and will often consist of a number of well separated major reflectors in addition to a large number of dipole reflectors having variable distance between the up and down spikes. The cumulative

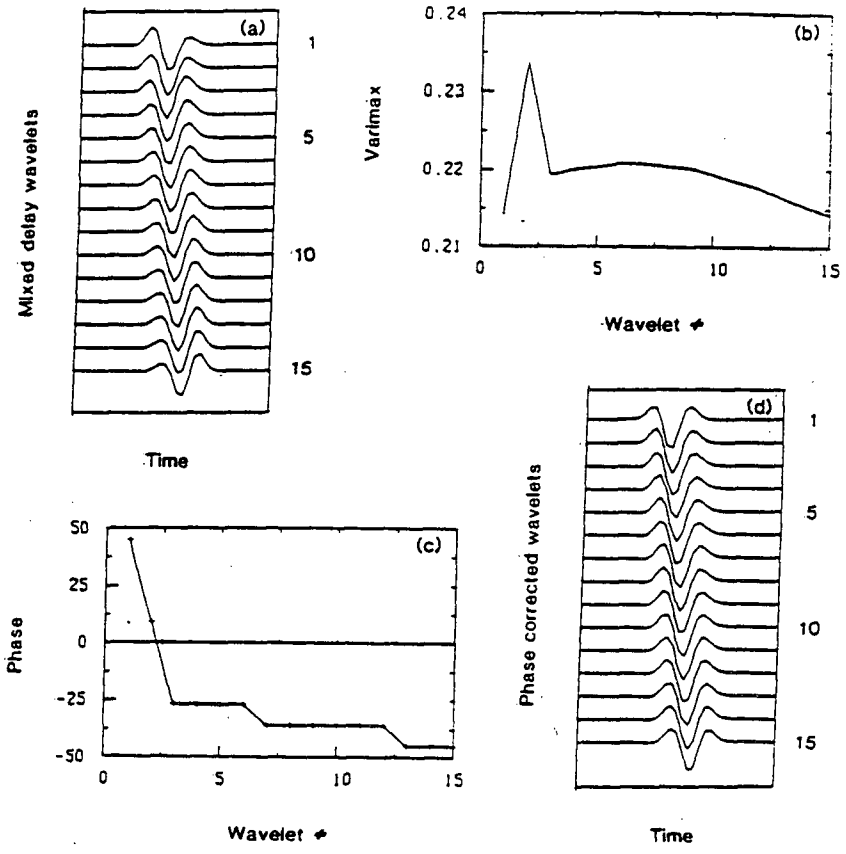

Figure 7-2

Fifteen wavelets having different delay are shown in (a). The varimax of the wavelets in (a) are shown in (b). The phase shifts required to rotate each of the wavelets in (a) so that the varimax is maximized is shown in (c). Panel (d) shows the results of applying the phase shifts given in (c).

effect of the different dipoles would be to control the level of the varimax norm and one would hope that the isolated reflectors would have enough influence on the varimax that they determine the proper phase shift.

To test the reliability of our phase estimation method in a realistic environment we apply the technique to reflectivity functions obtained from well logs. Eight velocity logs used for this test are shown in Fig. 7-4a. The reflectivities corresponding to these logs are shown in Fig. 7-4b. Each reflectivity is then bandpassed and used as input for the APC algorithm. The phase correction returned by the APC algorithm is tabulated in Table 7-2 as a function of the bandpass parameters.

Since the reflectivity function input into the APC program is the true reflectivity convolved with a zero phase wavelet, it would be hoped that the algorithm would have returned a zero value for the phase rotation for all tests. However, rotations of up to 30° do not greatly alter the shape of a wavelet and therefore we shall consider that the algorithm has produced a successful result if $-30° < \epsilon < 30°$. Having adopted this as a criterion of success we can examine Table 7-2 more closely. We notice specifically that for fixed (f_3, f_4), the results in Table 7-2a are generally superior to those in Table 7-2b. This suggests that our phase correction algorithm is heavily dependent on the ratio of the main energy lobe to the side lobes exhibited by the residual wavelet. Thus every effort should be made to maximize this ratio by maintaining the lower frequency components and appropriately shaping the wavelet's amplitude spectrum to avoid excessive side lobes ringing.

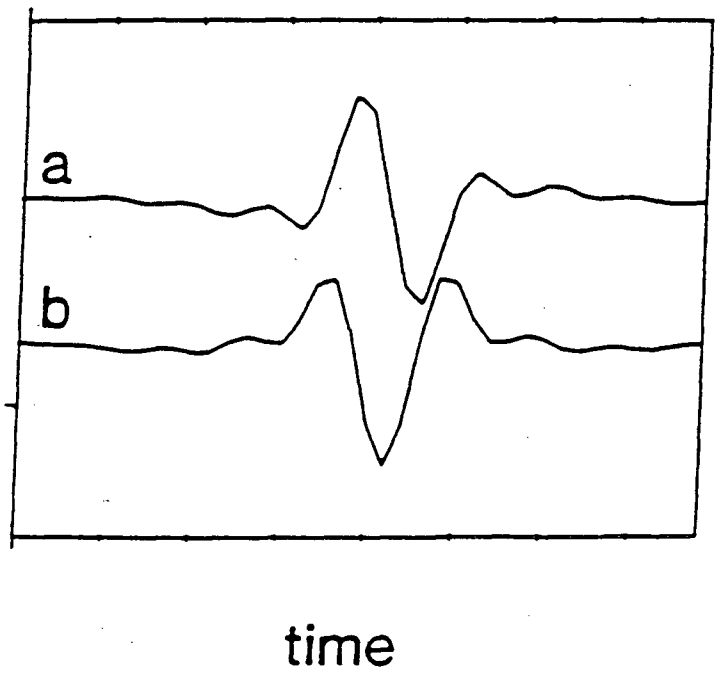

Figure 7-3

Trace (a) is a bandpassed dipole reflectivity. It resembles a 90° wavelet. Application of the automatic phase correction algorithm produces the rotated trace (b).

$(f_1, f_2) = (5, 10)$ Hz

(a)

well # \ (f_3, f_4) Hz	30-35	40-45	50-55	60-65
a	27	0	-27	18
b	54	-63	72	-72
c	45	-27	27	-9
d	-27	18	0	-18
e	63	18	27	9
f	-36	-63	36	18
g	9	9	-27	-36
h	-18	-9	0	-9

$(f_1, f_2) = (10, 15)$ Hz

(b)

well # \ (f_3, f_4) Hz	30-35	40-45	50-55	60-65
a	90	-54	-45	36
b	81	72	81	54
c	-81	45	72	-36
d	-90	45	-18	-18
e	81	9	45	9
f	-81	63	-72	-9
g	27	9	-36	9
h	90	0	27	54

TABLE 7-2

The automatic phase correction algorithm is aplied to each of the reflectivities shown in Fig. 7-4. The reflectivities are first bandpassed with a linear taper extending (f_1, f_2) on the low frequency side and (f_3, f_4) on the high frequency side. The numbers shown in the table are the phase rotations in degrees required to maximize the varimax after the bandpassing.

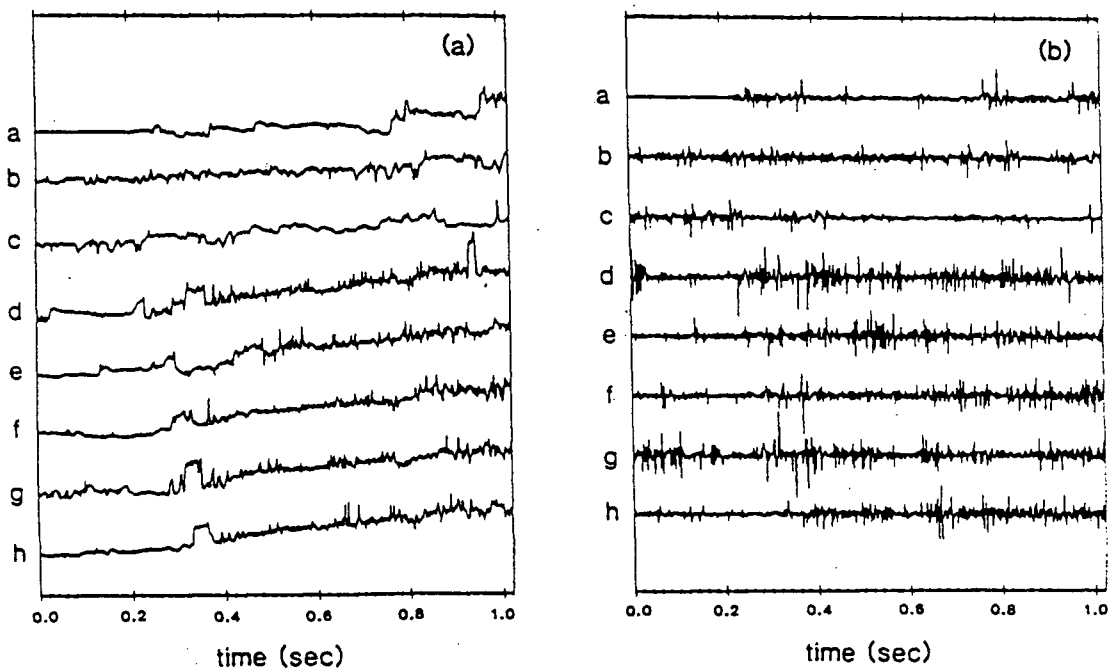

Figure 7-4

Eight velocity logs used to test the automatic phase correction algorithm are shown on the left. The full band reflectivities corresponding to these velocities are shown on the right.

Now let us consider a specific column $(f_3,f_4) = (40,45)$ Hz in Table 7-2a. We notice that the APC algorithm has provided a successful result for 6 of the 8 logs; only reflectivities from logs (b) and (f) would have been adjusted incorrectly. We feel that this is a good success ratio for the APC program. There are some differences in the adjacent columns but the differences are not extreme, except when (f_3,f_4) is reduced to (30,35), a value which is too low and produces too many failures. Such differences with the change in the high frequency filter parameters are expected because of the geologic tuning of the signal. That is, whether a reflectivity dipole looks like a single 90° wavelet or two zero phase wavelets depends upon the separation between the reflectors and the bandpass parameters.

We are very encouraged by these results. The algorithm has proven reliable in the majority of cases providing that low frequencies have been used in the process. We also realize that the success ratio can be increased by using the APC algorithm only in certain types of geologic structures. We know, for instance, that the APC algorithm will fail (generally) if the reflectivity function is Gaussian. In such cases the algorithm has an equal probability of returning a phase shift between -90° and 90°. Returning to Fig. 7-4 we see that log b has a reflectivity function which resembles a Gaussian distribution; this may account for the failure of the APC algorithm to operate upon that reflectivity. We would expect the APC algorithm to work well when the reflectivity is non-Gaussian. This is confirmed by the results in Table 7-2a.

The importance of the low frequency information in applying the varimax criterion has been clearly indicated in the preceding examples. It often happens, however, that the field data are missing information below 10 or 15 Hz. In such cases better results can be expected by first extending the seismic spectrum into the low frequency region by using autoregressive (AR) techniques and then applying the APC algorithm. To use the AR approach we follow the work initially proposed by Oldenburg et al. (1983) and modified by Walker and Ulrych (1983). The low and high frequency cutoffs of the seismic spectrum are first estimated from the data and the spectrum is modelled as an AR process of order p. The Yule-Walker algorithm is used to evaluate the AR filter coefficients and the constructed filter is then used to predict the missing low frequency values.

The benefits of using the AR frequency extension are shown in the next example. We have taken the reflectivities in Fig. 7-4 and bandpassed them with the trapezoid filter. The low frequency parameters for the trapezoid were always $(f_1,f_2) = (10,15)$ Hz but the high frequency values (f_3,f_4) were variable. After each bandpassing we used the frequency band (f_2,f_3) to generate the spectral values at frequencies smaller than f_2. The results from the APC algorithm when information 5-10 Hz was used and when information 1-5 Hz was used are shown in Table 7-3. We see that the success ratio is very good, expecially for Table 7-3b.

Although our algorithm seems to yield reasonably reliable results, it is recommended that, whenever possible, a test trial on a well-log synthetic reflectivity should be made prior to the

$(f_1,f_2) = (5,10)$Hz

(5-10)Hz	30-35	40-45	50-55	60-65
a	-27	-9	-18	-18
b	81	72	-18	-18
c	18	-81	18	-9
d	45	9	-18	-27
e	-63	-36	45	-9
f	-9	9	-36	9
g	0	9	72	54
h	54	9	9	9

$(f_1,f_2) = (1,5)$Hz

(5-10)Hz	30-35	40-45	50-55	60-65
a	-18	-18	-54	9
b	63	-18	-9	-9
c	18	-90	9	-9
d	36	9	-9	-18
e	0	-27	27	-9
f	-9	0	-27	9
g	0	9	63	36
h	36	-9	0	0

TABLE 7-3

The automatic phase correction algorithm is aplied to each of the reflectivities shown in Fig. 7-4. The reflectivities are first bandpassed with a linear taper extending (10,15)Hz on the low frequency side and (f_3,f_4) on the high frequency side. Using the AR algorithm we have extended the frequency information band $(15,f_3)$Hz into the low frequency portion of the spectrum and then bandpassed the result as indicated by the corner frequencies (f_1,f_2) and (f_3,f_4). The numbers shown in the table are the phase rotations required to maximize the varimax after the bandpassing.

application of the algorithm to a given set of data. This test should establish the reliability of the phase correction operation for the given zone of interest. Additionally, if the correction angle estimated from the well-log synthetic differs largely from 0°, it may be prudent to follow the APC algorithm run by the application of a single phase correction to the whole section so that the final result will conform with the well-log information.

Before we proceed to some practical considerations and real data cases, we would like to present one more idea. If we consider the example summarized in Figure 7-2 as representative of a large number of cases, it seems that our algorithm opens the door for an additional approach to signature deconvolution. The target of signature deconvolution schemes is to recover a bandlimited zero phase representation of the reflectivity function. Let the seismogram be

$$s(t) = r(t) * w(t) \tag{7.4}$$

where $r(t)$ is the true reflectivity and $w(t)$ is a seismic wavelet. Taking the Fourier transform of (7.4) leads to

$$S(\omega) = R(\omega)\ W(\omega)$$

In most cases the amplitude spectrum $|W(\omega)|$ of the wavelet can be reliably determined but its phase spectrum $\phi(\omega)$ cannot. The work in Fig. 7-2 however shows that the effects of $\phi(\omega)$ can approximately be compensated for by applying a frequency independent constant phase

adjustment. That is, for any of the mixed delay wavelet, there exists a phase shift ϵ such that

$$\mathcal{F}^{-1}\{ W(\omega) \exp[i\phi(\omega)] \exp[\pm i\epsilon] \} \qquad (7.5)$$

is aproximately a zero phase signal. ($\mathcal{F}^{-1}$ denotes the inverse Fourier transform). In equation (7.5) the + sign is taken for positive frequencies and the - sign for negative frequencies. We now suggest that signature deconvolution can be carried out using two successive independent operations. In the first step we whiten the reflectivity spectrum by dividing the spectrum of the seismogram by the amplitude spectrum of the estimated wavelet. We then attempt to nullify the effects of the wavelet's phase spectrum using the operator $\exp[i\epsilon]$. Our final result will be

$$\frac{S(\omega) \exp[\pm i\epsilon]}{|W(\omega)|} = R(\omega) \exp[i(\phi(\omega)\pm\epsilon)] \approx R(\omega)$$

The inverse Fourier transform of this function will yield a reflectivity series representing (approximately) the convolution of the true reflectivity series with a zero-phase residual wavelet.

To demonstrate this deconvolution approach we use the following example. The mixed delay wavelet of Figure 7-5b is convolved with the reflectivity function of Figure 7-5a to yield the input seismogram shown in Figure 7-5d. Dividing the spectrum of the input seismogram by the amplitude spectrum of the wavelet (weighted by a 5% water level parameter) and inverse Fourier transforming the

result, yields the trace of Figure 7-5e. Application of the phase-correction algorithm to the latter gave the final deconvolved output which is shown in Figure 7-5f. Comparison of this result with the band-limited reflectivity function (Figure 7-5c) shows that this deconvolution route can yield the desired solution. Considering the difficulties so often associated with the estimation of the wavelet's phase spectrum it seems that the proposed deconvolution route offers an attractive alternative to conventional methods.

7.3 REAL DATA EXAMPLES

In applying the phase correction procedure to real data sets we want to enhance the ability for the algorithm to produce correct results. We outline below a number of steps which are designed to increase the success ratio of the proposed algorithm.

I. If low frequency information is missing, the spectrum of the data should be extended into the range (5-10 Hz) using the AR prediction scheme.

II. To avoid end effects, the data should be tapered prior to the application of the APC algorithm.

III. To avoid inconsistent phase rotations which may arise due to large lateral variability of the processed data, the algorithm should determine the appropriate phase correction via the analysis of successive groups of seismograms. The number of traces in each

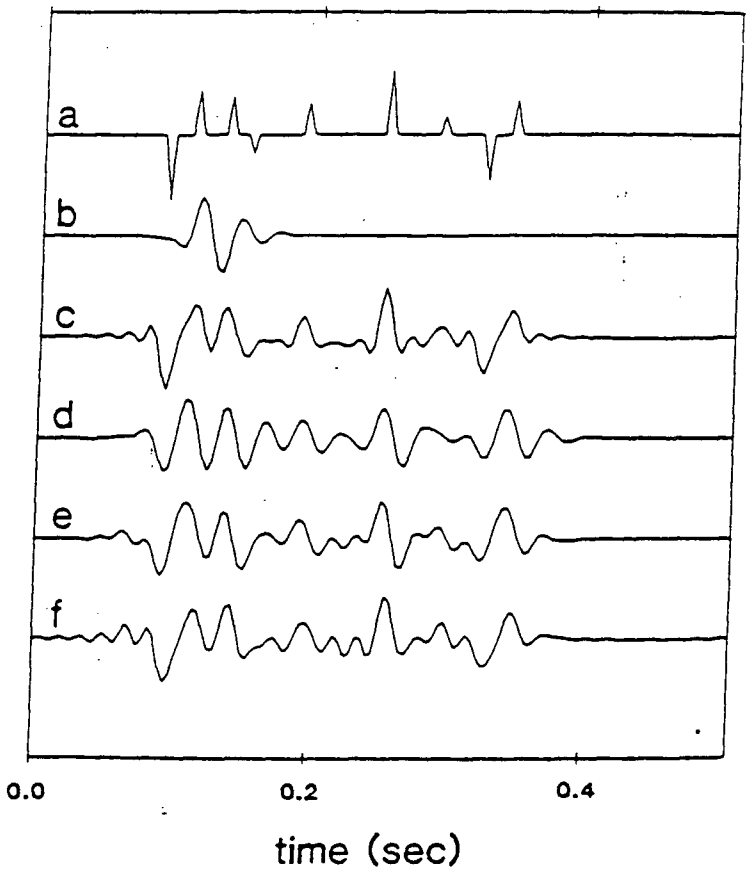

Figure 7-5

The work summarized by Figure 7-2 suggests that zero phase deconvolution followed by a phase correction may provide an alternate way of carrying out signature deconvolution. The true reflectivity function is shown in (a) and a mixed delay wavelet is given in (b). The bandpassed reflectivity function is shown in (c). The seismogram in (d) has undergone zero phase deconvolution by dividing its spectrum by the spectrum of the wavelet in (b). The result of this deconvolution is shown in (e). Application of the phase correction algorithm yields the final result in (f); it may be compared directly with the bandpassed reflectivity in (c).

analysed group depends on the variability exhibited by the data. As a rule, the number of traces in an analysed group should not be smaller than ten or twenty. If it is felt that the lateral variability of the estimated phases is too large, then the APC algorithm should be rerun using a larger number of seismograms in each group.

IV. The estimated phase corrections should be smoothly interpolated so that each trace can be assigned a phase shift. In addition, it may be necessary to correct for the polarity to conserve trace-to-trace true polarity relations.

V. To avoid smoothing effects due to source signature time dependency, the analysed time window for the phase correction algorithm should be centered around the zone of interest. It is important to remember that the phase correction which is suitable for a given time window may perform poorly outside this window. Our experience suggests that the analysed time window should not be shorter than about 500 milliseconds nor longer than about 1.0 second.

VI. When well-log information is available, the algorithm should be applied to the band-limited synthetic reflectivity function to determine the phase angle ϵ_{well}. If ϵ_{well} differs largely from 0°, the output from the phase correction algorithm should be further rotated by $-\epsilon_{well}$ degrees.

VII. The algorithm should not be applied to time sections in which the geologic reflectivity is approximately Gaussian.

Having specified these practical considerations we shall now turn to the real data examples. As with many other processing techniques, the goal of our newly developed algorithm is to improve the interpretability of the given seismic section. To show that this goal can be achieved we will recover the logarithm of the relative impedance function (Oldenburg et al. 1983) of a CMP stacked section both before and after phase correction. The success of the APC algorithm will be shown by comparing the recovered relative impedance functions to a velocity log measured at a well site slightly off the processed line.

The data of Figure 7-6a constitute the output of a conventional processing sequence. We have further applied a post-stack zero-phase deconvolution to yield the results in Figure 7-6b. Those data were input into the APC algorithm to produce the results shown in Figure 7-6c. The unconstrained (no external well-log or stacking velocity constraints applied) linear programming acoustic impedance inversion algorithm was applied to the data in figures 7-6b and 7-6c and the results for twenty consecutive traces near the well are shown in Figure 7-7. The impedance traces to the right of the well-log correspond to the phase corrected data ($\epsilon \approx 80°$) while those those to the left correspond to the uncorrected data. Obviously, the application of the phase correction algorithm to this data resulted in a fairly good match between the well-log and the recovered relative impedance functions. Furthermore, comparison of the faulted zone (traces 50 to 70, between 1.6 to 2.0 seconds) in figures 7-6a, b, and c, shows a better fault definition on the phase corrected output. To complete this example we show in Figure 7-8 the result of

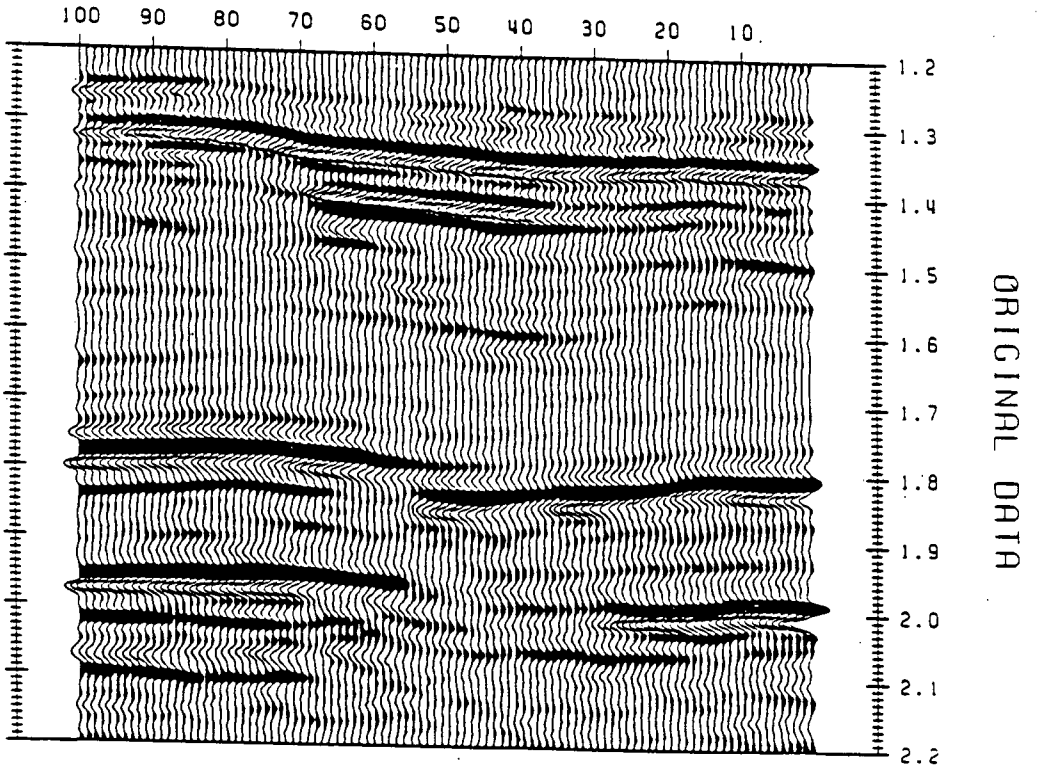

Figure 7-6a

CMP seismograms representing the output of a standard processing sequence.

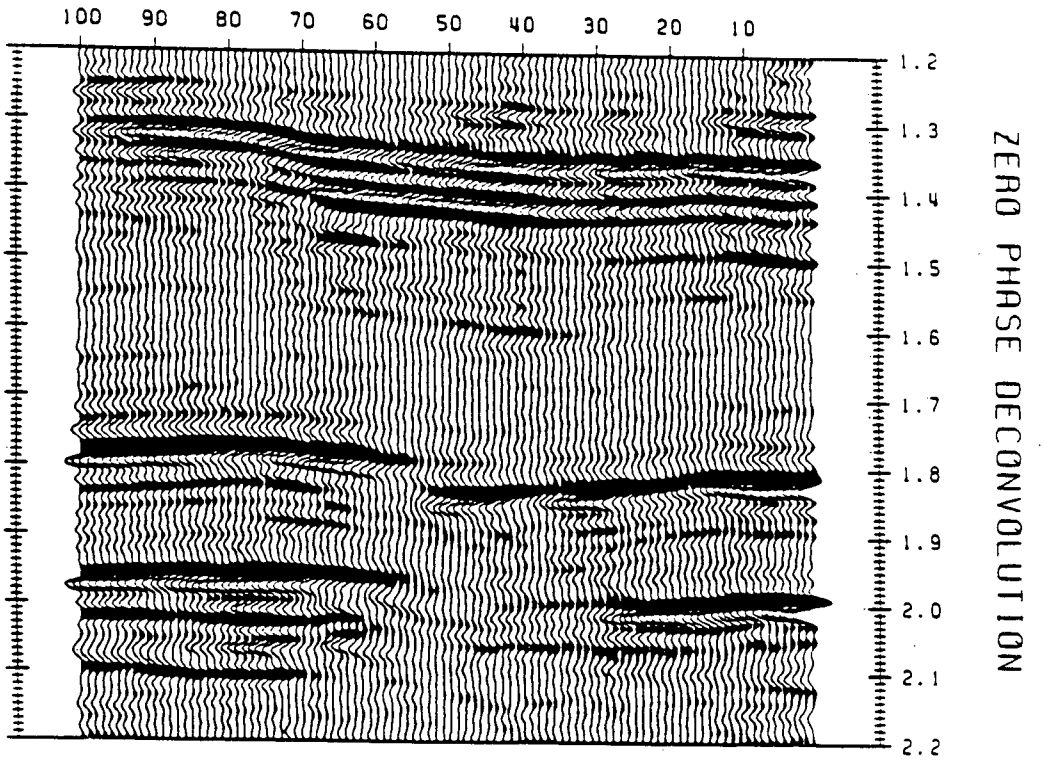

Figure 7-6b

The data of Fig. 7-6a after zero-phase deconvolution.

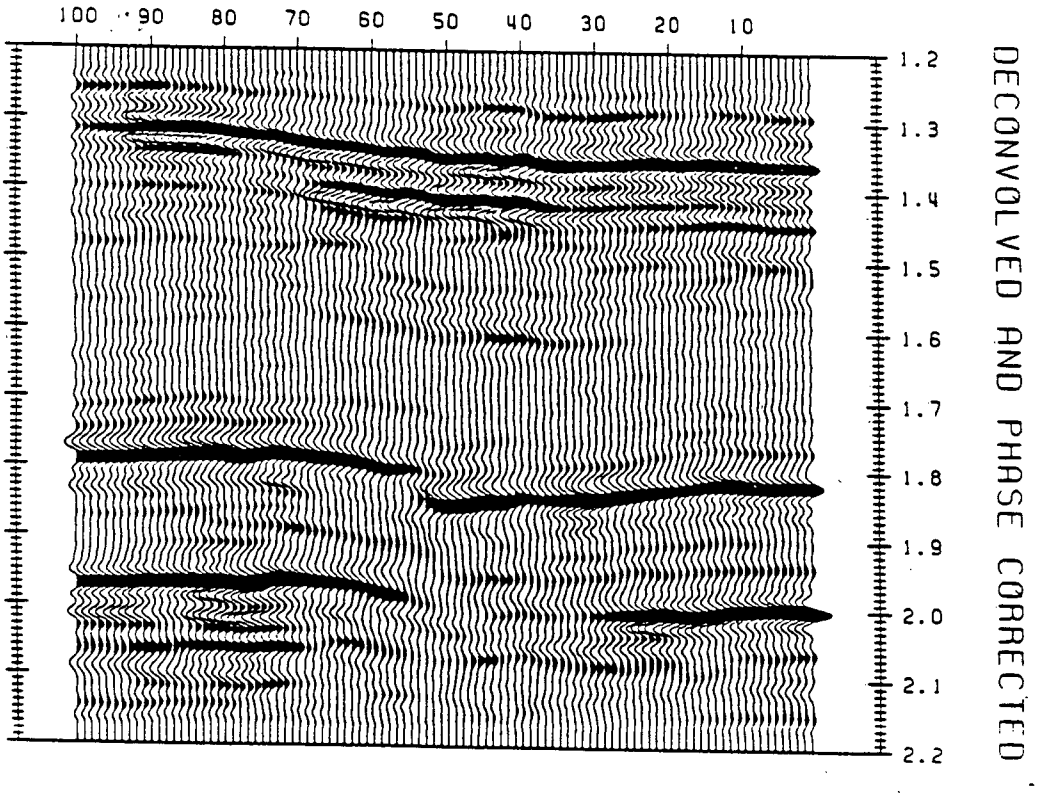

Figure 7-6c

Application of the APC algorithm to the data shown in Fig. 7-6b produced the phase-corrected data shown in this figure. Successive groups of 10 traces were analysed for the whole data set and all phase corrections were close to 90°.

the unconstrained linear programming algorithm applied to the complete data set of Figure 7-6c. We have overlayed the recovered reflectivity on the grey shaded relative impedance functions. The consistent behaviour of these functions after the application of the phase correction is very noticeable.

7.4 CONCLUDING COMMENTS

In this chapter we have put forth a method for estimating the residual phase of the seismic wavelet. The combined use of the varimax norm and the concept of a constant phase rotation permits us to estimate this phase directly from the data. The method is not guaranteed to work in every instance but work done with acquired velocity logs shows that the method should work in the majority of cases. Moreover, modifications such as extending the frequency band of the spectrum using autoregressive techniques, selecting particular geologic environments in which to use the algorithm, and applying the algorithm to groups of seismic traces, will increase the chances for success. Our work with this algorithm to date has been very promising, and we now apply the APC algorithm on a routine basis to conventionally processed data. In a great may cases, we find that the interpretability of the section is improved and we also find better agreement with well logs when the inversion is carried out on phase corrected data.

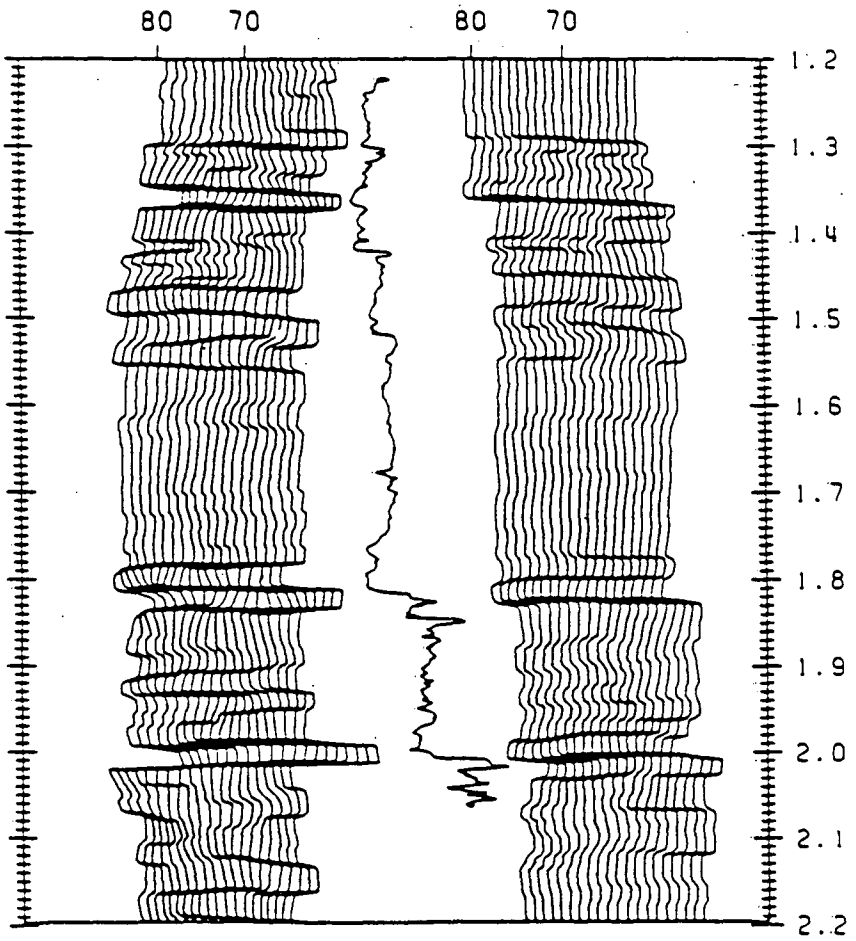

Figure 7-7

The relative acoustic impedance shown on the left has been obtained by inverting twenty seismograms near trace #70 in Figure 7-6a. These results do not compare favourably with the velocity log plotted in the center of the diagram. The relative acoustic impedance obtained by inverting the phase corrected data in Figure 7-6c is shown on the right side of this figure.

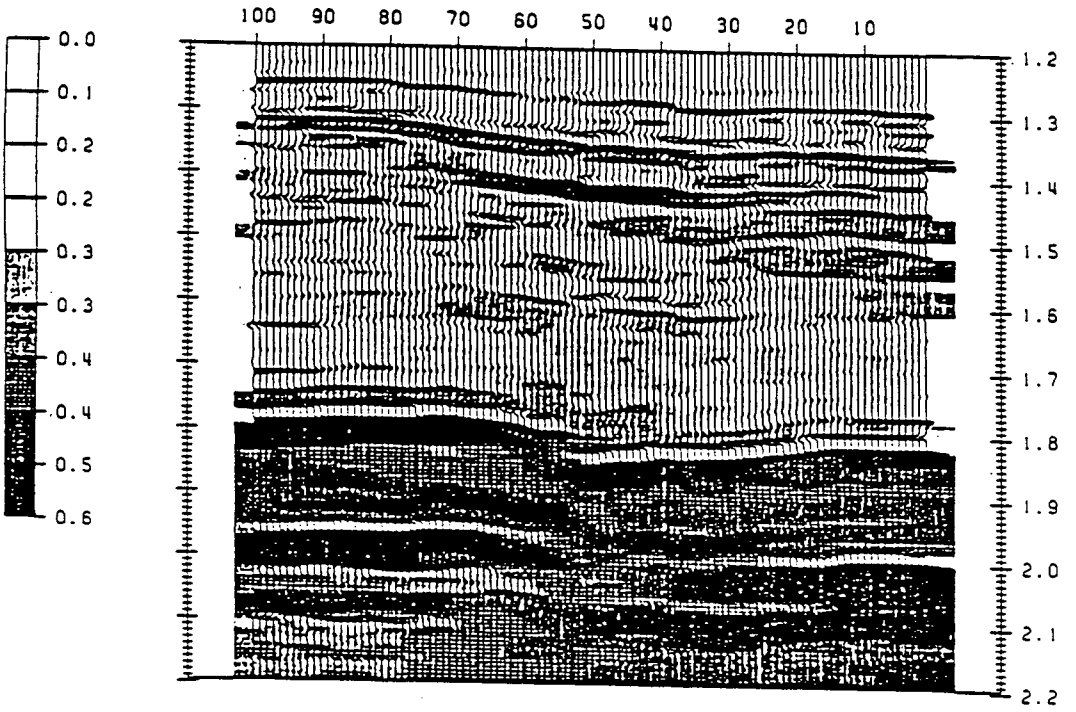

Figure 7-8

The linear programming reflectivities obtained from the phase corrected data in Figure 7-6c are shown in this figure. They are overlaid with the grey shade of the relative acoustic impedance.

CHAPTER VIII: SUMMARY

It is the irony of the subject of this work that at its conclusion I still have to say that all the preceding material may not be sufficient for practical implementation of the inversion scheme. Indeed, a number of steps are required if bandlimited seismic data are to be successfully inverted to yield a full band acoustic impedance. Each is important and failure of any step can result in a degraded end product. In the following I will outline in step wise form some considerations and operations which when followed will enhance the likelihood of success for the complete inversion.

STEP 1: Preinversion Processing

The processing sequence applied to seismic data prior to impedance inversion will have important effects on the outcome of the inversion. Of particular importance are those processes which affect the relative amplitudes of the reflectors, the effective bandwidth of the seismogram, and the phase of the residual source signal.

It is generally impossible to obtain true amplitude sections without 'a priori' knowledge of the subsurface geology. Since this information is not usually available, one should do his best using

programmed gain control with the hope that subsequent incorporation of well-log information and stacking velocity information into the inversion will overcome any amplitude discrepancies present in the data. It is recommended that AGC with short window lengths not be applied to the data.

In many cases, lateral energy balancing of the data is required. A module which normalizes trace amplitudes should be applied to produce a balanced section, that is, one in which the energy or the sum of the absolute values of each of the seismograms is normalized to a given constant. If this is not done and the section is unbalanced then it is likely that the constructed impedance section will display an apparent decrease in lateral continuity.

The input to the acoustic impedance inversion algorithms is assumed to be a bandlimited representation of the true reflectivity. Therefore routine processes like spiking deconvolution and gap-deconvolution which are applied to the data in order to whiten the trace spectrum and eliminate short to medium period multiples are required prior to impedance inversion runs. Some caution is recommended when gap-deconvolution is applied to the data because this process may introduce a phase shift into the seismogram. In Chapter VII we showed how this phase shift may be recovered and how to apply the corresponding correction to the seismic section.

It is important to remember that the goal of preinversion processing is a stacked section in which: (a) multiples are largely attenuated, (b) the effects of the wavelet within the frequency

information band have been removed to our best ability, and (c) relative amplitude relations are approximately correct. That is, the observed seismograms are a reasonable band-limited representation of the primary reflectivity function.

STEP 2: Section Polarity Correction

In some instances there is doubt about the true polarity of the seismic section. Such ambiguity may be the result of field procedures or due to subsequent processing (for example minimum phase deconvolution followed by phase correction applied to Vibroseis data). If this is the case, determination of the correct polarity is an essential step which should precede the impedance inversion. Polarity determination can be accomplished to a certain extent using the results of an unconstrained impedance inversion run. We distinguish the following cases:

A. Well log information is available

(i) When there is correlation between some reflectors on the stacked section and corresponding events on the well-log synthetic reflectivity, then direct comparison of these events may be used to determine the correct polarity.

(ii) If direct correlation is not available (that is, the synthetic well-log reflectivity does not match the near-well stacked seismograms), an unconstrained impedance inversion should be executed. The polarity of the section

may be estimated from the general behavior of the pseudo-impedance log (i.e. general rise within some given time windows which match (correct polarity) or mirror image (reverse polarity) the well-log impedance). Due to the nature of the inversion algorithms (the solutions are minimum structure representations of subsurface geology), AREAS OF sharp changes in impedance on the well-log are more likely to be correctly reconstructed. These areas are preferable for the purpose of polarity determination.

B. Well log information is not available

In this case the information contained in the stacking velocities should be used. Stacking velocities are picked and inverted using the Dix formula or one of the velocity inversion algorithms outlined in Chapter IV. The constructed velocity profile is used in conjunction with the pseudo-impedance log estimated by an unconstrained impedance inversion of the data. The polarity is estimated by comparing the general behavior of the two profiles within chosen time windows.

The user is cautioned that an interpreter's wavelet which contains a large residual phase may severely inhibit the success of the methods discussed here.

STEP 3: Section Phase Correction

The inversion algorithms proposed in this work, assume that the interpreter's wavelet, (or residual wavelet) is zero-phase. In many cases this assumption is invalid and a correction to the wavelet phase is required.

For this correction, we adopt the constant phase shift model in which we approximate the residual phase of the wavelet by a frequency independent phase shift. This correction consists of converting the observed seismogram $x(t)$ into an analytical signal $x(t)$, and then multiplying $x(t)$ by the factor $\exp[i\epsilon]$ with ϵ being the correction phase angle. The phase corrected trace is recovered by taking the real part of this final quantity (See Chapter VII). Our experience shows that (with appropriate choice of ϵ) this operation satisfactorily corrects the phase and that the subsequent impedance inversion yields markedly better results.

The determination of the 'correct' shift angle should be based on the results of the unconstrained impedance inversion and information contained in either the well-log or in the stacking velocities, in the manner described below:

A. Well log information is available

(I). When well-log impedance or velocity is available, efforts should be concentrated on a window which contains a large impedance discontinuity (both the AR and LP algorithms are best suited for the detection of this type of impedance structure). Successive rotation of the near-well stacked traces by a number of shift angles (say = -90°, -60°, -30°, +30°, and +60°) followed by impedance inversion will yield a set of pseudo-impedance curves. These are then compared to the well-log impedance, and the trace which produces the best match is used to determine the correction angle. It is important to realize that polarity uncertainty may still exist after the application of this analysis, but this uncertainty can be resolved by inspecting the set of pseudo-impedance profiles produced by an unconstrained inversion run.

(II). If no distinct impedance discontinuity is present on the given well-log, the operation described in (i) above is performed on some arbitrary data window. This time, however, the choice of the correction is based on the comparison of the general behavior of the pseudo-impedance profiles and the well-log impedance in the chosen window. Experience has shown that the results of the analysis for this type of information are less reliable and must be applied with caution.

B. No well-log information is available

In this case the results of the unconstrained impedance inversion algorithms applied to the phase corrected traces are compared to the velocity curve obtained from the Dix formula or from the inversion of stacking velocities using algorithms outlined in Chapter IV. Again however, these results are not completely reliable and the technique must be applied with caution.

C. Automatic Phase Correction

The procedure outlined in Chapter VII has proved successful in a large number of examples. However, it is quite conceivable that this scheme will fail in some geological environments. Consequently, it is always recommended to compare the results of an unconstrained inversion run on the phase corrected section to the available well-log and stacking velocity information. If any doubt as to correctness of the applied phase remains, it is recommended to use the uncorrected data in the ensuing inversion.

STEP 4: Improving Signal to Noise Ratio

When the quality of the stacked section is low, impedance inversion algorithms which operate directly on these data are not likely to produce reliable results. In such cases poor quality output might be expected even when the inversion is done by incorporating external information from well-logs and stacking velocities. An improvement in the signal to noise ratio in the observed stacked section can add significantly to the final quality of results. Trace mixing is the simplest scheme for signal to noise ratio improvement. However, mixing results in a loss of lateral resolution which may obscure some features of interest.

An alternate approach is based on principal component analysis as outlined in Appendix 7-B. Here we search for the most correlatable (similar) component in a set of 'n' successive traces (generally n = 3 is sufficient). This method deteriorates to a straight stack if the signals are uncorrelated but it will achieve a somewhat better signal to noise ratio, accompanied by a somewhat smaller loss of lateral resolution, otherwise.

STEP 5: Determining the 'Reliable Frequency Bandwidth'

The basic assumption made in the inversion algorithms described here is that the section to be inverted consists of a bandlimited representation of the reflectivity function. The LP algorithm attempts to construct a full band reflectivity whose spectrum is consistent with the data within the information band. It is therefore important that the width of this frequency band be reliably determined.

In determining the reliable frequency band one should use the following guide-lines:

(a) The results of the impedance inversion algorithms are more certain and exhibit higher resolution when the algorithms use a wider frequency bandwidth.

(b) Earth attenuation causes a severe loss of energy at the higher frequencies with the result that the amount of energy that returns to the receivers at these frequencies for 'large' arrival times is small. If this energy is comparable in magnitude to that of the background noise, the information contained in these frequencies is not reliable and should not be used in the inversion.

The actual determination of the endpoints of the reliable frequency band (FLO, FHI) is based upon inspection of a set of amplitude spectra corresponding to arbitrarily selected traces from across the section. The processor should note the band of

frequencies at which relatively high energy is concentrated and the level of noise at those frequencies which are outside the frequency band of the source. The upper limit of the reliable frequency band is the highest frequency of this band at which energy is about twice the noise level. The lower limit can be computed likewise, but one is cautioned not to set the lower limit less than about 8 Hz because the reliability of the phase below this frequency is rather poor.

STEP 6: Unconstrained Inversion

In the absence of any additional information, the inversion algorithm can operate on the information included in the stacked section alone. In this case, the reflectivity obtained from the algorithms represents a good deconvolution of the stacked section, and can be safely used as such. However, the pseudo-impedance section obtained from this inversion carries at best relative information (as it represents only the logarithm of the ratio of the impedance at time 't' to that at the top of the section). This information may be correct if the geology of the area does not contain many regions where the impedance is a slowly changing function of depth. Generally, however, this impedance estimate has a lower reliability than that produced from a constrained impedance inversion run. Moreover, because the information available is not sufficient for proper scaling of the stacked section, subsequent conversion of the pseudo-impedance into impedance or pseudo-velocity is not likely to produce physically meaningful information concerning formation characteristics.

STEP 7: Scaling The Data

When constraints are used, it is important that the data are properly scaled. The primary reason is that both point velocity constraints and stacking velocity constraints require that the sum of the reflection coefficients obtained in the inversion will attain some desired value to within a determined error. In order for the sum to be physically meaningful it is necessary that the data are properly scaled. The magnitude of the reflection coefficients obtained from the unconstrained inversion run provide an immediate indication about the necessity to scale the data. For instance, reflection coefficients larger than unity are not physically reasonable. Similarly, reflection coefficients of magnitude 0.5 in an area where the reflection coefficient should be in the order of 0.05 indicate that the data should be rescaled. To avoid such instances we recommend that considerable effort be spent in scaling the data prior to an inversion run.

The procedures suggested here are quite subjective and are largely dependent on the geological intuition possessed by the processor. We distinguish two cases:

A. Well-log information is available

The simplest and most straight forward method is to compare the size of the reflection coefficients obtained from the unconstrained inversion to those observed in the well-log reflectivity. The scaling factor obtained from this comparison is that number which will scale the constructed reflectivity so that its reflection

coefficients are comparable to those of the well-log reflectivity. The user is reminded to use the same frequency information band in the unconstrained run as he will when he runs the constrained version.

Once an approximate scaling factor has been determined, it is recommended that the constrained inversion algorithm be run on small sets of scaled data. One should now inspect the computed impedance or velocity estimates to verify that these estimates are geologically reasonable. If they are not, further adjustment of the scale should be made on the basis of this inspection. If the processor is satisfied, the whole section may be scaled and the constrained run can be submitted.

B. Automatic scaling

The technique outlined in Chapter VI has proved successful in a number of cases. However, residual phase and severe relative amplitude discrepancies may cause its failure. It is then recommended that this scheme be used only when the log relative impedance from an unconstrained run exhibits a reasonable match with the well-log or the velocity profile obtained from the inversion of the stacking velocities.

Step 8: Well-log Constraints

Point velocity constraints can be used in the inversion when well-log information is available and a reasonable tie is established between this information and either the observed stacked section or the reflectivity output from an unconstrained inversion. The format of the constraints includes the time of the constraint, the estimated velocity and a corresponding estimate of the uncertainty in the velocity.

Step 9: Stacking Velocity Constraints

Stacking velocities are always available for use in constraining the impedance inversion, but their applicability to this inversion may decrease considerably in regions of complex geology. If it is possible to utilize them, their information supplies additional controls on the low-frequency trends in the recovered impedance.

To derive information from the stacking velocities we assume that to good approximation they are in fact RMS velocities. Thus, from the stacking velocities we can get averages of the velocity over selected time windows.

Velocity analysis, continuous velocity analysis maps, or constant velocity stacks can all be used for selecting stacking velocities. However, the picking of stacking velocities with the corresponding times and the associated uncertainty values is most easily performed on a contour velocity analysis plot. One should

select as many reasonable stacking velocities as possible, particularly in those time windows where the stacked section indicates major structural changes.

Velocity constraints (if available) should be used along with the stacking velocities in the velocity inversion. The final constructed model then incorporates all of the available velocity information. The velocity inversion algorithms (described in Chapter IV) offer important advantages in both stability and approach over other one dimensional schemes. Out of all possible velocity models which fit the data, these algorithms seek that solution which exhibits the smallest amount of change as a function of time (depth). This results generally in a smooth version of the true structure. The correctness of the low frequency features in this model is further ensured by the addition of point velocity constraints (from well-log information) when available.

Stability is achieved by not requiring that the solution fit the data exactly, but rather allowing it to misfit in accordance with the supplied errors.

The RMS inversion followed by an appropriate interpolation generates an interval velocity profile at each CDP location which is a smooth estimate of the true velocity profile. In using this velocity model to constrain the impedance inversion, we must remember that it is similar to the true velocity only in terms of averages over certain time windows. This prescribes the form of the

constraint utilized by the impedance algorithm. The average value of the impedance change across a specified time window is constrained to be that calculated from the input interval velocity, to within a given misfit (see Chapter IV).

One is cautioned again that the reliability of the constructed interval velocity curves depends on the quality of the velocity analysis maps and the deviation of the local geology from the horizontally layered earth model (which is assumed in the conversion from stacking to interval velocity profiles). In areas where steeply dipping events are present, the estimated velocity curves may exhibit prohibitively large errors.

Step 10: Principal Component Analysis and Low Frequencies Mixing.

In order to increase the reliability and enhance the presentation of the results, we recommend that principal component analysis will be applied to the final reflectivity section produced by the inversion. This operation (which has been described previously) should be applied to the reflectivity section prior to plotting. Its application will increase considerably the signal to noise ratio of the reflectivity section and result in only a small loss of lateral resolution.

Due to the inherent non-uniqueness in the acoustic impedance

inversion problem, it is necessary to mix the predicted low frequencies, that is, to average those frequencies generated by the inversion algorithm which are smaller than 'FLO' (the lower limit of the information band). This mixing operates on the premise that the very low frequencies (say 0-1.5 Hz) should exhibit only a very small change across the section and hence the information about the reflectivity contained in those frequencies is averaged over a large number of traces. Conversely, for frequencies close to 'FLO' only the information contained in a small number of successive traces is mixed. This permits lateral variability to occur. Between these two extremes, the number of traces used in the mixing decreases rapidly by a rule which behaves approximately as the inverse frequency (1/f).

STEP 11: Conversion of Full-band Reflectivity to Pseudo-Velocity or Pseudo-Impedance

The output of the acoustic impedance inversion algorithms is a set of 'full-band' reflectivity functions which satisfy all constraints imposed during the inversion, to within the prespecified errors. That is, the reflectivity function has a spectrum which matches the spectrum of the input seismograms within the information band, and it also satisfies well-log velocity constraints and stacking velocity constraints if they were imposed. Conversion of the full band reflectivities into velocity or impedance is carried out by exponentiating the partial sums of the reflectivities and then multiplying them by the starting velocity at each CDP location.

STEP 12: Displaying Impedance Sections

Presentation of impedance sections depends largely on the type of information desired. When the goal of the interpreter is to delineate geological formations with the associated relative impedance information, a simple line plot seems to offer a useful presentation. This type of presentation is particularly advantageous since the interpreter's eye will tend to follow impedance discontinuities and not be affected adversely by small trace to trace impedance variations.

If the interpreter wishes to assign a velocity or impedance value to the formation of interest, color or grey shades constitute a better form of presentation. When such a presentation is desired, the choice of the number of color levels and their actual values is of paramount importance. A poor choice of these parameters may cause a significant decrease in the observed resolution of the presented impedance. It is recommended that the number of color levels be chosen such that the interpreter can recognize easily any transition from one velocity/impedance level to another. Choosing too many color levels allows subtle transitions from one color level to another, thereby obscuring small targets of economic importance. Furthermore, although it may seem desirable to assign an arbitrary velocity/impedance value to each color level so that the total number of colors will cover the range of the expected velocity values in a linear (equi-spaced) fashion, this coloring scheme is strongly not recommended. This scheme will cause a severe loss in resolution (reduction in the number of active color levels) in any

geological environment which includes a small number of very low and very high impedance formations embedded in a set of formations characterized by medium impedance values. A better choice of levels is one which assigns values to color levels so that each color level represents about the same number of picture cells (a picture cell is a portion of the impedance picture defined by the time and the space sampling intervals). This approach ensures that all the available colors will be active in the coloring process and thereby yield a better apparent reslution than that offered by the linear coloring scheme.

Finally, the results of an inversion run executed with the full set of steps discussed previously is presented in the folded data set marked as Line C. These data have been acquired in Alberta and feature a number of exploration targets in the time window 0.5 to 0.7 seconds. The processed result presented here depicts the full-band reflectivity functions overlayed by the pseudo-velocities calculated from these reflectivities using the assumption of constant density. Details which are not easily deciphered from the stacked section are clearly observed on the final inversion result. In particular, lateral variations in formation velocity are clearly visible even though only nine grey shade levels representing velocity in kilometers/seconds are displayed. Comparison of the calculated pseudo-velocities with sonic log information (not available during the inversion process) revealed excellent

agreement.

Past experience with the process described in this work has shown that careful utilization of the presented algorithms generally yields highly reliable results.

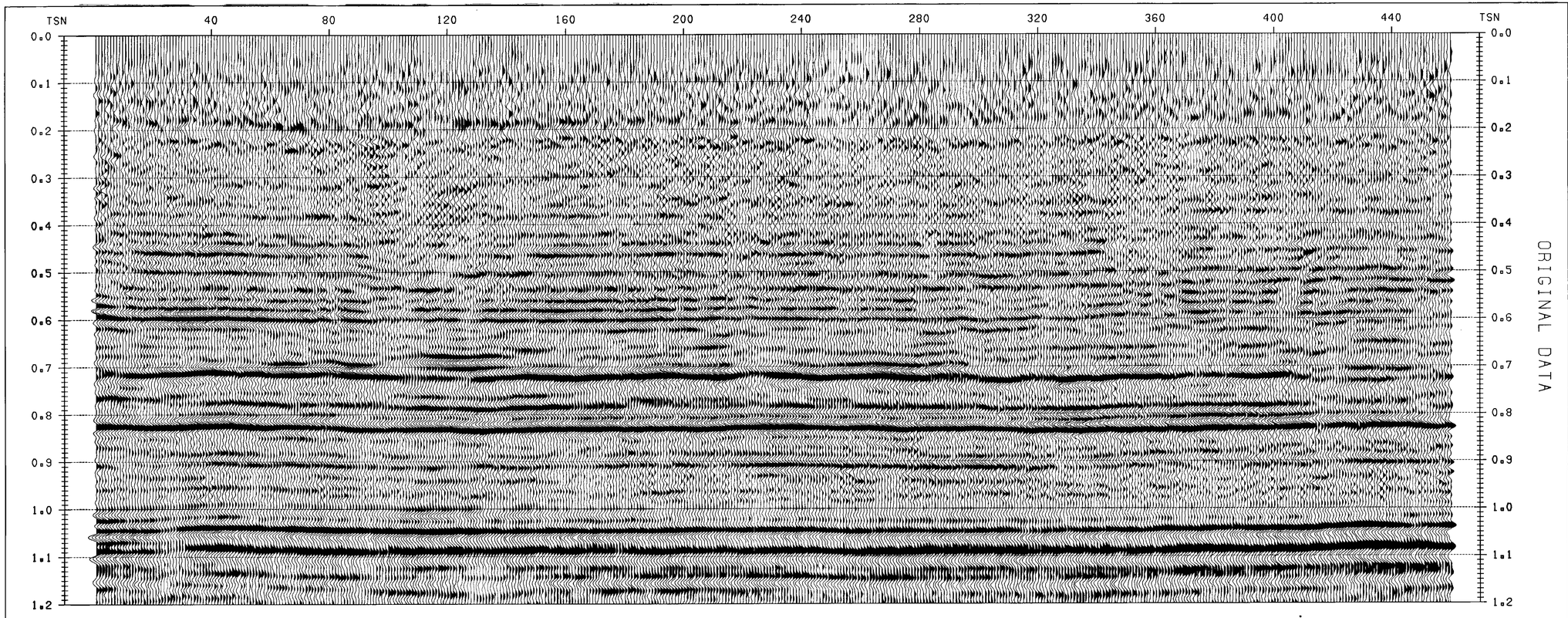

LINE C

200a

PLOTTED NORMAL POLARITY

ORIGINAL DATA

PROCESSED BY IT&A

INVERSE THEORY AND APPLICATIONS INC.

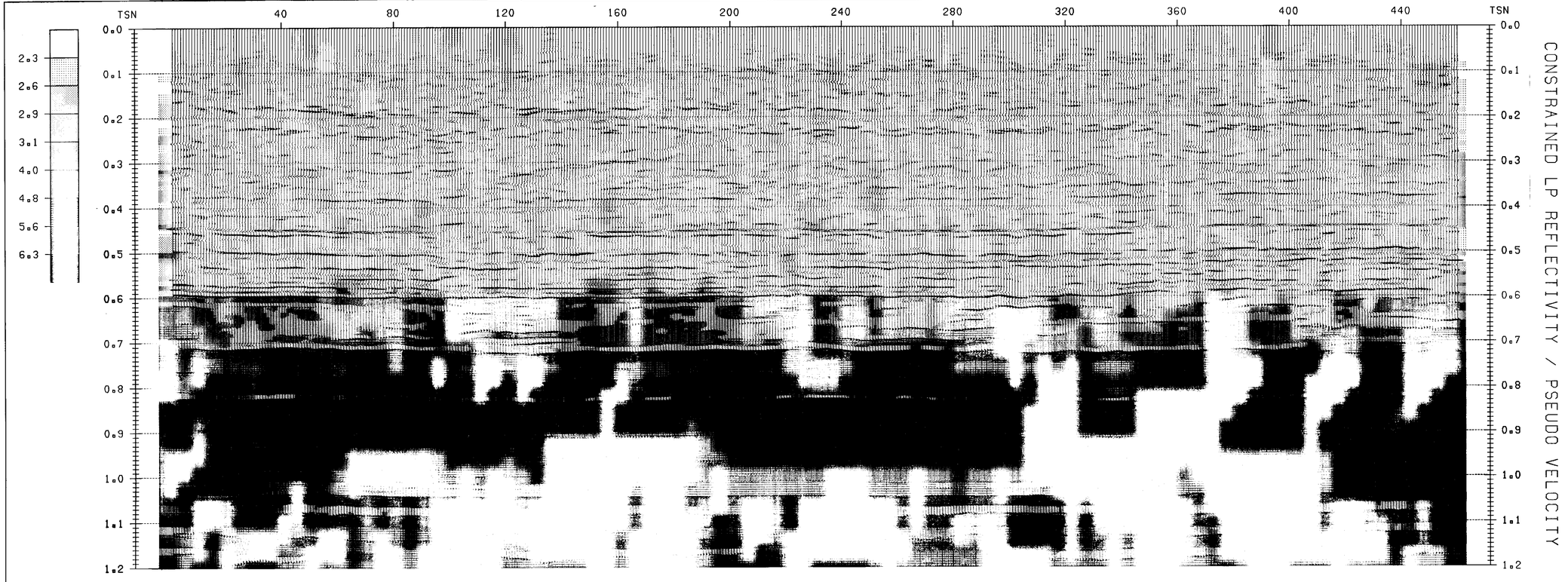

LINE C 200b

PLOTTED NORMAL POLARITY

PROCESSING SEQUENCE:

(1) INFORMATION BAND (12-55 HZ)

(2) GEOLOGIC DECONVOLUTION
- WELL LOG AND STACKING VELOCITY CONSTRAINTS

(3) 3 TRACE KLSTAK

(4) LFSTAK

(5) RMVBDI

(6) COLOUR LEVELS FROM GREY (KFEET/S)

PROCESSED BY IT&A

INVERSE THEORY AND APPLICATIONS INC.

REFERENCES

Aki, K., and Richards, P. G., 1980, Quantitative Seismology, Theory and Methods, v.1: W. H. Freeman and Co. 557 p.

Al-Chalabi, M., 1974, An analysis of stacking, RMS, average, and interval velocities over a horizontally layered ground: Geophysical Prospecting., v.22, p. 458-475.

Angeleri, G.P., and Carpi, R., 1982, Porosity prediction from seismic data: Geophysical Prospecting, v.30, p. 580-607.

Anstey, N.A., 1977, Seismic Interpretation- The Physical Aspects: International Human Resources Development Corporation.

Arons, A. B., and Yennie, D. R., 1950, Phase distortion of acoustic pulses obliquely reflected from a medium ofhigher sound velocity: J. Ac. Soc. Am. v. 22, p. 231-237.

Backus, G.E., and Gilbert, F., 1970, Uniqueness in the inversion of inaccurate gross earth data: Phil. Trans. R. Soc. London Ser. v.A-266, p. 123-192.

Backus, G. E., and Gilbert, J. F., 1967, Numerical applications of a formalism for geophysical inverse problems: Geophys. J. Roy. Astr. Soc., v. 13, p. 247-276.

Berkhout, A. J., 1977, Least squares inverse filtering and wavelet deconvolution: Geophysics, v. 42, p. 1369-1383.

Bilgeri, D., and Ademeno, E.B., 1982, Predicting abnormally pressured sedimentary rocks: Geophysical Prospecting, v.30, p. 608-621.

Bilgeri, D., and Carlini, A., 1981, Non-linear estimation of reflection coefficients from seismic data: Geophysical Prospecting, v.29, p. 672-686.

Bracewell, R., N., 1978, The Fourier Transform and its Applications: New York, McGraw-Hill Book Co., Inc., 2nd. ed. 444 p.

Burg, J. P., 1975, Maximum Entropy Spectral Analysis: Ph.D. Thesis, Stanford Univ.

Choy, G., L., and Richards, P., G., 1975, Pulse distortion and Hilbert transformation by multiply reflected and refracted body waves: SSA Bull., v. 65, p. 55-70.

Claerbout, J. F., 1976, Fundamentals of Geophysical Data Processing: McGraw-Hill Inc., 274 p.

Claerbout, J. F., and Muir, F., 1973, Robust modelling with erratic Data: Geophysics, v. 38, p. 826-844.

Deeming, T. J. and Taylor, H. L., 1981, Use of an improved l_1 norm minimization for wavelet processing of seismic sections: Presented at 51st. Annual International SEG Meeting, Oct.11-15, 1981, in Los Angeles.

Dix, C. H., 1955, Seismic velocities from surface measurements: Geophysics., v.20, p. 68-86.

Everett, J. E., 1974, Obtaining interval velocities from stacking velocities when dipping horizons are included: Geophysical Prospecting, v.22, p. 122-142.

Frazer, J., 1983, Vibroseis down the hole: Proc. Australian Petroleum Exploration Association 23rd Annual Meeting, p. 203-210, Melbourne.

Futterman, W. I., 1962, Dispersive body waves: J. of Geophysical Research, v.67, p. 5279-5291.

Gass, S., 1964, Linear Programming- Methods and Applications: McGraw-Hill Book Co.

Gibson, B., and K. Larner, 1984, Predictive deconvolution and the zero-phase source: Geophysics, v.49, p. 379-397.

Hemon, C., and Mace, D., 1978, The use of the Karhunen-Loeve transformation in seismic data processing: Geophysical Prospecting, v. 26, p. 600-626.

Huang, T.S., and Narenda, P.M., 1975, Image restoration by singular value decomposition: Appl. Opt., v.14, p.2213-2216.

Hubral, P., and Krey, T., 1980, Interval Velocities from Seismic Reflection Time Measurements: Tulsa, SEG, 203 p.

Jenkins, G., M., and Watts, D. G., 1969, Spectral Analysis and its Applications: San Francisco, Holden-Day, 525 p.

Karhunen, K., 1947, Uber Lineare Methoden in der Wahrscheinlichkeitsrechnung: Ann. Acad. Sci. Fenn., (Suomalainen Tiedeakatemia), v.37, p.1-79. (Translation by I.Selin, 1960: "On Linear Methods in Probability Theory." t-131 RAND Corp., Santa Monica, California).

Kesmarky, I., 1977, Estimation of reflector parameters by the virtual image technique: Geophysical Prospecting, v.25, p. 621-635.

Knopoff, L., 1964, Q: Reviews of Geophysics, v.2, p. 625-660.

Kramer, H. P., and Mathews, M. V., 1968, A linear coding for transmitting a set of correlated signals: Presented at the 38th Annual International SEG meeting, Denver, Co.

Krey, T., 1976, Computation of interval velocities from common reflection point movemout times for N layers with arbitrary dips and curvatures in three dimensions when assuming small shot-geophone distances: Geophysical Prospecting, v.24, p. 91-111.

Levin, F. K., 1971, Apparent velocity from dipping interface reflections: Geophysics, v.36, p. 510-516.

Levy, S., and Fullagar, P. K., 1981, The reconstruction of a sparse spike train from a portion of its spectrum and application to high resolution deconvolution: Geophysics, v.46, p. 1235-1243.

Levy, S., Walker, C., Ulrych, T. J., and Fullagar, P. K., 1982, A linear programming approach to the estimation of the power spectra of harmonic processes: I.E.E.E. Acoustic Section, v. 30 (4), p. 675-679.

Levy, S., and Oldenburg, D. W., 1982, The deconvolution of phase shifted wavelets: Geophysics, v.47, p. 1285-1294.

Levy, S., Ulrych, T. J., Jones, I. F., and Oldenburg, D. W., 1983, Applications of complex common signal analysis in exploration seismology: Presented at the 53rd Annual SEG Meeting Las Vegas.

Loeve, M., 1955, Functions Alteatories de Second Odre: Chapter 8, p.299-352, Hermann, Paris.

O'brien, P. N. S., 1967, Quantitative discussion on seismic amplitudes produced by explosions in Lake Superior: J. of Geoph. Res., v.72, p. 2569-2575.

Oldenburg, D. W., 1976, Calculation of Fourier transforms by the Backus-Gilbert method: Geophys. J. Roy, Astr. Soc. v.44, p. 413-431.

Oldenburg, D. W., and Samson, J. C., 1979, Inversion of interferometric data from cylindrically symmetric refractionless plasmas: J. Opt. Soc. Am., v.69, p. 927-942.

Oldenburg, D. W., 1981, A comprehensive solution to the linear deconvolution problem: Geophys. J. Roy. Astr. Soc., v. 65, p. 331-357.

Oldenburg, D. W., Levy, S., Whittall, K. P., 1981, Wavelet estimation and deconvolution: Geophysics, v. 46, p.

1528-1542.

Oldenburg, D. W., Scheuer, T. E., and Levy, S., 1983, Recovery of the acoustic impedance from reflection seismograms: Geophysics, v.48, p. 1318-1337.

Oldenburg, D. W., Levy, S., and Stinson, K., 1984, RMS velocities and recovery of the acoustic impedance: Submitted to Geophysics.

Parker, R. L., 1977, Understanding inverse theory: Ann. Rev. Earth Plan. Sci., v.5, p. 35-64.

Pelat, D., 1974, Karhunen-Loeve Series Expansion: A new approach for studying astrophysical data: Astron. and Astrophys., v.33, p.321-329.

Peterson, R.A., Fillipone, W.R., and Coker, F.B., 1955. The synthesis of seismograms from well log data: Geophysics, v.20, p.516-538.

Ready, R.J., and Wintz, P.A., 1973, Information Extraction, SNR improvement and data compression in multispectral imagery: IEEE Trans. Commun., v.COM-21, p.1123-1130.

Ristow, D., and Jurczyk, D., 1975, Vibroseis deconvolution, Geophysical Prospecting, v.23, p. 363-377.

Robinson, J. C., 1979, A technique for the continuous representation of dispersion in seismic data: Geophysics, v.44, p. 1345-1351.

_____ 1980a, Reply to discussion of Geophysics, v.44, p. 1345-1351: Geophysics, v.45, p. 1316-1317.

_____ 1980b, Reply to discussion of Geophysics, v.44, p. 1345-1351: Geophysics, v.45, p. 1881-1883.

Scheuer, T. E., 1981, The Recovery of Subsurface Reflectivity and Impedance Structure from Reflection Seismograms: M.Sc. Thesis, University of British Columbia.

Sherwood, J. W. C., and Trorey, A. W., 1965, Minimum phase and related properties of the response of a horizontally stratified absorptive earth to plane acoustic waves: Geophysics, v.30, p. 191-197.

Schneider, W. A., 1971, Developments in seismic data processing and analysis (1968-1970): Geophysics, v.36, p. 1043-1073.

Stone, D. G., 1974, Velocity and bandwidth: Paper presented at 44th annual international SEG meeting, Dallas

Taner, M.T., Koehler, F., and Sheriff, R.E.,1979, Complex

seismic trace analysis: Geophysics, v.44, p.1041-1057.

Taner, M. T., Cook, E. E., and Neidell, N. S., 1970, Limitations of the reflection seismic method. Lessons from computer simulations: Geophysics, v.35, p. 551-573.

Taylor, H. L., Banks S. C., and McCoy, J. F., 1979, Deconvolution with the L1 Norm: Geophysics, v.44, p. 39-52.

Ulrych, T. J., and Walker, C., 1982, Analytic minimum entropy deconvolution: Geophysics, v 47, p. 1295-1302.

Ulrych, T. J., and Bishop, T. N., 1975, Maximum entropy spectral analysis and autoregressive decomposition: Rev. Geophys. and Space Physics, v.13, p. 183-200.

Ulrych, T. J., and Clayton, R. W., 1976, Time series modelling and maximum entropy: Phys. Earth Plan. Int., v.12, p. 188-200.

Ulrych, T. J., Levy, S., Oldenburg, D. W., and Jones, I. F., 1983, Applications of the Karhunen-Loeve transformation in reflection seismology: presented at the 53rd Annual SEG meeting in Las Vegas.

Watanabe, S., 1965, Karhunen-Loeve expansion and factor analysis. Theoretical remarks and application. Reprinted in: Pattern Recognition, J. Sklansky, ed., Stroudsburg, Pennsylvania, 1973, (p.146-171).

Walker C., and Ulrych T. J., 1983, Autoregressive recovery of the acoustic impedance: Geophysics, v.48, p. 1338-1350.

Waters, K.H., 1978, Reflection seismology, a tool for energy resource exploration: New York, John Wiley and Sons.

Wiggins, R. A., 1978, Minimum entropy deconvolution: Geoexploration, v.16, p. 21-35.

Wood., L. C., Heiser, R.C., Treitel, S., and Riley, P. L., 1978, The debubbling of marine source signature: Geophysics, v. 43, p. 715-729.

Wuenschel, P. C., 1965, Dispersive body waves - an experimental study: Geophysics, v.30, p. 539-551.

APPENDIX 2-A: MEAN NOISE POWER AND THE VARIANCE OF A RANDOM NOISE PROCESS

This appendix justifies the use of the mean noise power as an estimate of the variance of the random noise process in the time domain, using the treatment of Jenkins and Watts (1969), p. 230-232) as a starting point.

Let the observed noise power at frequency ωj be regarded as a realization of the random variable Cj defined by

$$Cj = \mu^2 + \nu^2, \tag{2.A-1}$$

where μj and νj are random variables representing the real and imaginary parts of the noise in the frequency domain, i.e.,

$$\mu j = \sqrt{1/N} \sum_{n=0}^{N-1} Z_n \cos(\omega j t_n), \tag{2.A-2}$$

and

$$\nu j = \sqrt{1/N} \sum_{n=0}^{N-1} Z_n \sin(\omega j t_n),$$

The random noise process Z is assumed to be normal with mean zero and variance σ^2; hence,

$$\mathrm{Var}[\mu] = \sigma^2/2 = \mathrm{Var}[\nu] = V, \text{ for example.} \tag{2.A-3}$$

Suppose the high-frequency half of the spectrum of the seismogram $X(\omega)$ can be regarded as pure noise, and we define the random variable $\bar{C}$ by

$$\bar{C} = (2/N') \sum_{j=N''}^{N'} Cj,$$

where $N' = N/2$ and $N'' = N/4 + 1$. The sample mean $\bar{\sigma}^2$ defined in the text "statistical cutoff" section under "Selection of data....." is a realization of $\bar{C}$:

$$\bar{\sigma}^2 = (2/N') \sum_{j=N''}^{N'} |Xj|^2,$$

From equations (2.A-1) and (2.A-3) it may be observed that Cj is the sum of squares of two normal random variables with variance V, so Cj/V is distributed as χ^2_2. Hence, recalling equation (2.A-3),

$$\epsilon[Cj] = \epsilon[\bar{C}] = 2V = \sigma^2. \tag{2.A-4}$$

Therefore the sample mean of the noise power is an unbiased

estimator of the variance of the random noise process, i.e., $\bar{\sigma}^2$ is a valid estimate of σ^2.

$\bar{C}$ may be regarded as near normal on the strength of the central limit theorem and Gaussian confidence limits assigned with respect to

$$\mathrm{Var}[C] = 8V^2/N' = 2\sigma^4/N'. \qquad (2.A\text{-}5)$$

In the computer program, the (upper) Gaussian 95 percent confidence limit is adopted as the estimate of the variance. This conservative estimate can cause overcompensation for noise, particularly in the equality constraint formulation, with the result that only the most prominent spikes are recovered.

APPENDIX 2-B: THE CHOICE OF STATISTICAL CUTOFF IN LP DECONVOLUTION

The theory underlying the choice of the statistical cutoff in the "statistical cutoff" section under "Selection of data....." in the text is presented in this appendix.

The real part of the error in the deconvolved data is regarded as a realization of the random variable Q given by

$$Q = \mathrm{Re}\{E/W\} = [\mu \mathrm{Re}\{W\} + \nu\ \mathrm{Im}\{W\}]/|W|^2, \tag{2.B-1}$$

where this equation is understood to apply at each frequency. The treatment requires only trivial modification if Q is regarded as Im{E/W} instead.

The reliability of data is assessed by comparing $\mathrm{Re}^2\{X/W\}$ with a cutoff K defined in equation (2.9) in terms of $\epsilon[Q^2]$ and a parameter α. Hence, the distribution of Q^2 is of primary interest here. Since μ and ν in equation (2.A-2) are normal random variables with mean zero, so too is Q; therefore, $Q^2/\mathrm{Var}[Q]$ is distributed as χ^2_1. Hence, using equations (2.B-1) and (2.A-3),

$$\epsilon[Q^2] = \mathrm{Var}[Q] = \sigma^2/(2|W|^2), \tag{2.B-2}$$

which corresponds to equation (2.8).

As a increases, the probability that pure noise will exceed the cutoff decreases. More precisely,

$$\Pr\{Q^2>K\} = (1/\sqrt{2\pi}) \int_{2a^2}^{\infty} \exp(-x/2)dx/\sqrt{x} \qquad (2.B\text{-}3)$$

$$= \operatorname{erfc}(a).$$

Thus, if σ^2 were known exactly, setting $a = 2$ would reduce the probability of the inclusion of a pure noise value to less than 0.005.

APPENDIX 2-C: NOISE CONSIDERATION IN THE EQUALITY CONSTRAINTS FORMULATION OF LP DECONVOLUTION

Essential to the equality constraints formulation is a condition to ensure the statistical compatibility of the noise removed in the course of the computations; such a condition is derived below.

The real part of the noise μ will be considered, without loss of generality. Since μ is a normal random variable, μ^2/V is distributed as χ^2_1, with V defined in equation (2.A-3). Writing

$$|\mu| = \sqrt{\mu^2} = \sqrt{V} \cdot \sqrt{\mu^2/V},$$

it follows from Jenkins and Watts (1969, p. 71) that

$$\epsilon[|\mu|] = \sqrt{V/2\pi}\int_0^\infty \exp(-y/2)dy = \sigma/\sqrt{\pi}.$$

Hence,

$$\epsilon[S] = 2\sigma/\sqrt{\pi} \qquad (2.C\text{-}1)$$

for the random variable S defined in equation (2.13).

In the linear programming problem, μ and ν are expressed as differences between positive quantities, i.e.,

$$\mu m = um - \nu m \text{ and } \nu m = xm - ym, \quad m = 1, \ldots, M,$$

where M is the number of acceptable frequencies as before. The actual constraint imposed on the noise is

$$(1/M)\sum_{m=1}^{M} (um + \nu m + xm + ym) = e[S] = 2\sigma/\sqrt{\pi}. \tag{2.C-2}$$

This condition is consistent with equation (2.13), provided

$$|\mu m| = um + \nu m \text{ and } |\nu m| = xm + ym. \tag{2.C-3}$$

The validity of equations (2.C-3) derives from the fact that minimization of the L1-norm of a(t) is favored by relatively large noise values; with reference to equation (2.12), it is apparent that the trivial solution is feasible for sufficiently serious noise pollution. Therefore, given the constraint equation (2.C-2), the noise is most effective in reducing $||a||_1$ when it satisfies equations (2.C-3).

APPENDIX 6-A: AR SPIKING DECONVOLUTION OF BAND-LIMITED DATA

The problem of obtaining a sparse spike representation of band-limited reflection seismograms has been treated recently by a number of authors in the geophysical literature. The basic assumptions underlying this operation are:

(a) An earth model which consists of a set of physically distinct layers.

(b) A sparse reflectivity series, that is, reflections are generally separated by a number of zeros, and

(c) The recorded seismogram is a reasonable band-limited representation of the earth response function. That is, the source's phase and amplitude distortions are largely removed.

We express the second assumption by the equation:

$$r(t)=\sum_{n=0}^{N-1} r_n \cdot \delta(t-n\Delta) \qquad (6.A-1)$$

where N is the number of samples in the input seismogram,

r_n is the reflection coefficient at the nth sample,

Δ is the sampling interval, and

$\delta(t-n\Delta)$ represents a Dirac delta function at time $n\Delta$.

The digital Fourier transform of a sparse reflectivity series r(t) consists of the sum of a number of sinusoids and is written as:

$$R(w_j)=R_j=\sum_{n=0}^{N-1} r_n \exp(-i2\pi jn/N) \qquad (6.A-2)$$

with j being the index of w the angular frequency, and

n the time sampling index.

It is obvious that each frequency in the series $R(w_j)$ contains contributions from each of the spikes present in the reflectivity series. Hence, it is expected that under the assumptions specified previously, a full-band estimate of the reflectivity function r(t) can be obtained from an incomplete set of $R(w_j)$'s via the use of appropriate numerical techniques. In this work, we have used the Linear Programming and the Auto-Regressive technique which will be described next.

Auto-Regressive Deconvolution

As was shown in equation (6.A-2), the frequency representation of a sparse-spike series consists of a sum of a number of complex sinusoids each of which corresponds to a specific non-zero reflection coefficient. The problem of spectral extension can then be viewed as an Auto-Regressive process where a complex prediction filter $\{\underline{\beta}k\}$ is calculated and the available information is extrapolated by a convolution with this filter. The process is

simply summarized by the following set of equations.

Let the forward AR prediction be given by:

$$R_j = \sum_{k=1}^{p} \underline{\beta}_k R_{j-k}$$

and the reverse AR prediction by:

$$R^*_j = \sum_{k=1}^{p} \underline{\beta}_k R^*_{j+k}$$

with p being the order (length) of the prediction operator $\{\underline{\beta}k\}$, and * denoting the complex conjugate. We seek a prediction filter $\underline{\beta}$ such that the sum of the forward and reverse prediction errors is minimized in a least-squares sense. That is, the filter coefficients are found through the minimization of:

$$e^2 = 1/(N-p) \sum_{j=p+1}^{N} |R_j - \sum_{k=1}^{p} \underline{\beta}_k R_{j-k}|^2$$

$$+ 1/(N+p) \sum_{j=1}^{N-p} |R^*_j - \sum_{k=1}^{p} \underline{\beta}_k R^*_{j+k}|^2 .$$

Details of some of the approaches to the solution of this minimization problem are given in Burg (1975), Ulrych and Clayton (1976), Ulrych and Bishop (1975) and Claerbout (1976).

The reader who is familiar with the AR process probably realizes that the order of the prediction filter is quite important to a successful spectral extension process. Since one prediction coefficient is required for the extrapolation of each sinusoid, the ideal order of the AR process should be equal to or larger than the

number of layers NL in our model. However, for band-limited real data, where we are given only M<(N+1)/2 frequency observations the requirement p>NL cannot be met. Hence, in this case, we hope that the process will detect only the larger reflectors in our model, thereby, reconstructing only the information concerning the major features of the sought reflectivity model. Our experience to date with a large number of synthetic as well as real data examples have proven the process to be quite successful. However, in cases where the local geology cannot be approximated by a relatively small number of reflectors the AR process, and also the LP will have a somewhat lower likelihood of success.

APPENDIX 7-A: THE DECONVOLUTION OF PHASE-SHIFTED WAVELETS

7-A.1 INTRODUCTION

In both reflection and refraction seismic studies, it is often assumed that the earth is composed of a number of homogeneous layers. A typical seismogram from such an earth model can be approximated by convolving a source wavelet with a set of reflectivity coefficients. The source energy is assumed to be propagating as a plane wave, and the reflectivity sequence is ideally a set of Dirac delta functions located at times corresponding to primary and multiple reflections from the layered earth model. Given that this "convolutional model" for a seismogram has some validity, a standard procedure is first to estimate a source wavelet and then to remove its effect by deconvolution. The resultant estimate of the reflectivity sequence is used to interpret the parameters of the layered earth structure.

A complicating factor to this simplistic approach is introduced when wide-angle reflections are considered or when the wave-front or reflective boundary is curved. Under these conditions, the angle of incidence for the incoming ray can be supercritical and inhomogeneous waves will be created on the boundary (Aki and Richards, 1980, p. 155). The reflectivity coefficient for the layer becomes complex; consequently, the shape of the emerging wave packet differs from the impinging one. The amount of distortion depends upon the phase ϵ of the complex reflection coefficient. Following

Arons and Yennies (1950) [or Aki and Richards (1980)], the altered waveform $w(\epsilon;t)$ can be written as

$$w(\epsilon;t) = \cos(\epsilon)\cdot w(t) + \sin(\epsilon)\cdot H[w(t)] \tag{7-A.1}$$

where H[ ] denotes the Hilbert transform. Basically, upon interacting with the boundary, the positive frequencies in w(t) are advanced by ϵ and the negative frequencies are retarded by ϵ; it is this sign effect which is responsible for the Hilbert transform in equation (7-A.1).

The importance of an alteration in the waveform can be appreciated when one attempts to estimate an arrival time for a wavelet that has been significantly phase shifted. For example, if $\epsilon = \pi/2$, then $w(\epsilon;t) = H[w(t)]$, and the altered waveform will differ greatly from w(t). In particular, if w(t) is delta-like, $w(\epsilon;t)$ will have an emergent portion of significant amplitude at times preceding those expected from geometrical ray computations. Estimating the arrival time to be near the onset of the emergent energy can produce appreciable error. Choy and Richards (1975) presented whole earth seismograms for SH waves in which various S arrivals are clearly phase shifted by approximately $\pi/2$; they suggested that errors in estimating the arrival time of the phase-shifted wavelets could be as large as 3 to 5 sec.

Another area in which waveform alteration can have significant consequences is in exploration seismology where wide-angle

reflections , nonplanar waves, and dipping layers produce conditions of supercritical reflection. Attempting to follow an event horizon by correlating peak (or troughs) on successive traces in a record section can lead to erroneous results if the character of the wavelet changes from trace to trace.

The purpose of this paper is to overcome these difficulties by introducing a complex reflectivity function from the outset. The convolution of this reflectivity function with an analytic source wavelet produces an analytic seismogram. Once recast as a convolution problem, linear inverse theory is used to deconvolve the analytic seismogram to obtain unique averages of the real and imaginary parts of a complex reflectivity function. Information about the amplitude and phase of the reflectivity function is recoverable through techniques of model construction or by using a simplified interpretation based upon the modulus of the deconvolved output. This latter method is not exact, but it works well if the seismic arrivals are not too close together.

Here we apply the analytic deconvolution technique only to synthetic data, but Ulrych and Walker (1982) use our analytic formulation and a complex version of minimum entropy deconvolution (MED) to deconvolve a set of normal incidence seismograms. Their work presents an important and practical extension of the analytic formulation, since the MED algorithm does not require knowledge of the wavelet; in fact, an estimate of the source wavelet can be obtained by inverting the MED filter. In those cases where the source function is not known, such an estimated wavelet is a crucial first step to carrying out the deconvolution by the methods

presented here.

7-A.2 THEORY

In many physical problems, a data set x(t) is generated by the superposition of time-displaced replications of a source wavelet w(t) that is,

$$x(t) = r(t)*w(t), \qquad (7\text{-A.2})$$

where * denotes the convolution operator. In seismological problems, r(t) is called the reflectivity function. For normal incidence seismograms over a layered earth it can be written as

$$r(t) = \sum_{j=1}^{M} r_j \delta (t - \tau_j), \qquad (7\text{-A.3})$$

so that

$$x(t) = \sum_{j=1}^{M} r_j w(t - \tau_j), \qquad (7\text{-A.4})$$

where r are reflection coefficients and τ_j are the delay times related to layer thicknesses and material velocities. When the data are adequately represented by equation (7-A.2), the recovery of r(t), when w(t) is known, is a well-posed linear inverse problem for which a variety of solutions have been given in the literature. But there exist cases of practical importance where neither equation (7-A.2) nor equation (7-A.4) is adequate because w(t) has been phase

shifted upon reflection from a boundary. Consequently, the data consist of a superposition of wavelets, each phase shifted by an arbitrary and unknown amount. Any attempt to deconvolve without allowing for these phase shifts will produce a poor estimate or r(t).

If w(t) is used to denote the Hilbert transform H[w(t)], then a wavelet, phase shifted by an amount ϵ, can be written as

$$w(\epsilon;t) = \cos \epsilon \cdot w(t) + \sin \epsilon \cdot \tilde{w}(t)$$

$$= \mathrm{Re}\{\hat{w}(t) \cdot \exp[i\epsilon]\},$$

where Re denotes the real part and $\hat{w}(t)$ is the analytic wavelet

$$\hat{w}(t) = w(t) - i\tilde{w}(t)$$

(Bracewell, 1978, p.268). Allowing for phase-shifted wavelets, equation (7-A.4) can be rewritten as

$$x(t) = \sum_{j=1}^{M} r_j \, w(\epsilon_j, \, t - \tau_j)$$

$$= \mathrm{Re}\left\{ \sum_{j=1}^{M} r_j \exp[i\epsilon] \cdot \hat{w}(t - \tau_j) \right\}, \qquad (7\text{-A.5})$$

By introducing the continuous function

$$r(t) \cdot \exp[i\epsilon(t)] = \sum_{j=1}^{M} r_j \cdot \exp[i\epsilon_j] \cdot \delta(t - \tau_j),$$

equation (7-A.5) may be rewritten as

$$x(t) = \mathrm{Re}\{r(t)\cdot \exp[i\epsilon(t)] * \hat{w}(t)\}. \tag{7-A.6}$$

From equation (7-A.6) it can be seen that the seismogram $x(t)$ is the real part of the convolution product of a complex reflectivity function and the analytic representation of the wavelet.

Although equation (7-A.6) is nearly in the form of equation (7-A.2), the real part on the right-hand side prevents us from applying known deconvolution techniques to recover $r(t)$ and $\epsilon(t)$. It is convenient, therefore, to introduce the analytic signal $\hat{x}(t) = x(t) - i\tilde{x}(t)$. Then, since the bracketed term in equation (7-A.6) is an analytic signal, it follows that

$$\hat{x}(t) = r(t)\cdot \exp[i\epsilon(t)] * \hat{w}(t). \tag{7-A.7}$$

This is the desired convolution formula, and evidently standard procedures can be used to recover $r(t)$ and $\epsilon(t)$ if $w(t)$ is known. Here we shall treat the deconvolution as a linear inverse problem and use the formalism developed in Oldenburg (1981).

Let us first define a complex model $m(t)$ as

$$m(t) = r(t)\, \exp[i\epsilon(t)]. \tag{7-A.8}$$

Then equation (7-A.7) can be rewritten as

$$\hat{x}(t) = m(t)*\hat{w}(t) + \hat{n}(t), \qquad (7\text{-A.9})$$

where the analytic noise $\hat{n}(t)$ has been included to account for additive noise $n(t)$ in the measured signal. Sometimes, the power spectrum of $n(t)$ may be known; or, in the absence of that information, one can assume that $n(t)$ is uncorrelated Gaussian noise with an estimated standard deviation, σ_0. The noise statistics of $\hat{n}(t)$ are easily computed from $n(t)$, but the result will depend upon the algorithm used to compute the Hilbert transform. If the digital Fourier tranform is used, the power spectrum of $n(t)$ will be the same as that of $\hat{n}(t)$ when $n(t)$ is unbiased.

The deconvolution of equation (7-A.9) will be carried out in the frequency domain. It is assumed here that all time functions are periodic with period T. The Fourier transform of any such function $g(t)$ is given by

$$G(f_k) = G_k = 1/T \int_{-T/2}^{T/2} g(t) \cdot \exp[-i2\pi kt/T]\, dt,$$

$$k = 0, +1, +2, \ldots,$$

and the inverse Fourier transform is

$$g(t) = \sum_{k=-\infty}^{\infty} G_k \cdot \exp[i2\pi kt/T]$$

Unique information about m(t) will be found by constructing an analytic filter $\hat{v}(t)$ such that an analytic averaging function

$$\hat{a}(t) = \hat{w}(t)*\hat{v}(t) \qquad (7\text{-A.}10)$$

is "as close as possible" to some desired function $\hat{h}(t)$. Ideally we want $\hat{v}(t)$ to contract $\hat{w}(t)$ into a real delta-like function. However, this is impossible in the anlytic formulation because $\hat{w}_k = 0$ for $k<0$; hence the negative frequencies are lost from the solution. This is the price paid so that phase-shifted wavelets can be treated in a convolution format. The unique averages of the model are found by convolving $\hat{v}(t)$ with the analytic signal. That is,

$$\begin{aligned} <m(t)> &= \hat{x}(t)*\hat{v}(t) \\ &= m(t)*\hat{a}(t). \end{aligned} \qquad (7\text{-A.}11)$$

The statistical variance of the averages is given by

$$\mathrm{Var}[<m(t)>] = \mathrm{Var}[\hat{n}(t)*\hat{v}(t)]. \qquad (7\text{-A.}12)$$

The concept of unique averages is sometimes misunderstood, so an elaboration is useful. Let us first suppose that the data are accurate. The first equality in equation (7-A.11) shows that $<m(t)>$ is obtained from linear combinations of the data, and the second equality shows that any model which identically reproduces the data will have these same averages. It is in this sense that the averages are unique; consequently, $<m(t)>$ and $\hat{a}(t)$ summarize our knowledge

about all possible models which might reproduce the data. However, if the data are inaccurate, the averages must also be inaccurate. This statisical inaccuracy is quantified by the variance in equation (7-A.12).

The analytic filter can be found by minimizing

$$\phi = \cos\theta \cdot \int_{-T/2}^{T/2} |\hat{a}(t) - \hat{h}(t)|^2 dt$$

$$+\sin\theta \cdot \mathrm{Var}[\langle m(t)\rangle], \quad 0<\theta<\pi/2. \tag{7-A.13}$$

The usual trade-off parameter θ has been included in equation (7-A.13), and it controls the trade-off between resolution and accuracy of the averages. Following Oldenburg (1981), we use Parseval's theorem and the convolution theorem to rewrite equation (7-A.13) as

$$\psi = \cos\theta \cdot \sum_{k=0}^{\infty} T|T\hat{W}_k\hat{V}_k - \hat{H}_k|^2$$

$$+ \sin\theta \cdot T^2 \sum_{k=0}^{\infty} |\hat{N}_k\hat{V}_k|^2. \tag{7-A.14}$$

The lower limit on the summation is k = 0 instead of the usual k = - ∞ because the spectral components of analytic functions are zero for negative frequencies. The Fourier coefficients of the desired filter, found by differentiating equation (7-A.14) with respect to $\hat{V}_k^*$ and setting $\partial\psi/\partial V_k^* = 0$, are

$$\hat{V}_k = \frac{\cos\theta \cdot \hat{H}_k \hat{W}^*_k}{T|\hat{W}_k|^2 \cos\theta + |\hat{N}_k|^2 \sin\theta}, \qquad k > 0,$$

$$V = 0, \qquad k, < 0, \qquad (7\text{-A.}15)$$

where the * denotes the complex conjugate. In the special case $\hat{h}(t) = \hat{\delta}(t)$, a Dirac delta function centered at the origin,

$$V_k = \frac{\cos\theta \cdot \hat{W}^*}{T^2|\hat{W}_k|^2 \cdot \cos\theta + T|\hat{N}_k|^2 \cdot \sin\theta}, \qquad k > 0$$

$$V = 0, \qquad k<0, \qquad (7\text{-A.}16)$$

Equation (7-A.16) reduces to $\hat{V}_k = 1/(T^2\hat{W}_k)$ when $\theta = 0$; this result is identical to that obtained when solving $\hat{\delta}(t) = \hat{w}(t)*\hat{v}(t)$ by using the convolution theorem and dividing in the frequency domain.

With $\hat{v}(t)$ computed, the averaging function $\hat{a}(t)$ is easily found from equation (7-A.10). The averages [from equation (7-A.11)] have the form

$$\langle m(t)\rangle = \hat{x}(t)*\hat{v}(t) = m(t)*a(t) - im(t)*\tilde{a}(t). \qquad (7\text{-A.}17)$$

It is seen that $\langle m(t)\rangle$ is the sum of two averages of the model. One of these averages is the inner produce to m(t) with a delta-like function a(t), and the other average is the inner product of m(t)

with $\tilde{a}(t)$. Only in the special case where $m(t)$ is purely real or purely imaginary can the interpretation proceed with the same ease that it does in ordinary deconvolution algorithms. In general, the model

$$m(t) = r(t)\cdot\cos\,\epsilon(t) + ir(t)\cdot\sin\,\epsilon(t) \tag{7-A.18}$$

will have both real and imaginary components; consequently, the real and imaginary parts of $\langle m(t)\rangle$ have the form

$$\begin{aligned} \mathrm{Re}\langle m(t)\rangle &= \mathrm{Re}\{\hat{x}*\hat{v}\} = r(t)\cdot\cos\,\epsilon(t)*a(t) \\ &\quad + r(t)\cdot\sin\,\epsilon(t)*\tilde{a}(t), \\ \mathrm{Im}\langle m(t)\rangle &= \mathrm{Im}\{\hat{x}*\hat{v}\} = r(t)\cdot\sin\,\epsilon(t)*a(t) \\ &\quad -r(t)\cos\epsilon(t)*\tilde{a}(t). \end{aligned} \tag{7-A.19}$$

The averages in equation (7-A.19), their statistical error, and the averaging functions contain the desired information about $r(t)$ and $\epsilon(t)$. The general problem of recovering information about $r(t)$ and $\epsilon(t)$ from equation (7-A.19) will be considered, but first a simple, insightful example will be presented. We consider a single complex reflective coefficent located at $t = \tau_1$ so that the model is

$$m(t) = r_1 \exp[i\epsilon_1]\ \delta(t-\tau_1).$$

From equation (7-A.19) the real and imaginary parts of the averages become

$$\mathrm{Re}\langle m(t)\rangle = r_1 \cos\epsilon_1 a(t-\tau_1) + r_1 \sin\epsilon_1 \tilde{a}(t-\tau_1).$$

$$\mathrm{Im}\langle m(t)\rangle = r_1 \sin\epsilon_1 a(t-\tau_1) - r_1 \cos\epsilon_1 \tilde{a}(t-\tau_1).$$

Consequently, $\mathrm{Re}\langle m(t)\rangle$ will look like a reproduction of $a(t)$, and the imaginary part will have the form of $\tilde{a}(t)$ if ϵ_1 is close to zero or π. Alternatively, if ϵ_1 is close to $\pi/2$ (or $3\pi/2$), the $\mathrm{Re}\langle m(t)\rangle$ will resemble $\tilde{a}(t)$ and the imaginary part will look like $a(t)$. For intermediate values of ϵ_1, the delta function spike in the model will be seen as a linear combination of a delta-like averaging function and its Hilbert transform. For the current example, we shall choose $\epsilon_1 = \pi/4$. The wavelet and data are shown in Figure 7-A.1, and the results of the deconvolution obtained by using equation (7-A.16) with $\theta = 0$ are shown in Figures 7-A.1c-1f. Clearly, both the real and imaginary parts of the averages are linear combinations of $a(t)$ and $\tilde{a}(t)$. If the data were inaccurate the deconvolution could not be carried out at $\theta = 0$; some sacrifice in resolution would have to be made in order to achieve statistical reliability in the averages. This could be effected by using equation (7-A.16) with a value of θ greater than zero. Typical results are shown in Figures 7-A.1g-1j.

Our ultimate goal is to determine the values of the parameters

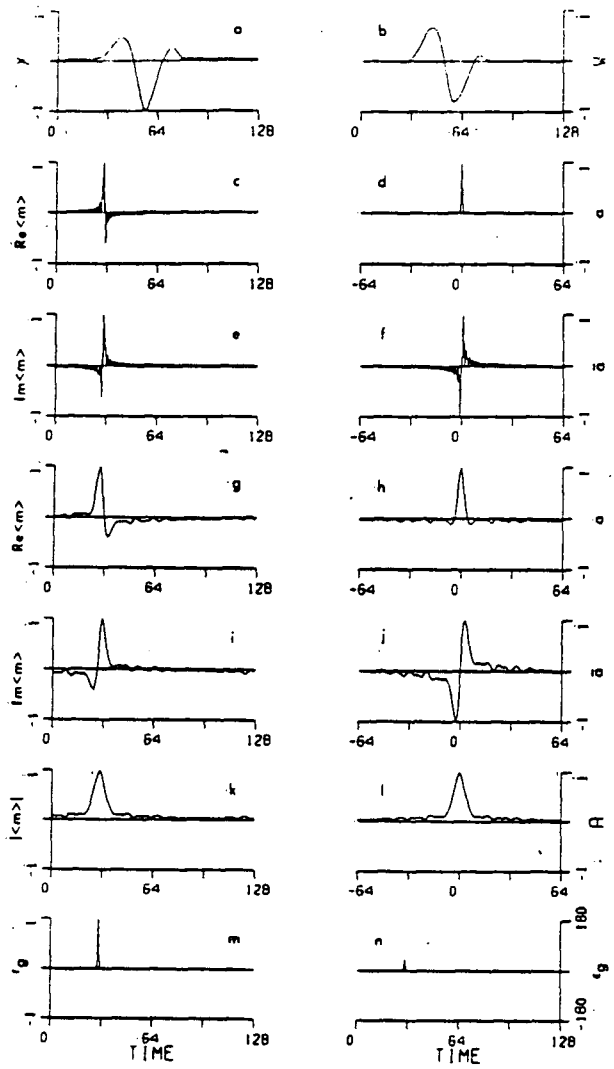

Figure 7-A.1

Shown in successive panels are (a) the data obtained by phase-shifting the wavelet in (b); (c) the real part of the averages obtained by deconvolving with θ = 0; (d) the averaging function a(t); (e) the imaginary part of the averages obtained by deconvolving with θ = 0; (f) the Hilbert transform of a(t); (g)-(j) are the same as the results in (c) - (f) except that the deconvolution was carried out with θ > 0; (k) the modulus of the averages in (g) and (i); (l) the modulus A(t) of the averaging function [equation (7-A.20)]; (m) the recovered reflectivity function; (n) the recovered phase function.

$(\tau_1, r_1, \epsilon_1)$ from the averages in Figures 7-A.1g-1i (or 1c and 1e). There are a number of ways to accomplish this. The first method uses the modulus of the averages. For the example of a single reflector, the modulus of $\langle m(t) \rangle$ is easily shown to be independent of the phase ϵ_1 and equal to

$$|\langle m(t) \rangle| = |\hat{x}(t) * \hat{v}(t)| = r_1 \sqrt{a(t - \tau_1)^2 + \tilde{a}(t - \tau_1)^2}$$
$$= r_1 A(t - \tau_1).$$

where (7-A.20)

$$A(t) = \sqrt{a(t)^2 + \tilde{a}(t)^2}.$$

Thus $|\langle m(t) \rangle|$ is scaled and translated replication of A(t), and the best values for the scaling factor r_1 and the time delay τ_1 are those which minimize the difference between the left- and right-hand sides of equation (7-A.20). The modulus of the averages and A(t) are shown in Figures 7-A.1k - 1l.

In an alternative method, τ_1 and r_1 can be estimated by recognizing that A(t) is a delta-like function whose maximum is at t = 0; the time difference between zero and the location of the maximum in $|\langle m(t) \rangle|$ will thus provide an estimate for τ_1. Moreover, $\tilde{a}(t = 0) = 0$, so r_1 can be recovered directly from

$$r_1 = 1/A(0) \cdot \max |\langle m(t) \rangle|, \qquad (7\text{-A.21})$$

where max indicates the maximum value. The phase ϵ_1 can be estimated

from the function

$$\phi(t) = \tan^{-1}\,[\mathrm{Im}\langle m(t)\rangle\,/\mathrm{Re}\langle m(t)\rangle] =$$
$$\tan^{-1}\{[\sin\epsilon(t)a(t-\tau_1)-\cos\,\epsilon(t)\tilde{a}(t-\tau_1)]\,/$$
$$[\cos\,\epsilon(t)a(t-\tau_1)+\sin\,\epsilon(t)\tilde{a}(t-\tau_1)]\}$$

(7-A.22)

which, at time $t = \tau_1$, reduces to

$$\phi(t=\tau_1) = \tan^{-1}[\sin\,\epsilon(t)/\cos\,\epsilon(t)] = \epsilon(\tau_1).$$

(7-A.23)

Thus the phase shift ϵ_1 can be found by evaluating $\phi(t)$ at percisely the arrival time of the wavelet. The recovered amplitude and phase are shown in Figures 7-A.1m and 1n.

It is clear that if the data were accurate and consisted of a single phase-shifted wavelet there would be no problem in computing the arrival time of the pulse, the magnitude of the reflective coefficient, and the phase shift. In spite of its success, we emphasize that equation (7-A.23) should be used with some caution because a(t) is large if t is not precisely zero. A small error in estimating τ_1 can lead to a large error in ϵ_1.

The interpretation of the deconvolution results is less straight- forward when the data are inaccurate or when multiple reflectors are sufficiently close so that averaging functions from

different reflective events overlap. These complexities affect the averages differently so they are treated separately. The effects of observational errors are considered first.

Let $n(t)$ represent the additive noise on the seismogram, and $\tilde{n}(t)$ and $\hat{n}(t)$, respectively, represent the Hilbert transform of the noise and the analytic noise signal. The averages of the model can be written as

$$\langle m(t)\rangle = \hat{x}(t)*\hat{v}(t) = \langle m(t)\rangle_{true} + \delta\langle m(t)\rangle, \tag{7-A.24}$$

where $\hat{v}(t)$ is the analytic filter [equation (7-A.16)] and $\delta\langle m(t)\rangle$ represents the discrepancy between the true average and that computed from the erroneous data. Since $\hat{x}(t) = \hat{x}(t)_{true} + \hat{n}(t)$, it follows that

$$\delta\langle m(t)\rangle = \hat{n}(t)*\hat{v}(t). \tag{7-A.25}$$

and thus

$$\begin{aligned} \delta\ \mathrm{Re}\langle m(t)\rangle &= 2n(t)*v(t), \\ \delta \mathrm{Im}\langle m(t)\rangle &= -2H[n(t)*v(t)]. \end{aligned} \tag{7-A.26}$$

By using Parseval's equation, the convolution theorem for Fourier transforms, and the assumption that n(t) is stationary, it follows from equation (7-A.26) that the variance of the averages is evenly divided between the real and imaginary parts, that is,

$$\text{Var}[\text{Re}\langle m(t)\rangle] = \text{Var}[\text{Im}\langle m(t)\rangle] = T^2/2\sum_{k=1}^{\infty} |\hat{N}_k \hat{V}_k|^2. \tag{7-A.27}$$

[The sum in equation (7-A.27) begins at $k = 1$ instead of $k = 0$ because the noise is assumed to be unbiased, and hence $N_0 = 0$.]

In addition, approximate formulas for the variances of $|\langle m(t)\rangle|$ and $\phi(t)$ can be computed from the Taylor expansion technique presented by Jenkins and Watts (1969, p. 76). We have

$$\text{Var}[\,|\langle m)(t)\rangle|\,] \approx \text{Var}[\text{Re}\langle m(t)\rangle], \tag{7-A.28}$$

and

$$\text{Var}[\phi(t)] \approx \text{Var}[\text{Re}\langle m(t)\rangle]/|m(t)|^2 \tag{7-A.29}$$

In deriving equations (7-A.27), (7-A.28), and (7-A.29), we have used the fact that for stationary noise $\text{Cov}[\eta(t), \tilde{n}(t)] = 0$. Further, in equation (7-A.29), the denominator should really be

$\{E[Re\langle m(t)\rangle]\}^2 + \{E[Im\langle m(t)\rangle]\}^2$ where E denotes the expected value; these quantities, however, are unknown and have been replaced with their measured values.

A second interpretive complication arises when the reflective horizons are so close that there is significant overlap of the averaging functions in the deconvolved output. An attempt to infer directly from $\langle m(t)\rangle$ the correct values of the phase shifts, the arrival times of the wavelets, and the magnitude of the reflective coefficents may produce poor results if equations (7-A.21) and (7-A.23) are used alone. In fact, the problem encountered is similar to that faced in interpreting the results from standard deconvolution techniques. There, each reflective event appears as an averaging function multiplied by some amplitude factor. If reflective events are so close that the averaging functions overlap significantly, then the location of the maxium of $\langle m(t)\rangle$ may no longer coincide with the true arrival time of a wavelet. In the extreme, two reflective events might appear as a single peaked function in the averages with the time at which the peak occurs lying between the two true arrival times.

Our problem in deconvolving phase-shifted signals is somewhat worse than in the standard deconvolution problem because the averages $\langle m(t)\rangle$ are complex combinations of delta-like averaging functions and their Hilbert transforms. Here we present two methods for recovering $r(t)$ and $\epsilon(t)$ from the averages in equation (7-A.17). The first method is one of many possible model construction techniques; it will yield good results even when the reflective

events are close together. The second method is based upon the approximate formulas in (7-A.21) and (7-A.23); it will work well if the reflective events are sufficiently separated in time. In fact, the approximate formulas appear to be quite good and should provide acceptable results for many practical cases of interest.

Our construction algorithm is a parametric least-squares solution to obtain a "best guess" for r(t) and $\epsilon(t)$, where

$$r(t)\cdot\exp[i\epsilon(t)] = \sum_{j=1}^{M} r_j\cdot\exp[i\epsilon_j]\cdot\delta(t-\tau_j).$$

Following the formalism outlined by Oldenburg (1981) closely, we first determine, from the averages, the number of resolvable spikes M and their approximate time locations τ_j, j =1,....M. Then either the real or imaginary portion of <m(t)> can be used to find a set of parameters $\{\tau j, aj, \underline{\beta} j\}$, j = 1, ...,M, such that

$$\chi^2 = \sum_{k=1}^{N}\{\sum_{j=1}^{M} a_j\, a(t_k-\tau_j) + \underline{\beta}_j\,\tilde{a}(t_k-\tau_j) - \mathrm{Re}\langle m(t_k)\rangle\}^2 \qquad (7\text{-A.30})$$

is minimized. In equation (7-A.30), aj = rj·cos(ϵj) and $\underline{\beta}$j = rj sin(ϵj). A best guess of the magnitude of the reflectivity coefficients and the phase advances is easily derived from {aj, $\underline{\beta}$j}.

The second method for finding the parameters $\{\tau j, rj, \epsilon j\}$ uses an approximation involving the modulus of the averages. We saw from

equation (7-A.20) that when the data comprised a single wavelet, $|\langle m(t)\rangle| = r_1 A(t - \tau_1)$, where r_1 was the reflectivity coefficient. When the data comprised multiple wavelets, it might be hoped that

$$|\langle m(t)\rangle| = \sum_{j=1}^{M} rjA(t - \tau j), \qquad (7\text{-A.31})$$

that is, the modulus of the averages would be scaled and displaced replications of A(t). From an examination of equation (7-A.19), it takes little effort to show that equation (7-A.31) cannot be true in general. Nevertheless, we still expect equation (7-A.31) to hold approximately whenever the reflective events are separated by times somewhat greater than the width of A(t). In such circumstances the delay times τj can be equated to the times at which $|\langle m(t)\rangle|$ achieves a significant maximum, and the approximate amplitudes and phases can be determined by

$$rj \approx 1 / A(0) \cdot |\langle m(\tau j)\rangle|, \qquad (7\text{-A.32})$$

and

$$\epsilon j \approx \tan^{-1} [\mathrm{Im}\langle m(\tau j)\rangle / \mathrm{Re}\langle m(\tau j)\rangle]. \qquad (7\text{-A.33})$$

Variances of these quantities can be evaluated by using equations (7-A.27), (7-A.28), and (7-A.29).

The approximation (31), (7-A.32), and (7-A.33) must deteriorate when

the reflective events are closer together. To illustrate this, we consider an example in which successive sets of data are generated from a model consisting of two reflective coefficients ($r_1 = r_2 = 1.0$; $\epsilon_1 = \pi/4$, $\epsilon_2 = \pi/2$) which are brought closer together. The distance between the two spikes is decreased from 10 to 1 digitization interval. Although no noise is added to the data, the inversions are carried out (as in all realistic examples) by using a nonzero value of θ in equation (7-A.16). The averaging functions used for this example are identical in character but slightly narrower than those in Figures 7-A.1h, 1j, and 1l. Here w , the full width if A(t) at half its maximum value, is 6 digitization intervals. The results are given in Table 1a shows {rj, ϵj, τj} obtained by minimizing equation (30, and Table 1b gives the model parameters estimated from equations (7-A.31), (7-A.32), and (7-A.33).

The delay times, reflectivity amplitudes, and phase advances from the least-squares analysis are seen to be identical to their true values until $\Delta\tau$ /w $\approx$ 0.3. At that point there is no longer any indication in the averages that two spikes exist. Rather, |<m(t)>| shows only one peak; hence the least-squares program estimates a reflective amplitude of approximately $r_1 + r_2 = 2.0$.

The estimates of {rj, ϵj, τj} obtained by using equations (7-A.31), (7-A.32), and (7-A.33) are reasonably close to the true values for separations $\Delta\tau$/w >1, and the delay times are still well determined for even smaller separations. This indicates that the approximations in equations (7-A.32) and (7-A.33) should perform

well in practice as long as $\Delta\tau/w > 1$.

Table 7-A.1 (a) displays the best guess for $\{r, \epsilon, \tau\}$ obtained by minimizing equation (7-A.30). In the true model, the first spike was held at $\tau_1 = 10$, $\tau_2 = \tau_1 + \Delta\tau$, $r_1 = r_2 = 1.0$, $\epsilon_1 = 45$ degrees, and $\epsilon_2 = 90$ degrees. Calculations were made for $\tau_2 = 20, 18, 16, 15, 14, 13, 12,$ and 11. (b) displays the estimates $\{r, \epsilon, \tau\}$ obtained from the approximate formulas given by equations (7-A.32) and (7-A.33).

(a)

Δ_T	r_1	r_2	ϵ_1	ϵ_2	T_1	T_2
10	1.00	1.00	45	90	10	20
8	1.00	1.00	45	90	10	18
6	1.00	1.00	45	90	10	16
5	1.00	1.00	45	90	10	15
4	1.00	1.00	45	90	10	14
3	1.00	1.00	45	90	10	13
2	1.89	--	68	--	11	--
1	1.93	--	53	--	10	--

(b)

Δ_T	r_1	r_2	ϵ_1	ϵ_2	T_1	T_2
10	1.06	1.06	41	94	10	20
8	1.06	1.06	41	94	10	18
6	1.04	1.04	38	97	10	16
5	1.10	1.10	33	1.02	10	15
4	1.22	1.10	31	104	10	14
3	1.42	1.42	32	103	10	13
2	1.68	--	68	--	11	--
1	1.86	--	49	--	10	--

Thus far we have considered very simplistic noise-free examples involving only one or two reflective coefficents. More realistically we could expect a number of closely spaced reflectors and noisy obsevations. In the next example we deconvolve a inaccurate data set consisting of five phase-shifted wavelets. The results are shown in Figure 7-A.2. The wavelet and the true reflectivity and phase functions are shown in Figures 7-A.2b, 2k, and 2l, respectively. The data, with 5 percent white noise added, are shown in Figure 7-A.2a. The averages and averaging functions are shown in Figure 7-A.2c through 2h. The real averages a(t),and $\tilde{a}(t)$ (Figures 7-A.2c, 2d, and 2f) are used with equation (7-A.30) to generate a best guess $r_g(t)$ and $\epsilon_g(t)$, shown in Figures 7-A.2i and 2j. The reconstructed signal

$$x_g(t) = \mathrm{Re}[\sum_{j=1}^{M} r_j \cdot \exp[i\epsilon_j]\ \hat{w}(t - \tau j)]$$

is compared with the data x(t) in Figure 7-A.2m; their difference, displayed in Figure 7-A.2n, is a random signal with a standard deviation of approximately 5 percent.

Before leaving this example, it is of interest to carry out one more computation. Suppose it were not known that the wavelets were phase-shifted. We would proceed by deconvolving the data x(t) to recover a real reflectivity function s(t) such that x(t) = s(t)*w(t). The results of such an analysis are given in Figure 7-A.3. The averages <s(t)> in Figure 7-A.3c are easily shown to be

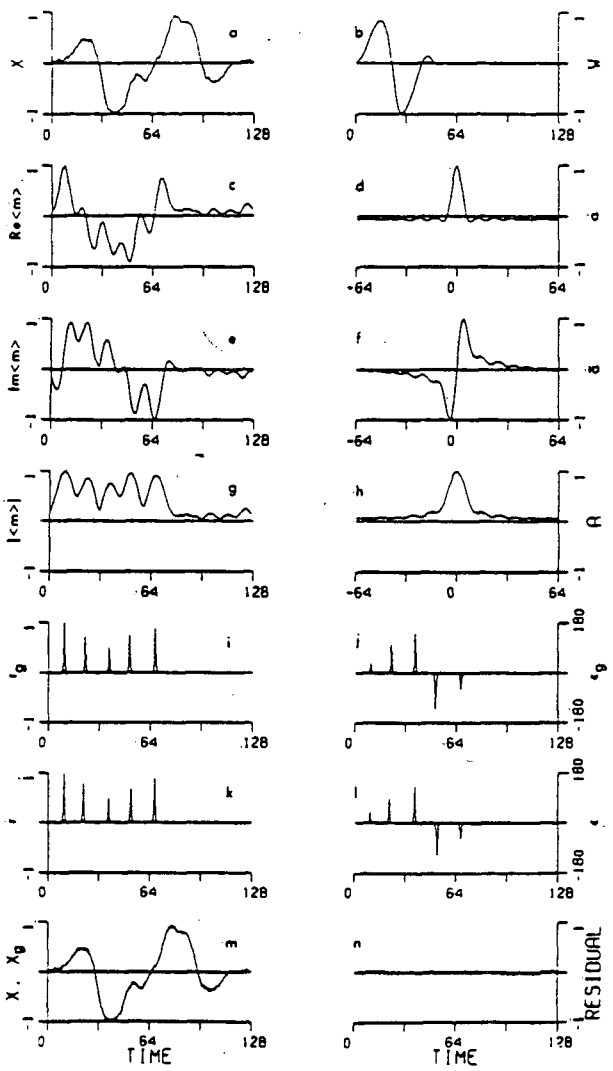

Figure 7-A.2

In successive panels are shown (a) the data; (b) the wavelet (c) the real part of the averages; (d) the averaging function a(t); (e) the imaginary averages; (f) the Hilbert transform of a(t); (g) the modulus of the averages; (h) the modulus A(t) of the averaging functions; (i) the best guess for the reflectivity function; (j) the best guess for the phase function (k) the true reflectivity function; (l) the true phase function; (m) the superposition of the data x(t) and the data reconstructed from w(t) and $r_g(t)$ and $\epsilon_g(t)$; (n) the residual between the data and the reconstructed signal.

$$\langle s(t)\rangle = \mathrm{Re}\langle m(t)\rangle$$
$$= r(t)\cos \epsilon(t) * a(t) + r(t) \sin \epsilon(t) * \tilde{a}(t), \qquad (7\text{-A.34})$$

where $r(t)$ and $\epsilon(t)$ are the true reflectivity and phase functions. Equation (7-A.34) is true in general, and consequently the neglect of phase-shifted wavelets means that only the real part of a complex function is revealed by standard deconvolution algorithms. Nevertheless, if we proceed with the deconvolution, the averages in Figure 7-A.3c show five well-resolved peaks, and a least-squares fit to find the amplitudes and positions of these spikes produces a best guess for the reflectivity sequence $s_g(t)$; that function is shown in Figure 7-A.3e. The residual

$$e(t) = x(t) - s_g(t) * w(t)$$

is shown in Figure 7-A.3f, and $x(t)$ and the reconstructed signal $s_g(t) * w(t)$ are superposed in Figure 7-A.3h. It is somewhat surprising that the residual is so small. It is also discouraging, for in practice the low-frequency deviations in the residual would likely be attributed to an imprecise knowledge of the wavelet (Oldenburg et al, 1981); thus $s_g(t)$ would be regarded as an acceptable reflectivity function. It should also be noticed that the delay times shown by $s_g(t)$ in Figure 7-A.3e are somewhat different from the true values shown in Figure 7-A.3g. This suggests that the first-order effect of neglecting true phase shifts in the wavelet

may be compensated for by altering the delay times.

As a final example, we show how the effects of phase-shifting a signal can introduce complications when attempting to correlate a particular peak (or trough) on successive traces. A wavelet taken from a marine seismic record has been phase retarded and advanced in units of 40 degrees. The phase-shifted wavelets are shown in Figure 7-A.4. The larger vertical line on the time axis denotes the position of the main positive peak, and its position is seen to change by 10 time units as the phase changes from -120 to 120 degrees; a smaller vertical reference time tick has also been plotted for each wavelet. The second and third columns of wavelets are the results after deconvolution. The Re<m(t)> is plotted in the second column; this would be the output from a standard deconvolution which neglects the possibility of phase shifts. We notice that the character of the output waveform changes markedly from record to record and that there is still a change in the time position of the positive peak on successive traces. Only in the third column, where |<m(t)>| has been plotted, does the location of the positive peak maintain a fixed time throughout all the traces.

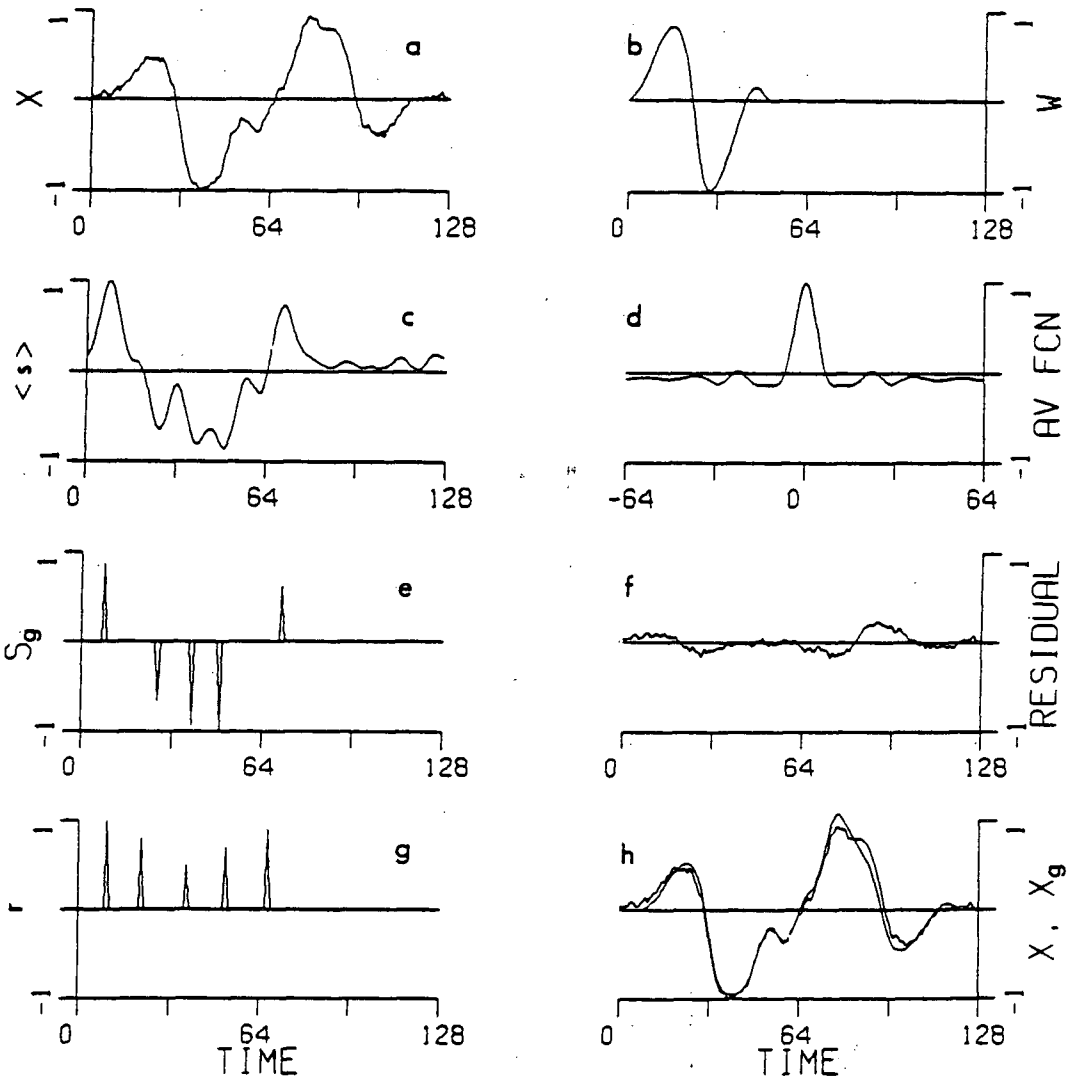

Figure 7-A.3

Shown in successive panels are (a) the data; (b) the wavelet; (c) the averages of the reflectivity function; (d) the averaging function corresponding to the averages in (c); (e) the best guess for the reflectivity function; (f) the residual between the data and s(t)*w(t); (g) the true reflectivity function; (h) the superposition of the data and the data and the reconstructed signal.

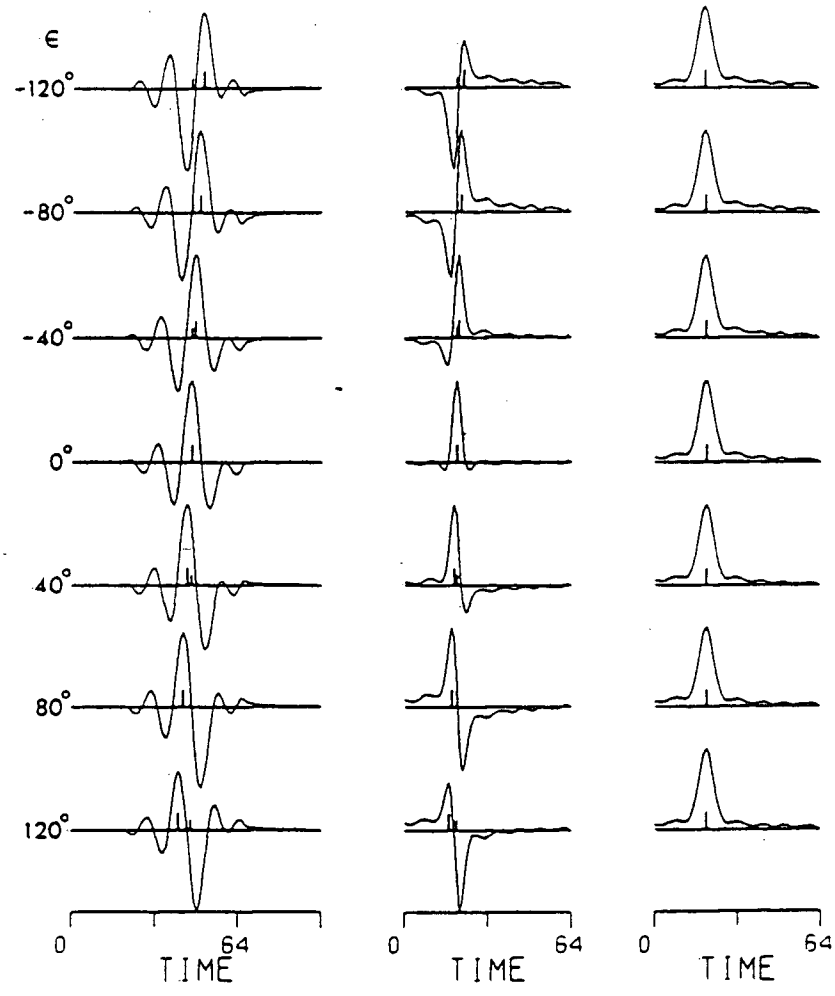

Figure 7-A.4

Wavelets, phase-shifted by amounts ϵ, are displayed in the first column. The $\mathrm{Re}\langle m(t)\rangle$ and $|\langle m(t)\rangle|$ are plotted in the second and third columns, respectively. The large vertical ticks on the time axis correspond to the central time of the main positive lobe. The smaller tick denotes a constant reference time. The small and large ticks coincide for the third column.

7-A.3 CONCLUSIONS

When a signal is composed of time-displaced, phase-shifted replications of a source wavelet, the effects of that source wavelet can be removed by deconvolution. First, the analytic signal can be written as a convolution of an analytic source wavelet and a complex model which contains the reflectivity function r(t) and the phase function $\epsilon(t)$. Linear inverse theory can then be used to recover averages of the model $\langle m(t) \rangle = \langle r(t) \exp[i\epsilon(t)] \rangle$. But these averages, because they are composed of delta-like functions a(t) and its Hilbert transform $\tilde{a}(t)$, are sometimes difficult to interpret. In seismological problems where

$$r(t) \cdot \exp[i\epsilon(t)] = \sum_{j=1}^{m} r_j \exp[i\epsilon_j] \cdot \delta(t - \tau_j),$$

the deconvolution results are more lucidly presented by displaying $|\langle m(t) \rangle|$ which is approximately equal to r(t)*A(t) (where $A(t) = [a(t)^2 + \tilde{a}(t)^2]^{1/2}$} if the distance between the successive delay times $\Delta\tau$ is greater than the width of A(t). Since A(t) will be a peaked function, the locations of maximum $|\langle m(t) \rangle|$ can be used to infer values for τj, and estimates for the amplitude coefficients rj and the phase coefficients ϵj are then easily recovered. Estimates of the variance of rj and ϵj are also available if the statistics of the observational noise are known.

An alternative method for obtaining r(t) and $\epsilon(t)$ is to recover these functions by using the averages $\langle m(t) \rangle$, and the averaging

functions a(t) and $\tilde{a}(t)$, to construct a model which fits the data. A parametric least-squares approach has been used here to find a best guess for the parameter set {rj, ϵj, τj}.

Sometimes it is not known a priori whether the wavelets making up the signal are phase-shifted. What are the consequences of deconvolving a phase-shifted signal by assuming a constant wavelet w(t)? It is shown here that only Re<m(t)> will be returned and that the averaging function will be a(t). A real reflectivity sequence s(t) can still be found such that s(t)*w(t) is an adequate representation of the original data. However, the delay times and reflectivity coefficients of s(t) may be different from those which generated the data. It seems that the first- order effect of altering the phase of the wavelet can be compensated for by altering the delay time of a fixed source wavelet. Moreover, it is speculated that the effects of inaccurate knowledge of the source wavelet might be indistinguishable from the effects of phase shifting, and so similar degradation in the deconvolved output could result either from poor knowledge of the source wavelet or from deconvolving with a fixed source wavelet when the signal is phase-shifted. All of this serves to illustrate the the nonuniqueness inherent in the deconvolution problem and stresses that some degree of caution will have to be used when applying the deconvolution to real data.

APPENDIX 7-B: APPLICATIONS OF ANALYTIC COMMON SIGNAL ANALYSIS IN EXPLORATION GEOPHYSICS

7-B.1 INTRODUCTION

The problem of extracting information from multichannels of correlated data can be approached in many ways. One very promising technique, however, is to represent the signals in terms of an orthogonal basis where the choice of basis functions is determined from the inner product matrix, that is, the covariance of the signals. The approach appears under various names in the published literature, for example: Karhunen-Loeve (KL) transformation, principal component analysis, eigenvector analysis, or Hotelling transformation. Although the mathematical foundation was originally developed by Karhunen (1947), and Loeve (1948,1955) to represent stochastic signals, the transformation has found numerous applications in areas of data compression and signal to noise enhancement (e.g. Watanabe (1965), Ready and Wintz (1973), Pelat (1974), Huang (1975)). This transformation, however, has not been widely used in seismological problems even though its potential has been exhibited by Hemon and Mace (1978). In an earlier paper (Ulrych

et al., 1984) we have reintroduced the KL transformation and showed how it could be successfully applied to problems in stacking, wavelet estimation, residual statics, and velocity analysis. The purpose of the present paper is to combine that work with the complex reflectivity convolutional model (Levy and Oldenburg, 1982). This extended mathematical framework will permit us to consider the above problems while admitting the complication of phase shifts of the wavelet. In addition to these applications, we shall show how our formalism can be applied to the problems of attenuation and dispersion, density and velocity inversion, and 'bad-trace' recognition.

Although the original work covers all the topics mentioned above, for the purpose of this thesis I will limit the discussion to the problems of dispersion and the inversion of phase-shift information associated with supercritical reflections.

7-B.2 MATHEMATICAL BACKGROUND

As pointed out in Ulrych et al. (1984), there are many ways in which the KL transformation can be derived. The work of Kramer and Mathews (1956) is, however, very straightforward and insightful. We shall first present the essence of their paper and then show its extension to complex signals.

From the point of view of data compression, we consider the problem as follows. Given a set of n real signals $g_i(t)$ ($i=1,...n$),

we define a transformed set $x_j(t)$ and a transformation (rotation) matrix A (yet to be defined) such that:

$$x_j(t) = \sum_{i=1}^{n} a_{ij}\, g_i(t) \qquad j = 1,\ldots m,\ m \le n \qquad (7\text{-B.1})$$

The signals $x_j(t)$ form an orthogonal basis, and each signal $g_i(t)$ can be expressed (approximately) as:

$$\tilde{g}_i(t) = \sum_{j=1}^{m} b_{ij}\, x_j(t) \qquad i = 1,\ldots n \qquad (7\text{-B.2})$$

where $\tilde{g}_i(t)$ is the ith reconstructed signal, B is the inverse transformation matrix, and m is the number of basis functions used in the truncated expansion.

The objective at this point is to reconstruct $\tilde{g}_i(t)$ to within a given error using the smallest possible number of basis signals. If m=n, then $\tilde{g}_i(t)=g_i(t)$, i.e., the original signal is reproduced exactly. However, this case is of no interest since it requires n basis signals in order to reconstruct the n original signals. We restrict our attention to the case where m<n, and require that the transformation matrices A and B be those that minimize the least squares error:

$$\phi(m) = \sum_{i=1}^{n} \int (\tilde{g}_i(t) - g_i(t))^2 dt, \qquad (7\text{-B.3})$$

Kramer and mathews (1956) showed that $B=A^T$, and that the rows of the transformation matrix A consist of the normalized eigenvectors of Γ, defined as:

$$\Gamma_{ij} = \int g_i(t)\, g_j(t)dt = (g_i, g_j) \qquad (7\text{-B.4})$$

Γ is symmetric and positive semidefinite and hence is decomposable. $\Gamma=R\Lambda R^T$ where $\Lambda=\mathrm{diag}(\lambda_1, \lambda_2, \ldots \lambda_n)$ with $\lambda_1 \geq \lambda_2 \geq \ldots \lambda_n$ and the columns of R contain the normalized eigenvectors $\bar{r}_i$ where $\Gamma\bar{r}_i = \lambda_i \bar{r}_i$. When $A=R^T$, the rotated signals $x_j(t)$ form an n-dimensional subspace of a Hilbert space, and with these basis elements, the truncation error in equation (7-B.3) is

$$\phi(m) = \sum_{j=m+1}^{n} \lambda_j \qquad (7\text{-B.5})$$

Since the eigenvalues are arranged in descending order it follows that the first basis function can be used to reconstruct more of the total signal energy than any other basis function. For this reason, it is called the first principal component. Similarly, the second basis function will sometimes be referred to as the second principal component, etc.

The first principal component has an important characteristic. If $g_i(t) = c_i \cdot s(t)$ where c_i are real constants, and s(t) is a given signal, then the first principal component will be

$$x_1(t) = \left(\sum_i c_i^2\right)^{1/2} \cdot s(t) \qquad (7\text{-B.6})$$

That is, the first principal component will be a scaled version of the signal s(t), and the complete set of input signals $g_i(t)$, can be reconstructed from this basis vector and an appropriate set of weights. The remaining basis vectors ($x_j(t)$, j=2,...n), will have zero eigenvalues and are not needed in the reconstruction.

The properties of the KL transformation enumerated by Kramer and Mathews(1968) for real signals carry over directly to the case when complex signals are used. For complex signals though, the inner product matrix is Hermitian and positive semi-definite and hence a unitary matrix is required for diagonalization. The eigenvalues will still be real, but the eigenvectors are complex. Nevertheless, the truncation error in equation (7-B.3) is still given by equation (7-B.5). Importantly, if we consider the case where $g_i(t) = c_i\, s(t)$ where the c_i are complex constants, then the first principal component will be

$$x_1(t) = \left(\sum_i |c_i|^2\right)^{1/2} s(t) \qquad (7\text{-B.7})$$

This latter equation shows that complex signals which differ only be a complex scale factor can be represented by a single principal component.

As an illustration, we consider the following simple example. Let $g_1(t) = s(t)$ and $g_2(t) = \exp(-i\epsilon)\, s(t)$. The energy in the signal is $||s||^2 = (s,s^*)$ and $\Gamma_{ij} = (g_i, g_j^*)$ where '*' denotes the complex conjugate. Thus

$$\Gamma = ||s||^2 \begin{bmatrix} 1 & \exp(-i\epsilon) \\ \exp(i\epsilon) & 1 \end{bmatrix}$$

The eigenvalues of Γ are $\lambda_1=2||s||^2$ and $\lambda_2=0$, while the unitary matrix is

$$U = \frac{1}{\sqrt{2}} \begin{bmatrix} 1 & \exp(-i\epsilon) \\ \exp(i\epsilon) & 1 \end{bmatrix}$$

The first basis function is $x_1(t) = U_{11}\, g_1(t) + U_{21}\, g_2(t) = \sqrt{2}\cdot s(t)$ where Ui_1 are the elements of the first column of U.

The importance of these results to recorded seismograms is apparent when phase shifts of a source signal are considered. If w(t) is the initial wavelet, then a wavelet, phase shifted by an amount ϵ, is given by

$$w(t;\epsilon) = \cos(\epsilon)\cdot w(t) + \sin(\epsilon)\ \tilde{w}(t)$$

where $\tilde{w}(t) = H[w(t)]$ is the Hilbert transform of the initial wavelet (Aki and Richards, 1980). In such cases, it is expedient to consider the analytic signal (e.g. Taner et al., 1979; Levy and Oldenburg, 1982)

$$\hat{w}(t) = w(t) - i\tilde{w}(t)$$

for the phase shifted signal can be written as

$$w(t;\epsilon) = \mathrm{Re}[\hat{w}(t)\exp(i\epsilon)]$$

Let us now consider a signal $g_1(t) = w(t)$ and another signal $g_2(t) = w(t;\epsilon)$. The corresponding analytic signals are

$$g_1(t) = \hat{w}(t)$$

$$g_2(t) = \hat{w}(t)\exp(i\epsilon)$$

Since these signals are like those considered in the numerical example, application of the Complex Karhunen-Loeve (CKL) transformation will produce a first principal component equal to w(t). Moreover, equation (7-B.8) shows that the phase rotation in the second signal is recoverable directly from the eigenvector associated with the first principal component. That is,

$$\epsilon = \tan^{-1}[\mathrm{Im}(U_{2,1})/\mathrm{Re}(U_{2,1})] \qquad (7\text{-B.8})$$

In the following sections of this paper the CKL transformation will be applied to analytic seismograms. The eigenvectors of the covariance matrix will be used as complex weights for stacking and phase estimation purposes while the corresponding eigenvalues will be used in the construction of a correlation measure. That is, the

ratio

$$\chi(m) = \sum_{i=1}^{m} \lambda_i/\phi(m) \qquad (7\text{-B.9})$$

will be used as a measure of correlation between the original set of signals. $\chi(1)>>1$ implies a good correlation, whereas $\chi(1)\simeq O(1)$ implies a poor correlation. When $\chi(1) >>1$, each of the original signals may be expressed (to within a small acceptable error) as a scaled and phase shifted verson of the first principal component. Consequently, phase-shifts in the various signals can be estimated from the eigenvector associated with λ_1, and subsequently used for physical parameters inference.

7-B.3 MODELLING DISPERSION BY A CONSTANT PHASE-SHIFT

The properties outlined above suggest that the CKL algorithm can be very useful in investigating those physical phenomena that introduce phase shifts which, to first order, can be approximated by a constant. If the applicability of this model can be established, then estimation of the phases involved can yield useful information about earth properties.

Following Robinson (1979), we shall assume a constant Q model for attenuation, and model dispersion using the Fourier scaling

theorem. Our aim is to use the CKL method to determine whether an observed dispersion effects can be approximated by a constant phase shift, viz. $g(t) = \mathrm{Re}[\hat{g}(t) \exp(i\epsilon]$, where $g(t)$ is a measured seismogram which has undergone dispersion. If applicability can be determined, the first eigenvector will be used to estimate the shift angle ϵ (Equation 7-B.8) which will rotate the dispersed trace to its undispersed form.

Given a reference wavelet, the applicability of the constant phase shift model is determined by completing the following steps: (1) select a time window which contains a dispersed pulse; (2) calculate the envelope of the analytic signal for the dispersed pulse and reference pulse (initial wavelet), aligning the peaks of the envelopes so there is no time discrepancy; (3) apply the CKL transformation; (4) evaluate $\chi(1)$. If $\chi(1)$ is large, then the dispersed signal is approximately a phase shifted verson of the original. If $\chi(1) \simeq 1$ then the constant phase shift assumption is not valid.

Figure 7-B.1(a) shows three time delayed Ricker wavelets (center frequency 25 Hz), dispersed by cumulative Q values of 1000, 60, and 30 respectively. Large Q values produce little distortion and so the event at 0.5 seconds (Q=1000) is nearly identical to the source wavelet, and is considered here as the reference signal. The events at 0.9 seconds (Q=60) and 1.5 seconds (Q=30) have considerable distortion and will be used in conjunction with the reference signal to test the validity of the constant phase shift approximation. For the event at 0.9 seconds, we find that $\chi(1)=5364$, while analysis of the deeper event yields $\chi(1)=656$. These values are

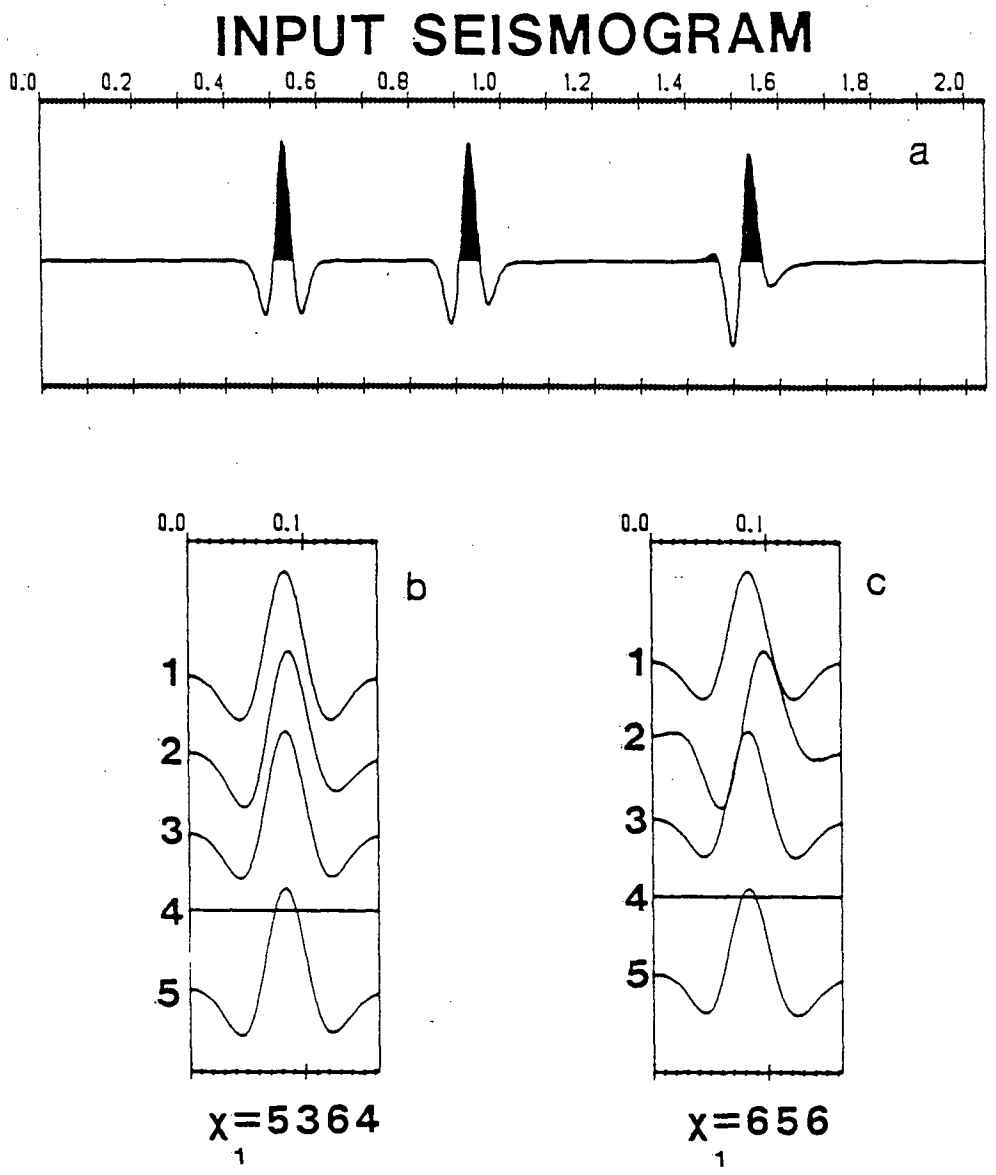

Figure 7-B.1

(a) Dispersed Ricker wavelets for cumulative Q values of 1000, 60, and 30 respectively. (b) (1) The wavelet at 0.5 secs, (2) wavelet at 0.9 secs, (3) and (4) first and second principal components of (1) and (2), and (5) a phase rotated version of (2). Here $\chi(1)=5364$. (c) Same as in (b) but for the wavelet at 1.5 seconds. Here $\chi(1)=656$.

both large and, hence, the corresponding wavelets can be properly undispersed by applying the appropriate constant phase corrections as is shown in Figures 7-B.1b and c.

A more realistic example includes the effects of dispersion and attenuation. In Figure 7-B.2a we have regenerated the synthetic of Figure 7-B.1a, and included attenuation. In this case, the reference and the distorted signals are different in both their phase and amplitude spectra. The values of $\chi(1)$ are still quite large ($\chi(1)=195$ for the event at 0.9 seconds, and $\chi(1)=91$ for that at 1.5 seconds, hence, the constant phase approximation is still acceptable. This is verified by comparing corrected signals (Fig. 7-B.2(b) and 7-B.2(c)) to the source signal (upper trace in each panel). Note that no attempt was made to remove the effects of attenuation, and hence both corrected signals are of longer time duration than the reference signal.

As expected, the constant phase shift approximation to attenuation related dispersion deteriorates with decreasing Q, and increasing travel-time. Furthermore, it will also deteriorate with increasing frequency bandwidth. However, our experiance to date, shows that over a bandwidth of about 2-2.5 octaves it seems to yield a reasonable approximation.

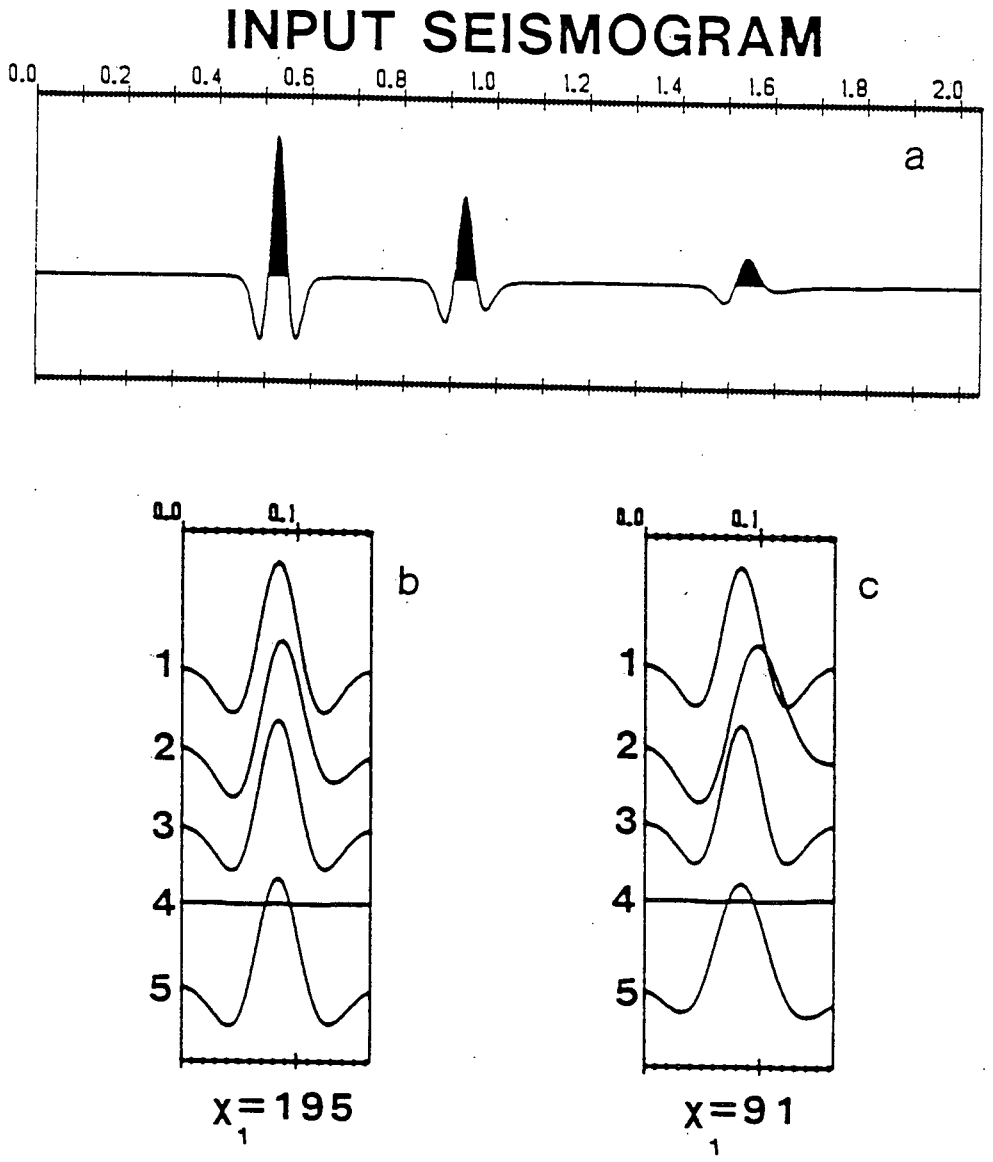

Figure 7-B.2

Same as Figure 7-B.1. Here however, we have included the effects of attenuation as well as disperson. The value of $\chi(1)$ For Fig. 7-B.2b is 195, while that for Fig. 7-B.2c is 91.

7-B.4 DENSITY AND VELOCITY ESTIMATION FROM SUPER-CRITICAL REFLECTIONS

For a plane wave travelling in a fluid layer overlaying a fluid half-space, the equation which relates phase shift $S(\theta)$ with the angle of incidence θ for a supercritical reflection (Rayleigh, 1945) is given by:

$$\tan^2\epsilon = \rho^2{}_1/\rho^2{}_2 \cdot (\tan^2\theta - v_1{}^2/v_2{}^2 \cdot (1/\cos^2\theta)) \qquad (7\text{-B.}10)$$

where $\epsilon = S(\theta)/2$. Given the velocity v_1, the density ρ_1, the angle of incidence θ, and the angular dependence of the phase shifts $S(\theta)$, for a number of observations at different offsets, we solve a set of equations (linear in $1/\rho_2{}^2$ and $1/\rho_2{}^2v_2{}^2$) in the form of equation (7-B.10) to obtain the half-space density ρ_2 and its acoustic velocity v_2. In this section, we will use the CKL algorithm to estimate the phase-shift - angle of incidence relation $S(\theta)$ for a bottom reflection in a deep water oceanic environment. The information contained in $S(\theta)$ will then be inverted to yield both density and velocity of the uppermost ocean bottom sediments layer. Velocity profiles from travel-time inversions will then be compared to the estimates obtained from the phase information in order to establish the credibility of the estimated phases.

A data set previously analysed by Chapman et al. (1984) was used for the purpose of density inversion. The data, shown in Figure 7-B.3a, are deep water reflections from Arctic Abyssal Plate

sediments. In the analysis of the data we have limited our attention to the four larger amplitude events in the second group of arrivals (the water column multiples), seen between times 1.7 sec and 2.5 sec, and offsets 25000 m and 38000 m. These arrivals were chosen because of their good signal to noise ratio. It was concluded on the basis of a previous analysis, and on the times and polarities of these events, that they corresponded to reflections from a single interface in the sediments, but with different path combinations (see Figure 7-B.3b).

The phase shift's angular dependence $S(\theta)$ was estimated from this reflection data: this analysis began by finding a suitable 'reference', i.e. a far-field signature of a pre-critical (un-phase shifted) signal, in this case the first bottom bounce on the nearest offset trace. The phase differential between the reference and each of the post-critical signals was then determined using equation (7-B.8). These differential phases (summarized in Table 7-B.1) constitute components of the angular dependence function $S(\theta)$ required in the solution of equation (7-B.10).

An example of phase estimation for the first of the reflection events is shown in Figure 7-B.3c, where the data shown are taken from a 100 msec window enclosing the event of interest for the different offset traces. Shown are: the reference signal, 6 post-critical reflections (from offsets 25000m - 38000m), the envelopes of the analytic signals of the 7 waveforms, and finally, the reference and the 6 post-critical wavelets after phase rotation to the reference.

Using straight ray travel paths through the water column we

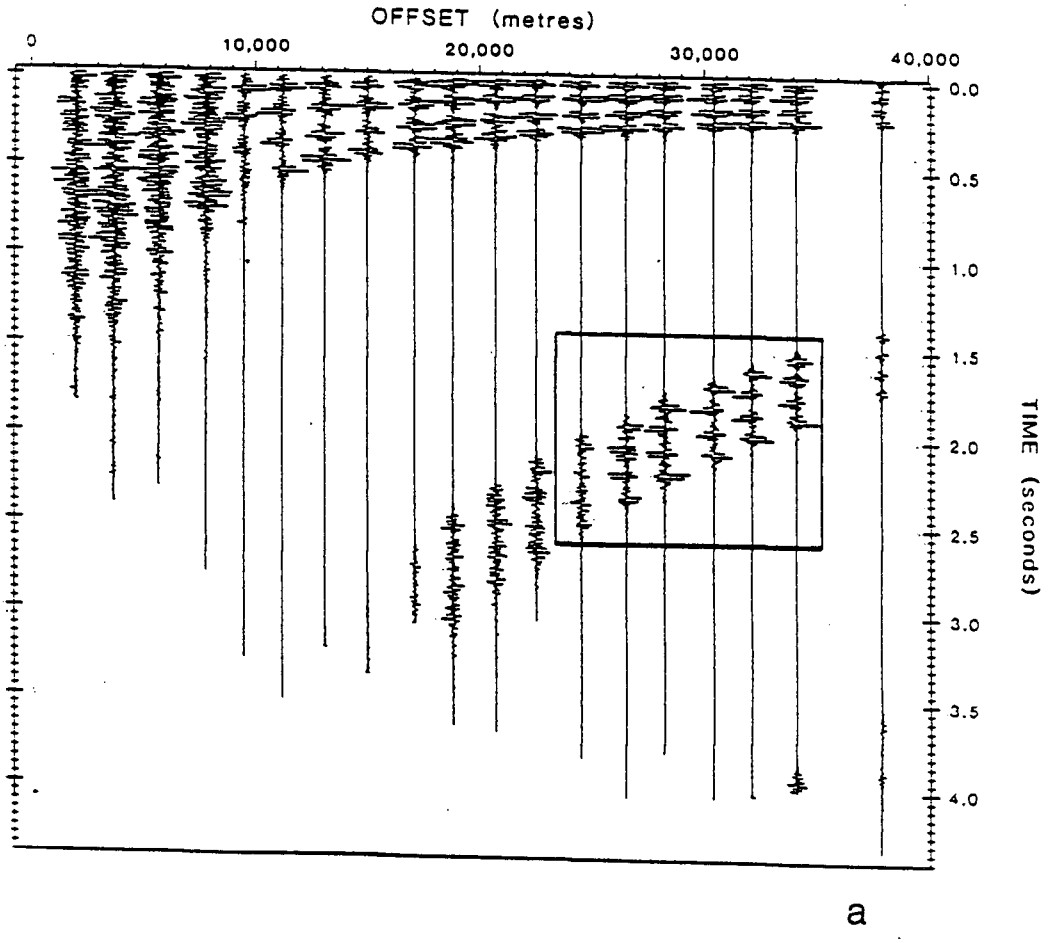

Figure 7-B.3

(a) Reduced time plot of the data aligned on the water bottom reflection. In the inset box are the super-critically reflected data to be analysed. The first event on the first trace of the figure (outside the box) is taken as the pre-critical reference trace.

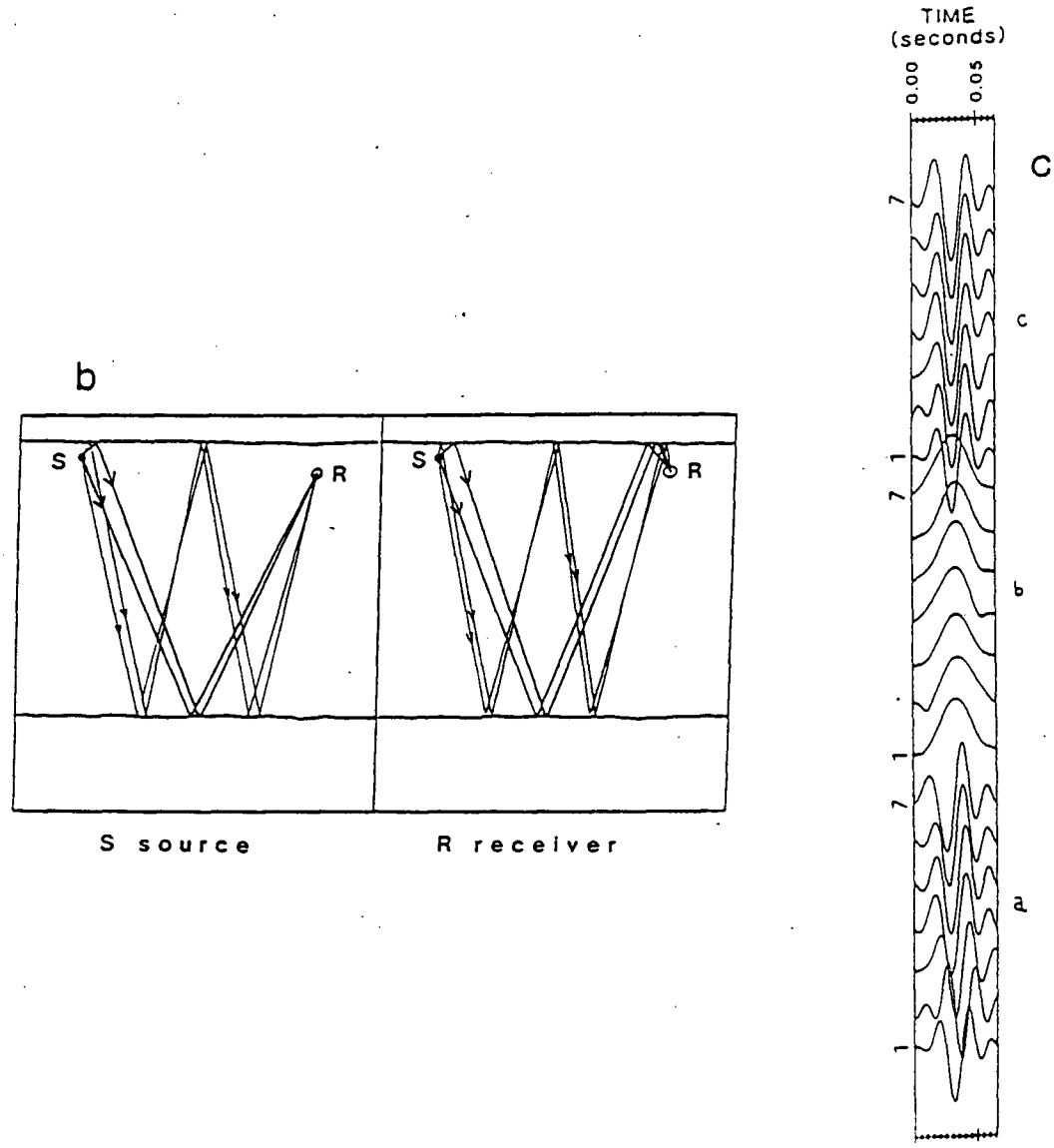

Figure 7-B.3

(b) Travel path for the analysed water bottom reflection event. (c) A sample window of data used for phase estimation (see text). Shown are the pre-critical reference and 6 post-critical reflections, the envelopes of these 7 wavelets, and finally the 7 wavelets after phase rotation to the reference.

FIRST MULTIPLES					
		HORIZON #			
x (km)	θ RADIANS	1 Phase	2 Phase	3 Phase	4 Phase
28.20	1.088	0.699	0.431	0.422	0.353
30.40	1.118	1.109	0.902	1.000	1.130
32.10	1.139	1.136	0.989	1.298	1.330
34.10	1.161	1.373	1.316	1.490	1.466
37.80	1.198	1.483	1.390	1.566	1.503

TABLE 7-B.1

Offset, angle of incidence θ, and phase angle (in radians) for the four reflections associated with the first multiple (see Figure 7-B.1). All phases are relative to a precritical arrival. The phases have been halved because the multiple path has two reflections from the water bottom.

have estimated the angles of incidence for each of the offsets present in the analysed data sets (see Table 7-B.1). We then solve the set of equations minimizing the square of the errors $\sum_{i} (\epsilon_i^c - \epsilon_i^o)^2$ where the superscripts c and o stand for 'calculated' and 'observed' phases respectively. The estimated velocity and density ratios for the water bottom sediments obtained from each of the analysed data sets are as given in Table 7-B.2.

These latter results are consistent with velocity profiles obtained from travel-time inversions (p-τ inversion Garmany (1979), and Dix like inversion Oldenburg et al. (1984)) which gave an average sediments sound speed of about 1700m/sec. Consequently, the above example adds credibility to both the CKL phase estimation and the inversion procedures.

7-B.5: CONCLUSIONS

In this appendix we have introduced the complex Karhunen-Loeve transformation and briefly reviewed some of its applications.

The ability of the method to deal with phase shifts and to extract phase information from groups of wavelets has proven most instructive in the description and analysis of phenomena involving phase changes, such as dispersion and super-critical reflection.

Small time shifts are transparant to the method, as it can approximate them as a small phase shift and hence avoid the problems which would beset conventional methods.

The scaling properties of the attendant eigenvectors proved

TABLE IV

FIRST MULTIPLES				
	HORIZON #			
	1	2	3	4
density ratio	1.23	1.17	1.00	1.12
sound speed ratio	1.17	1.14	1.15	1.16
sound speed (km/s)	1.81	1.77	1.78	1.80

TABLE 7-B.2

Density and sound speed ratios (ρ_2/ρ_1, and v_2/v_1) for the 'second layer' (see text) determined from inversion of the phases shown in Table 7-B.1. Using the estimated sound speed ratios and a sound speed for the 'first layer' of 1.55 km/s, the sound speeds for the 'second layer' were also estimated.

useful as a discriminator against uncorrelated seismic traces. This enables us to isolate such bad traces and omit them from further processing procedures, thus avoiding unnecessary signal degration.

A useful measure of similarity was obtained from the eigenvalues ratio $\chi(m)$. This enabled us to perform a CKL velocity analysis which seems to yield better results under conditions of static scatter than did a corresponding semblance velocity anaysis.

Given the ability of the CKL method to overcome the problems of small time shifts, we noted how a useful stacking tool could be developed. We applied the CKL stacking algorithm to several synthetic CDP gathers, and the result compared favourably with the section obtained by the application of the mean stack routine. We feel that this comparison justify further research of the stacking properties of the CKL algorithm.

As a corollary to the above points, the estimation of the seismic wavelet is a natural follow-up. The CKL estimate of the wavelet provided a sharper and more accurate representation of the input pulse than did the conventional estimate.

In conclusion, we note that the complex Karhunen-Loeve transformation, an extension of the long known Karhunen-Loeve transformation, has many and diverse applications in the field of exploration seismology. Further aplications and extensions of the work discussed here are presently under investigation.

Publications and Reports

Levy, S. and Clowes, R.M., 1980, Debubbling: A Generalized Linear Inverse Approach, Geophysical Prospecting 28, 840-858.

Oldenburg, D.W., Levy, S., and Whittall, K.P., 1981, Wavelet Estimation and Deconvolution, Geophysics, Vol. 46, No. 11, pp. 1528-1542.

Levy, S. and Fullagar, P.K., 1981, Reconstruction of a Sparse Spike Train from a portion of its Spectrum, and Application to High-Resolution Deconvolution, Geophysics, Vol. 46, pp. 1235-1243.

Levy, S. and Oldenburg, D.W., 1982, The Deconvolution of Phase-Shifted Wavelets, Geophysics, Vol. 47 pp 1285-1294.

Levy, S., Walker, C., Ulrych, T.J., and Fullagar, P.K., 1982, A Linear Programming Approach to the Estimation of the Power Spectra of Harmonic Processes, I.E.E.E. Transactions on Acoustic, Speech, and Signal Processing, Vol. ASSP-30, No. 4, August 1982.

Oldenburg, D.W., Scheuer, T., and Levy, S., 1983, Recovery of the Acoustic Impedance from Reflection Seismograms, Geophysics, Vol. 48, No. 10, pp. 1318-1337.

Oldenburg, D.W., Levy, S., and Stinson, K., 1984, RMS Velocities and Recovery of the Acoustic Impedance from Reflection Seismograms, Geophysics, Vol. 43, No. 10, pp. 1653-1663.

Cabrera, J.J. and Levy, S., 1984, Stable Plane-Wave Decomposition and Spherical Wave Reconstruction: Applications to Converted S-Mode Separation and Trace Interpolation, Geophysics, Vol. 49, No. 11, pp. 1915-1932.

Levy, S., Ulrych, T.J., Jones, I.F. and Oldenburg, D.W., 1983, Applications of Complex Common Signal Analysis in Exploration Seismology (presented in the 53rd SEG meeting in Las Vegas). To be submitted to Geophysics.

Levy, S. and Oldenburg, D.W., 1985, Automatic Phase Correction of CMP Stacked Data. Submitted to Geophysics.

Stinson, K. and Levy, S., 1984, Multi-Trace Simplex Algorithm in Seismic Data Analysis (presented in the 54th SEG Meeting in Atlanta). To be submitted to Geophysics.

Chapman, R., Levy, S., Stinson, K., Jones, I.F., Prager, B.P. and Oldenburg, D.W., Analysis of Deep Ocean Marine Seismograms by Inversion Techniques (submitted to the Journal of the Acoustical Society of America).

Levy, S., Oldenburg, D.W. and Wang, Jiaying, 1985, Subsurface Imaging Using M.T. Data (to be submitted to Geophysics 1985).

Oldenburg, D.W., Levy, S.W., Stinson, K., 1985, Inversion of Band-Limited Reflection Seismograms: Theory and Practice, Submitted to IEEE.